UNIVERSITY OF TRENTO
DEPARTMENT OF INDUSTRIAL ENGINEERING
DOCTORAL PROGRAMME IN MATERIAL, MECHATRONICS AND SYSTEMS ENGINEERING

APPLICATION OF AVALANCHE DETECTORS IN SCIENTIFIC AND INDUSTRIAL MEASUREMENT SYSTEMS

Doctoral Dissertation of:
Andrea Ficorella

Advisor:
Prof. Lucio Pancheri

Co-Advisor
Prof. Gian-Franco Dalla Betta

2019 XXXI Cycle

List of journal publications

[1] Pancheri, L., Brogi, P., Collazuol, G., Dalla Betta, G. F., Ficorella, A., Marrocchesi, P. S., Morsani, F., Ratti, L., Savoy-Navarro, A. "First prototypes of two-tier avalanche pixel sensors for particle detection", Nuclear Instruments and Methods in Physics Research Section A: Accelerators, Spectrometers, Detectors and Associated Equipment (2016).

[2] Pancheri, L., Ficorella, A., Brogi, P., Collazuol, G., Dalla Betta, G.-F., Marrocchesi, P. S., Morsani, F., Ratti, L., Savoy-Navarro, A., Sulaj, A. "First demonstration of a two-tier pixelated avalanche sensor for charged particle detection", IEEE Journal of the Electron Devices Society (2017).

[3] Ficorella, A., Pancheri, L., Brogi, P., Collazuol, G., Dalla Betta, G.-F., Marrocchesi, P. S., Morsani, F., Ratti, L., Savoy-Navarro, A. "Crosstalk Characterization of a Two-tier Pixelated Avalanche Sensor for Charged Particle Detection", IEEE Journal of Selected Topics in Quantum Electronics (2017).

[4] Zanazzi, E., Favaro, M., Ficorella, A., Pancheri, L., Dalla Betta, G.-F., Quaranta, A. "Proton Irradiation Effects on Colloidal InGaP/ZnS Core-Shell Quantum Dots Embedded in Polydimethylsiloxane: Discriminating Core from Shell Radiation-Induced Defects Through Time-Resolved Photoluminescence Analysis", Journal of Physical Chemistry Part C (2018).

[5] Englbrecht, F.S., Wurl, M., Olivari, F., Ficorella, A., Kreuzer, C., Lindner, F.H., Dalla Palma, M., Pancheri, L., Dalla Betta, G.-F., Schreiber, J., Quaranta, A., Parodi, K. "An Online Radiation Hard Proton Energy-resolving Scintillator Stack For Laser-driven Proton Bunches", Radiation protection dosimetry (2018).

[6] Zanazzi, E., Favaro, M., Ficorella, A., Pancheri, L., Dalla Betta, G. F., Quaranta, A. "Radiation-induced optical change of ion-irradiated CdSeS/ZnS core-shell quantum dots embedded in polyvinyl alcohol." Nuclear Instruments and Methods in Physics Research Section B: Beam Interactions with Materials and Atoms (2018).

[7] Musacci, M., Bigongiari, G., Brogi, P., Checchia, C., Collazuol, G.,Dalla Betta, G.-F., Ficorella, A., Marrocchesi, P.S., Mattiazzo, S., Morsani, F., Noli, S., Pancheri, L., Ratti, L., Savoy Navarro, A., Silvestrin, L., Stolzi, F., Suh, J., Sulaj, A., Vacchi, C. "Radiation tolerance characterization of Geiger-mode CMOS avalanche diodes for a dual-layer particle detector." Nuclear Instruments and Methods in Physics Research Section A: Accelerators, Spectrometers, Detectors and Associated Equipment (2018).

[8] Ratti, L., Brogi, P., Collazuol, G., Dalla Betta, G. F., Ficorella, A., Lodola, L., Marrocchesi, P.S., Mattiazzo, S., Morsani, F., Musacci, M., Pancheri, L., Vacchi, C. "Dark Count Rate Degradation in CMOS SPADs Exposed to X-Rays and Neutrons". IEEE Transactions on Nuclear Science (2019).

[9] Zanazzi, E., Favaro, M., Ficorella, A., Pancheri, L., Dalla Betta, G. F., Quaranta, A. "Photoluminescence enhancement of colloidal CdSe/ZnS quantum dots embedded in polyvinyl alcohol after 2 MeV proton irradiation: crucial role of the embedding medium". Optical Materials (2019).

List of conference proceedings

[1] Ficorella, A., Pancheri, L., Dalla Betta, G. F., Brogi, P., Collazuol, G., Marrocchesi, P. S., Morsani, F., Ratti, L., Savoy-Navarro, A. "Crosstalk mapping in CMOS SPAD arrays", Solid-State Device Research Conference (ESSDERC) IEEE (2016).

[2] Musacci, M., Brogi, P., Collazuol, G., Dalla Betta, G.F., Ficorella, A., Lodola, L., Marrocchesi, P.S., Morsani, F., Pancheri, L., Ratti, L., Savoy-Navarro, A., Vacchi, C. "Geiger-mode avalanche pixels in 180 nm HV CMOS process for a dual-layer particle detector", Conference Record of the IEEE Nuclear Science Symposium (2016).

[3] Marrocchesi, P. S., Brogi, P., Bigongiari, G., Checchia, C., Collazuol, G., Dalla Betta, G. F., Ficorella, A., Lodola, L., Morsani, F., Musacci, M., Noli, S., Pancheri, L., Savoy-Navarro, A., Silvestrin, L., Stolzi, F., Sulaj, A., Suh, J.E., Ratti, L., Vachi, C., Zanoli, M. Zarghami, M. "APiX: a Geiger-mode Avalanche Digital Sensor for Particle Detection", IEEE Nuclear Science Symposium and Medical Imaging Conference (NSS/MIC) (2017).

[4] Ficorella, A., Pancheri, L., Acerbi, F., Piemonte, C. "Effect of cell size on ambient light rejection in SiPM-based Time-of-Flight range sensors", Proceedings of IEEE Sensors (2017).

Abstract

Geiger-Mode avalanche photodiodes (GM-APDs) are diodes designed to operate at a reverse voltage that exceeds the breakdown voltage (V_{BD}). Their ability to detect single photons combined with their excellent timing resolution make them ideal for applications in which low amplitude signals need to be detected with sub-ns timing resolution. In the research activity reported in this dissertation two different applications of Geiger-Mode Avalanche Photo Diode arrays have been analysed: a two-tier GM-APD array with in-pixel coincidence for particle tracking and a direct Time-of-Flight range meter with a SiPM-based receiver.

The increasing complexity of particle tracking systems at collider experiments demands for high performance detectors with high granularity and position accuracy, low material budget and power consumption [1]. Both Hybrid and monolithic detectors have been proposed as particle trackers. Hybrid detectors have the advantage of allowing an independent customization of sensors and readout electronics, but they exhibit a higher input capacitance that increases readout noise, thus limiting their minimum thickness ($100\,\mu\mathrm{m}$) [2, 3]. Monolithic detectors have lower input capacitance, thus a better minimum detectable charge,

with a charge time collection of few tens of ns[4]. Thanks to their high gain, particle detectors based on GM-APDs have the potential for combining low material budget, low power consumption and an excellent timing resolution in the range of $100\,\mathrm{ps}$. However, their use as particle tracking detectors has been prevented by their Dark Count Rate, since it is not possible to discriminate a particle-generated event from a dark event. To overcome this issue, the use of GM-APDs in coincidence has been proposed.

The activity reported in this dissertation has been conducted in the framework of ApiX2 and ASAP projects funded by Istituto Nazionale di Fisica Nucleare (INFN). A two-tier sensor based on avalanche detectors in coincidence has been designed and fabricated in standard $150\,\mathrm{nm}$ CMOS technology. A charged particle crossing both GM-APDs integrated in a pixel triggers an avalanche in both devices. The output signal from each detector reaches the coincidence electronics, that allows the device to discriminate the particle detection from dark events. The performance of the proposed detector has been evaluated in a complete electrical and functional characterization campaign. The feasibility to reduce the substrate thickness has been studied in some devices thinned down to $50\,\mu\mathrm{m}$ and $25\,\mu\mathrm{m}$. The electronics for coincidence detection was also used to directly measure optical crosstalk, a phenomenon that is getting greater importance as stacked optical and image sensors are becoming common. The functional characterization of the APiX prototype was performed with a β-source and an evaluation of the radiation hardness of the devices was carried out in an irradiation campaign with neutrons at the INFN Laboratori Nazionali di Legnaro (LNL).

SiPMs take advantage of the characteristics of GM-APDs such as high sensitivity, high efficiency and very low time jitter, and overcome the problem related to the dead time connecting several sensitive elements in parallel, making them suitable for the simultaneous detection of more than one photon [5].

The evaluation of a SiPM-based direct Time-of-Flight range meter has been performed at two different wavelengths: $405\,\mathrm{nm}$ and $810\,\mathrm{nm}$. The set of measurement at $405\,\mathrm{nm}$ has been performed using a TCSPC module as acquisition system, while in the $810\,\mathrm{nm}$ measurements

a low-cost FPGA-based TDC was used. The replacement of the TCSPC module with an FPGA-based TDC represents an important step towards the integration of a low-cost prototype thanks also to the low power consumption of the device. In order to evaluate the feasibility of a SiPM-based range meter in the NIR region, a collaboration with the Circuits and Systems Research Unit of the ITEE Faculty of the University of Oulu was established to set up a system with a GaAs/AlGaAs multiple quantum well laser diode with a spectral emission of $\sim 0.808\,\mu\mathrm{m}$ [6] as transmitter and a NIR-HD SiPM with an enhanced efficiency for NIR photons recently developed at FBK [7] as receiver. The evaluation was performed at high repetition rate (MHz range), for the perspective purpose to upgrade the system including a 2-axis scanning mirror to perform real-time 3D imaging [8].

Contents

1 Geiger-Mode Avalanche PhotoDiodes **1**
1.1 Theory 1
1.2 GM-APD arrays 5
1.2.1 CMOS SPAD Arrays 5
1.2.2 Silicon PhotoMultipliers 7
1.3 Characteristics of GM-APDs 9
1.3.1 Dark Counts 9
1.3.2 Optical Crosstalk 12
1.3.3 Afterpulsing 14
1.3.4 Photon Detection Efficiency 15
1.3.5 Dynamic range 17
1.3.6 Single Photon Time Resolution 17
1.4 Single Photon detection 19
1.5 Applications 21

2 Particle Detectors **31**
2.1 Radiation Interaction with Silicon 32
2.1.1 Charged Particles 32
2.1.2 Electromagnetic Radiation 33
2.1.3 Neutrons 33

2.1.4 Radiation induced effects 34
2.2 Silicon Particle Detectors 37
2.3 Geiger-Mode APD Particle Detectors 39
2.4 APiX Projects 40
2.5 Single Layer Chip Architecture 41
2.5.1 Detector Cross-section 42
2.5.2 Array Architecture 43
2.5.3 In-pixel Electronics 44
2.6 Vertically-integrated Chip Architecture 47

3 Device Characterization **49**
3.1 Setup 50
3.1.1 Interface Board 51
3.1.2 Microcontroller 52
3.2 Breakdown Voltage 56
3.2.1 Extraction of the Breakdown Voltage 57
3.2.2 Breakdown Voltage Uniformity 58
3.3 Dark Count Rate 58
3.3.1 DCR Uniformity 60
3.3.2 Temperature Dependence 61
3.4 Optical Crosstalk 62
3.4.1 Crosstalk dependence on excess voltage 64
3.4.2 Dependence on substrate thickness 65
3.4.3 Detectors Comparison 69
3.4.4 Overall effect of Crosstalk 70
3.4.5 Inter-Layer crosstalk 73

4 Characterization with radiation sources **77**
4.1 Experimetal characterization with a β source 78
4.1.1 Preliminary Evaluation 78
4.1.2 Particle Detection Rate Simulation 79
4.1.3 Experimental characterization 82
4.2 Neutron irradiation 86
4.2.1 Description of the irradiation campaign 86
4.2.2 Results of the irradiation campaign 88
4.2.3 Dependence of the dark counts on neutron fluence 92

4.3 Proton irradiation 92
4.3.1 Experimental setup 93
4.3.2 Preliminary setup configuration 94
4.3.3 On-line proton measurement 96
4.4 Conclusions 98

5 SiPM based Time-of-Flight range meter 99
5.1 Direct Time-of-Flight(ToF) range meter working principle 100
5.2 Experimental Setup 102
5.2.1 Receiver 102
5.2.2 Optics 104
5.2.3 Transmitter 105
5.2.4 Acquisition system 105
5.3 Preliminary measurements 106
5.3.1 Threshold voltage selection 106
5.3.2 Effect of ambient light on a fixed target 107
5.3.3 Distance Measurements 108
5.3.4 Ambient light filtering 113
5.4 Portable ToF range meter with high-energy short-pulse laser diode 116
5.4.1 Experimental setup 117
5.4.2 Preliminary measurement 122
5.4.3 Target reflectivity 123
5.4.4 SiPM comparison 124
5.5 Conclusions 126

6 Conclusions and Future Perspectives 129

Bibliography 143

CHAPTER 1

Geiger-Mode Avalanche PhotoDiodes

Geiger-Mode avalanche photodiodes (GM-APDs) are diodes designed to operate at a reverse voltage that exceeds the breakdown voltage (V_{BD}) (i.e. the voltage at which a self-sustaining avalanche occurs). This extra voltage is commonly referred as excess voltage (V_{EX}) or overvoltage (V_{OV}). Single Photon Avalanche Diodes (SPADs) is an alternative name for GM-APDs that explicit the theoretical detection potential of these diodes to reveal single photons.

1.1 Theory

The small energy of a single photon that is absorbed in a diode may provoke the transition of a valence electron to the conduction band leaving an hole in the valence band. Normally, a single incoming photon cannot be detected through the collection of this infinitesimal charge, that will

be hidden by electronic noise.

In a photodiode biased at low reverse voltage, however, a high flux of photons can be directly detected measuring the output current since it generates a large number of e-h pairs, overcoming the electronic noise of the readout circuitry.

In an Avalanche Photodiode (APD) biased at an high reverse voltage, but still above the breakdown voltage, the high-field promotes the so called multiplication process that, starting from the initial e-h pair, increases the number of charge carriers, making a detectable current flow.

This multiplication process is due to the generation of e-h pairs by impact ionization, promoted by the high-field and resulting in a signal enhancement. Notwithstanding the high gain, that can be in in the order of few hundreds, a single photon cannot generate an adequate current to be detectable. The higher electric field, obtained biasing the GM-APD beyond the breakdown voltage, induces the multiplication process to be self-sustained, making them able to detect signal levels as low as a single photon.

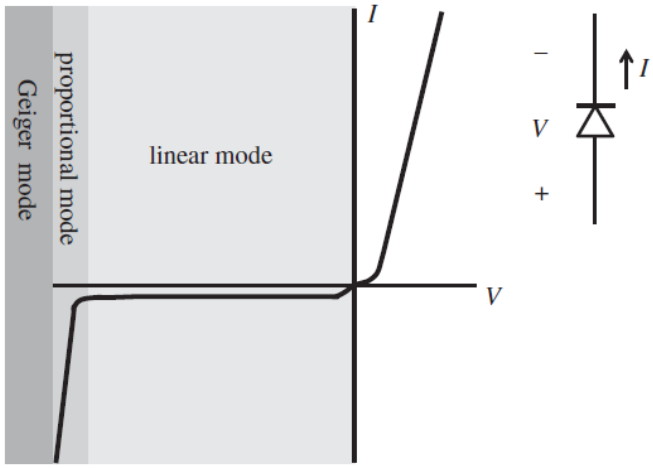

Figure 1.1: *IV curve of a diode. Linear mode is the operative range of conventional photodiodes, proportional mode is the operation range of APDs, while exceeding the breakdown voltage the GM-APDs operation range is reached [9].*

The avalanche process features five different phases happening in sequence:

- Seeding
- Build-up
- Spreading
- Quenching
- Recharging

The seeding is the generation of the electron-hole pair after the absorption of an incoming photon. At this point the high electric field at the junction increases the ionization rate and therefore causes a non-negligible avalanche trigger probability if the detector is biased in the Geiger-mode above the breakdown voltage [9]. It is worth mentioning that in silicon electrons and holes have different ionization rates according to their different mobility, giving rise to different mean free-paths [10]. When an avalanche it's triggered, the build-up phase takes place with an increase of the current density that is still confined in the pn junction. In this phase no output signal can be externally detected until the multiplication-assisted diffusion process that spreads the avalanche towards the whole diode occurs (spreading phase). At this point the current flow reduces the voltage across the junction leading to the quenching of the avalanche. This phase is important to prevent the destruction of the device by overheating and its duration combined to the recharge time is responsible for the dead time of the device. In addition to this, a fast quenching avoids an excessively large amount of carriers flowing during the avalanche, thus reducing the correlated noise [9].

A quenching circuit lowers the bias voltage reducing the strength of the electric fields. During the quenching phase, none of the carriers crossing the high field region get enough energy to promote the impact ionization, so the current is no more self sustaining and the avalanche is quenched. The last phase is the recharge phase in which the bias voltage

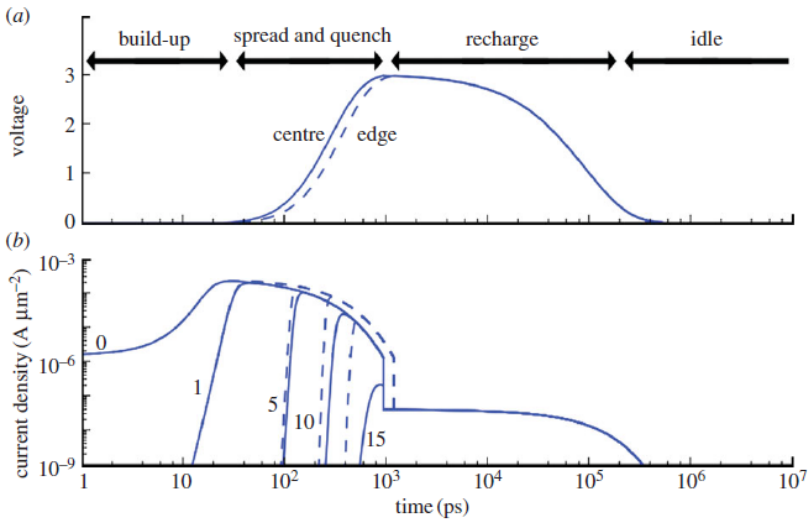

Figure 1.2: *Representation of the five constitutive phases of the avalanche process. (a) pn junction voltage at the anode; (b) Current density as a function of the distance from the junction in* μm *[11].*

across the junction is restored to the geiger-mode regime making the detector to be able to detect another event (idle state).

Quenching and recharging can be performed with different configurations with passive and active mechanisms. The simplest configuration is the passive scheme, obtained by placing in series to the diode a quenching resistor properly tuned to reduce the voltage across the junction under the breakdown voltage when the avalanche current flows trough it. GM-operative voltage is then restored to the idle state when the current stops flowing and the voltage drop across the resistor is no more present. Metal Oxide Semiconductor (MOS) transistors can be used both in passive and active circuits to define the dead time of the detector [12].

A simplified schematic SPAD model is shown in Fig. 1.3 with the avalanche current modeled by the current generator I_a with the series of the space-charge resistance R_{sc} and the quenching resistance R_q. The parasitic capacitance of the depletion region is modeled by C_d while C_p

is the parasitic capacitance of the quenching resistance [9].

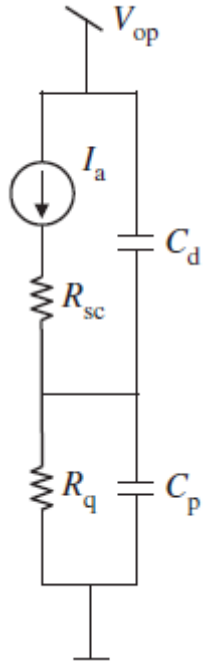

Figure 1.3: *Semplified model of the SPAD. Figure adapted from [9].*

1.2 GM-APD arrays

In this section, a brief description of the development of GM-APD arrays is reported focusing on the possibility of integrating Complementary Metal Oxide Semiconductor (CMOS) electronics in GM-APD arrays to perform high level data processing at the chip level.

1.2.1 CMOS SPAD Arrays

Early GM-APDs exhibited excellent performances in terms of noise, time-jitter and detection efficiency since they were produced in dedicated fabrication processes [13]. Despite these excellent achievements,

dedicated fabrication processes prevented a low-cost large-scale production.

The integration of GM-APDs in standard CMOS technologies was initially limited by special doping constraints to be observed in order to suppress the Periphery Edge Breakdown (PEB) and to limit the field-enhanced dark counts. A uniform breakdown voltage over the entire active area and a moderate dark count rate are the two fundamental requirements to be fulfilled for an avalanche photodiode to act as single photon counter [14].

Starting from 2002, when Rochas et al. [13] proposed a simple design technique that allowed the fabrication of avalanche photodiodes in conventional CMOS process, several different structures have been proposed for the realization of CMOS GM-APDs [15, 16, 17, 18, 19, 20, 21].

Although the CMOS fabrication features several advantages in terms of reproducibility of dark current and gain at a low cost of fabrication, the major benefit is the possibility to integrate the avalanche photodiode with front-end and readout electronics [9].

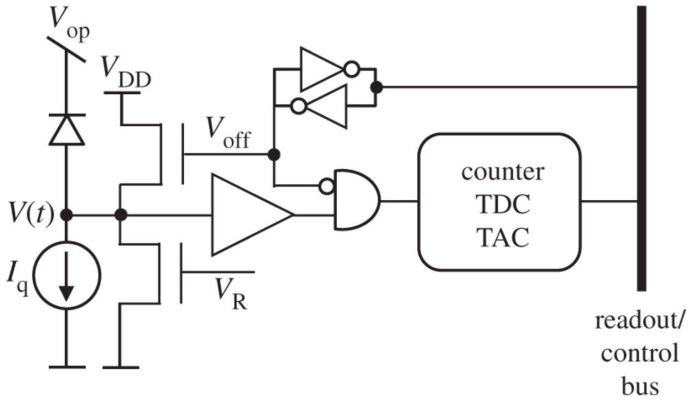

Figure 1.4: *GM-APD pixel with generic CMOS front-end electronic [9].*

In Fig.1.4, a simplified schematic of a pixel of a GM-APD array is reported with an example of front-end electronics that can be potentially CMOS integrated at pixel level to perform high-level functions.

In section1.3.1 a detailed description of Dark Count Rate (DCR) in

GM-APDs will be reported. However, in order to fully understand the importance of CMOS in-pixel electronics in SPAD arrays, it is worth anticipating here that some pixels within a SPAD array suffer of extremely high DCR compared to the rest of the array. These high DCR pixels can degrades the performance of the whole array. An in-pixel memory driven by a readout/control bus can be used to selectively disable the defective pixels ensuring better array performance.

Other examples of in-pixel electronic functionalities are uncorrelated photon counting, performed with integrated analog or digital counters, and correlated photon counting to be performed with integrated Time to Digital Converters (TDCs) or Time to Amplitude Converters (TACs).

These functionalities can be achieved by implementing different architectures with respect to the array design referred as in-pixel, in-column and on-chip electronics. In-pixel electronics benefit of detector proximity to perform their functionalities at the expenses of a Fill Factor (FF) reduction. In-column electronics imply a lower loss of sensitive area since the circuitry is located at the side of the array, while on-chip electronics are usually dedicated to data readout [9].

1.2.2 Silicon PhotoMultipliers

Silicon Photo-Multipliers (SiPMs) are the silicon solid-state alternative of standard Photo-Multiplier Tubes (PMT) from a functional point of view since both types of detectors feature an internal gain, providing an amplified current pulse when detecting a photon[22]. The basic structure of a SiPM is a cell composed of a GM-APD detector with its integrated passive-quenching resistor. A SiPM features a peculiar SPAD array in which the combination of several cells arranged in a matrix are connected in parallel forming a common anode and cathode [23, 24].

In Fig.1.5 the cross-sections of two SiPM cells fabricated with two different processes are reported. The two structures differ for a complementary alternation of the doping profiles in order to achieve a higher Photo Detection Efficiency (PDE) in a different spectral range [25].

Being made of several SPADs connected in parallel, the output of a SiPM is the combination of the output of each cell triggered by an

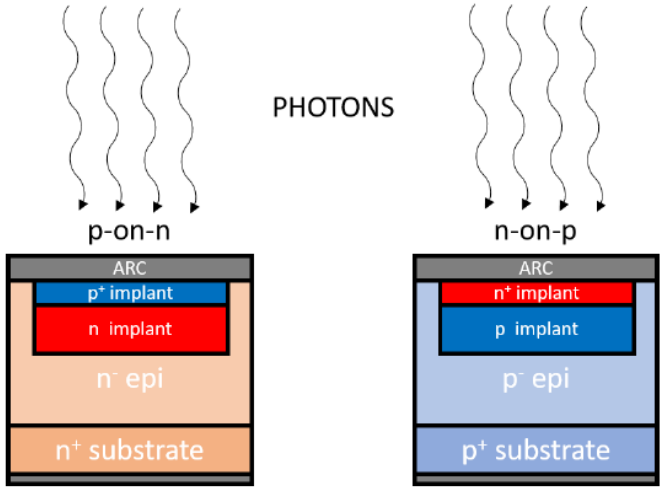

Figure 1.5: *Cross-sections of a cell of a p-on-n SiPM (left) and a cell of a n-on-p SiPM (right) [25].*

impinging photon. Thus, the output of a SiPM is proportional to the number of triggered cells. The output signals with a different number of cells firing, acquired with an oscilloscope in persistence mode, are shown in Fig. 1.6 [26].

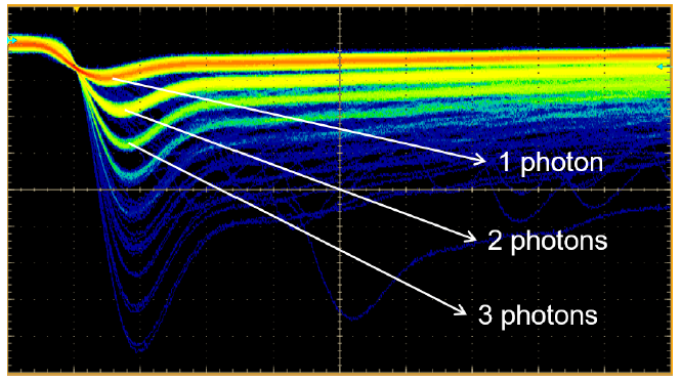

Figure 1.6: *SiPM output acquired with an oscilloscope in persistance mode [26].*

1.3 Characteristics of GM-APDs

In the first part of this section the characteristics of GM-APD detectors in terms of noise parameters are reported, starting with an insight on the physical mechanisms of DCR generation. The optical crosstalk is then discussed for its prominent role in dense GM-APD arrays and the noise analysis is concluded with the description of the afterpulsing phenomenon.

In section 1.3.4, an insight into GM-APD Photo-Detection Efficiency (PDE) is provided and its three constitute factors, Quantum efficiency (QE), Triggering probability (Tp), and Fill Factor (FF) are separately described. In section 1.3.5, the dynamic range of detection is discussed, while in section 1.3.6, the excellent timing performance of GM-APDs is described, analysing the mechanisms effecting this parameter and the critical issues to perform its measurement.

1.3.1 Dark Counts

The release of energy by a charged particle passing trough the GM-APD active region or the absorption of a photon generates electron-hole pairs that can trigger an avalanche event, leading to an output pulse that is interpreted as a detection of the particle. However, the avalanche event can be also triggered in the absence of external radiation: in this case it is called dark count event. This dark event compromises the performance of the detector because it can be erroneously interpreted as a particle detection. The Dark Count Rate (DCR) in a GM-APD should be kept low so not to spoil the Signal-to-Noise ratio of the detector.

In the next subsections the physical phenomena involved in the generation of the dark counts are reported.

Thermally generated dark counts

The properties of semiconductors are related to the energy gap (i.e. bandgap) between the valence and conduction bands, a forbidden energy region that is about $1.12\,\mathrm{eV}$ for silicon at room temperature.

Dark counts related to the effects of trapping centers with energy levels in the forbidden band are defined as SRH-generated dark counts

from the Shockley-Read-Hall theory[27, 28]. At a given temperature T, the generation/recombination rate caused by trapping centres with energy level E_t is described by the SRH equation:

$$G = \frac{{n_i}^2 - pn}{\tau_{e0}(p + n_i e^{\frac{-(E_t - E_0)}{kT}}) + \tau_{h0}(n + n_i e^{\frac{(E_t - E_0)}{kT}})} \tag{1.1}$$

where n_i refers to the intrinsic carrier concentration at the equilibrium, p and n are respectively hole and electron concentration, τ_{h0} and τ_{e0} are hole and electron recombination lifetime, E_0 is the Fermi level of silicon and k is the Boltzmann constant.

The generation-recombination of the minority carriers in the depletion region under the condition of slow variation in the carrier concentration can be described by Eq. 1.1 rewritten as

$$G = \frac{n_i}{\tau_{e0} e^{\frac{-(E_t - E_0)}{kT}} + \tau_{h0} e^{\frac{(E_t - E_0)}{kT}}} = \frac{n_i}{\tau_{g0}} \tag{1.2}$$

where τ_{g0} is the generation lifetime that represents the e-h pairs generation rate in the depletion layer.

Minority carriers that diffuse from the neutral region to the depletion region can ignite a dark event. The activation energy in this case is in the order of the Silicon bandgap (injection from neutral region).

In the presence of a high electric field the trapping rate of electrons from the valence band and the emission rate from traps to the conduction band are both increased by tunneling phenomena. This effect can be modeled considering a reduced lifetime both for electrons and holes in the so called trap-assisted tunneling. The activation energy is lower than the Energy band gap of the silicon as a consequence of tunneling [29].

Band-to-Band Tunnelling

The presence of a high electric field in a reverse biased p-n junction can also increase dark counts generation due to the band-to-band tunneling phenomenon. At low electric field, the bandgap between the valence band and the conduction band features an energy barrier that prevents the tunneling. At high electric field, the barrier between the

two bands is reduced, allowing a valence electron to make a transition from the valence band to the conduction band. Since this event happens with a horizontal transition of the electron through the band gap, this phenomenon is defined tunneling and does not requires an activation energy. As the electron transits to the conduction band, it leaves a hole in the valence band, thus an electron-hole pair is generated (tunnelling generation) [30].

Dark counts temperature dependence

A high DCR is a limiting factor that degrades the performance of GM-APDs in many application where a faint signal has to be detected. A useful approach to reduce the DCR is the cooling of the device since the dark counts generation is strongly affected by the temperature.

The generation mechanisms discussed in previous subsections exhibit different temperature dependence. Fig. 1.7 reports the temperature dependence of the dark current produced by the different generation contributions[29].

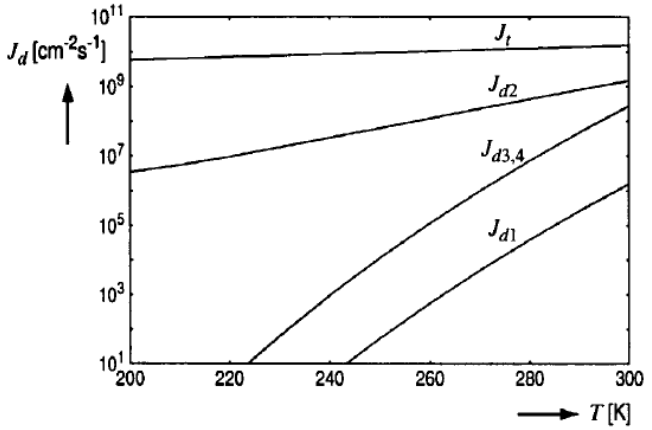

Figure 1.7: *Temperature dependence of dark currents for the different generation mechanisms [29].*

While the band-to-band tunneling J_t is only minimally affected by the temperature, the other mechanisms are strongly influenced. J_{d2} is

the dark current related to the trap assisted tunneling in the deplation layer, while J_{d1} and $J_{d3,4}$ are dark currents associated to the injection from neutral region [29].

Fig. 1.8(a) reports a sketch of the dependence on temperature of the dark counts, compared to an example of DCR measurement reported in Fig. 1.8(b). It is worth noticing how the tunnelling generation mechanisms emerges from the SRH generation only at low temperature [31].

1.3.2 Optical Crosstalk

Optical crosstalk is an unwanted phenomenon giving rise to an increase of DCR in SPAD pixelated arrays and SiPMs, leading to a degradation of the sensor performance [33], [34].

This effect is due to photon emission in silicon p-n junctions where the hot carriers generated during an avalanche event can emit electroluminescence photons [35]. The incoming primary photon triggers the avalanche multiplication leading to the generation of a large number of hot carriers in the high-field region of the SPAD. The recombination of these hot carriers can lead to the emission of a secondary photon that can ignite another avalanche after being absorbed by nearby detectors.

Since 1998, when Kindt et al. [36] proposed the first mathematical model to evaluate crosstalk probability, a lot of research has been done to evaluate the effect of crosstalk in SPAD arrays. Considering the path that a secondary photon follows from the generation point to the absorption region, optical crosstalk can be classified into two different components. Direct optical crosstalk occurs when secondary photons travel from the emitter to the detector following a straight line. Alternatively, when secondary photons reach the detector after an internal reflection at the backside surface of silicon substrate indirect optical crosstalk takes place.

A second classification can be provided in relation to the region of the detector where the secondary photon is absorbed. In order to trigger an avalanche, the hot carrier generated by the absorption of the secondary photon needs a high electric field to start the multiplication process. If the carrier is generated in the high-field region and the multiplication process occurs instantaneously, the mechanism is defined direct

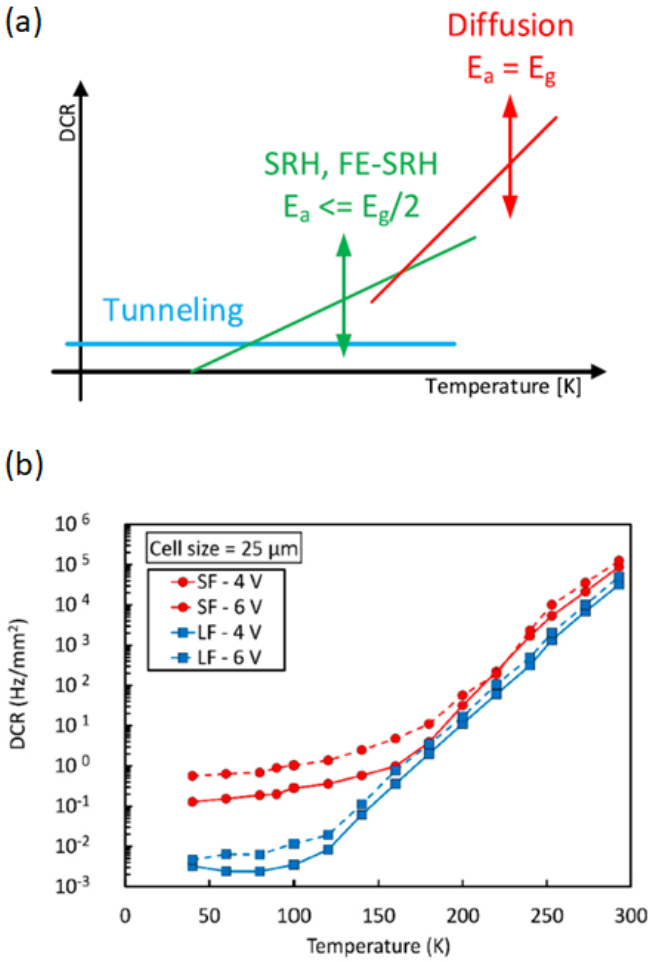

Figure 1.8: *(a) Schematic representation of DCR dependence on temperature highlithing the different generation mechanisms [32]. (b) Example of DCR measurement as a function of temperature for two different version of NUV-HD SiPMs fabricated at FBK [31].*

crosstalk. When the absorption of the secondary photon takes place in the low-field region and the hot carrier needs a previous diffusion to the high-field region to ignite the avalanche, the mechanism is defined

delayed crosstalk [32].

1.3.3 Afterpulsing

In section 1.3.1 it was mentioned that defects in the depletion layer are involved in the trap-assisted tunneling. However, their effects are not only limited to SRH generation since the presence of trap states in the depletion layer is also responsible for another form of false counts, the afterpulsing. As its name suggests, afterpulsing is a process that takes place after a primary avalanche event and triggers another avalanche. The carriers multiplication process that occurs during the avalanche produces a stream of charges that flows trough the depletion region. Some of these carriers may be captured by the defects that act as trapping centers. If these carriers are released after the diode has been recharged, they can trigger another avalanche [37].

If the afterpulsing probability is large, a self sustaining process can give raise to an iterative generation of avalanches. Even if generation centers and traps are formally the same entity, a distinction can be defined considering the different probability of the resultant process taking place. If the probability of the release of a carrier once trapped is higher than the recombination with an opposite charge, the generation center can be defined a trap [38].

It is important to notice that the position of the traps affects their probability to trigger an avalanche. Traps located closer to the high field region have higher triggering probability compared to traps located in the neutral region, since trapped carriers released in the neutral region have higher recombination probability due to their diffusion towards the high field junction before they are able to trigger an avalanche. Moreover, the energy level of a trap within the bandgap characterizes the type of carrier that is trapped with higher probability. If the trap energy level is very close to the valence band, the trap is mainly a hole trapping center. On the contrary, if the trap energy level is close to the conduction band, electrons are mainly captured and released [36].

The emission rate of a carrier from its trapped state is represented by the trap lifetime: the higher the lifetime the higher the time a carrier is maintained captured before its release. This lifetime can span several

orders of magnitude from a very short time up to hours [39].

As discussed in the previous subsection, the reduction of operating temperature may leads to a reduction of DCR; however, its effect on afterpulsing could be disadvantageous. A reduction of temperature may increase the lifetime of some short-lifetime traps that at higher temperature do not generate afterpulses. These traps at higher temperature have a short-lifetime, thus, the release of the trapped carrier happens during the recharge of the diode, so that the avalanche cannot be triggered. On the contrary, at lower temperature the lifetime increases favoring the release of the trapped carrier when the operating condition of the diode is already restored [40].

At the expense of a reduction of the maximum count rate, the afterpulsing can be reduced by varying the recharge time. If the recharge time is extended, the probability that a trapped carrier is released during the dead time of the device increases, thus the afterpulses are reduced.

1.3.4 Photon Detection Efficiency

The photon detection efficiency (PDE) is the probability that a photon impinging on the detector surface is detected and thus generates an output signal. Defined as the ratio between the number of detected photons over the number of incoming photons, it results from the product of three factors: Quantum efficiency (QE), Triggering probability (Tp), and Fill Factor (FF) of the detector [41].

$$PDE(V_{OV}, \lambda) = QE(\lambda) \times T_p(V_{OV}, \lambda) \times FF_{eff}(V_{OV}, \lambda) \qquad (1.3)$$

The QE is the probability of an impinging photon to generate an electron-hole pair, and includes the probability of the photon not to be reflected on the surface of the detector and the probability of the photon to be absorbed near the pn junction in order to let the generated carrier to reach the high field region before undergoing recombination.

Tp is the probability of the generated carrier to trigger a self-sustaining avalanche process. Tp depends on the overvoltage applied and on the position and type of photo-generated carrier, since the ionization coefficient for electrons is much higher than the one for holes [42].

The FF is the ratio of the sensitive area with respect to the total area of the detector. In Eq. 1.3 the effective fill factor (FF_{eff}) is considered in the computation of the PDE. FF_{eff} takes into account the border of the junction where the photo-generated carriers can drift laterally not triggering an avalanche [43].

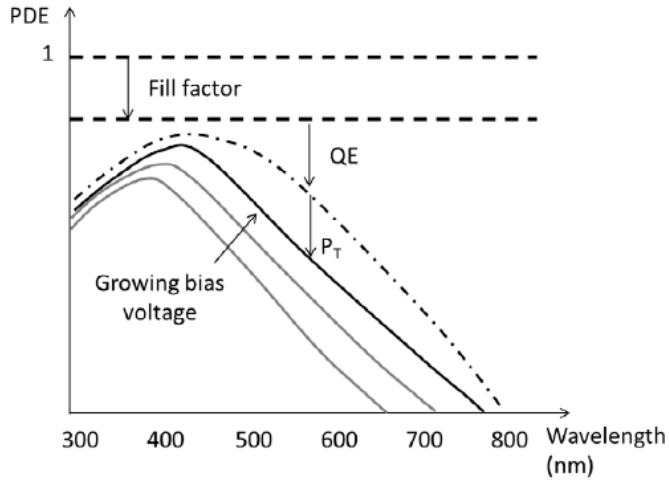

Figure 1.9: *Effect of the three factor of Eq. 1.3 composing the PDE [32].*

The PDE is one of the main parameters affecting the performance of detection systems based on GM-APDs. The effort to increase the PDE involves all the three factors of Eq.1.3 by implementing customized designs according to the specific application and by selecting the optimal operating condition.

QE can be increased by integrating an Anti-Reflecting Coating (ARC) on the surface of the detector to increase the number of photons entering the device and by engineering the pn junction to enhance the photon absorption in the spectral range required by the application[7].

Tp can be effectively increased by increasing the overvoltage V_{OV} (i.e. bias voltage exceeding the Vbd). However, a trade-off must be considered in the selection of the biasing condition since also correlated noise increases by increasing the voltage[32].

The integration of CMOS electronics to perform data processing at

the pixel level strongly affects the FF, limiting the PDE. A useful solution to partially recover this loss of sensitive area is the implementation of micro-lenses on the surface of the detectors to increase the effective FF [44].

1.3.5 Dynamic range

GM-APDs are capable to detect very faint light signals but on the other hand their linearity response to an incoming photon flux is limited by a saturation level that is related to the dead time of the detector.

The saturation photon flux is inversely proportional to the dead time, that is the time interval between the avalanche quenching and the restoration of the bias condition. However, also the afterpulsing has to be taken into account when considering the saturation flux, since it may reduce its value. Including the afterpulsing probability, the saturation flux can be defined by the following formula:

$$\phi_{S,Max} = \frac{1 - P_{AP}}{T_d} \tag{1.4}$$

where $\phi_{S,Max}$ is the saturation flux of photons, P_{AP} is the afterpulsing probability and T_d is the dead time [45].

In Fig. 1.10 the output of a CMOS SPAD array for 3D imaging is reported. At an optical intensity of about $100\,\mathrm{mW\,cm^{-2}}$ the detector response starts to lose linearity, approaching the saturation level. It is worth noticing that the dynamic range of detection spans several orders of magnitude.

1.3.6 Single Photon Time Resolution

Single Photon Time Resolution (SPTR) is the timing jitter in the measurement of the arrival time of the detected photon. As described in section 1.1, the build-up and spreading of the charge cloud are fast mechanisms, allowing GM-APDs to reach very good SPTR in the subnanosecond range down to few tens of picoseconds[47].

The SPTR is usually evaluated by acquiring the histograms of the arrival time of detected photons with a Time Correlated Single Photon Counting (TCSPC) system. An adequate statistics of detected photons

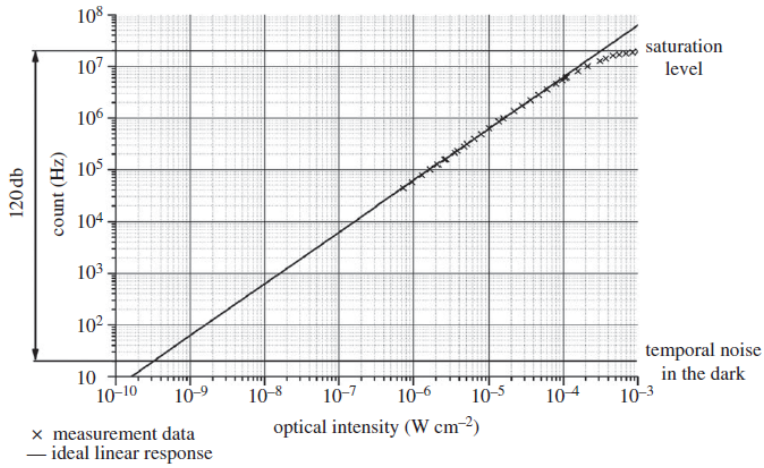

Figure 1.10: *Photo renspose of a CMOS SPAD array for 3D imaging [46].*

should be collected with the device illuminated by a ps-width pulsed laser strongly attenuated in order to avoid pile-up distortions[48]. Since SPTR is described by the distribution of arrival time, it is measured in terms of Full-Width at Half Maximum (FWHM).

In order to be able to detect the excellent SPTR of GM-APDs, the avalanche has to be detected at the beginning of the spreading phase, when the multiplication process is still confined within a small area around the photon absorption point, by employing a fast pick-up circuit and selecting a low threshold[49].

The typical SPTR of a SPAD is composed of a main peak usually followed by a tail caused by the carriers absorbed in the neutral region that have to diffuse towards the active region to trigger an avalanche [50].

In Fig.1.11 the timing jitter as a function of the excess voltage is reported for a $1\times1\,\mathrm{mm}^2$ SiPM at two different wavelengths. The SPTR at $425\,\mathrm{nm}$ is better than the SPTR at $850\,\mathrm{nm}$ according to the different absorption length of these two wavelengths in silicon. At shorter wavelengths (corresponding to a lower absorption depth) the carrier generation in the neutral region is lower compared to longer wavelengths (featuring a larger absorption length), thus the diffusion tail in the SPTR

histogram is reduced. By increasing the V_{OV} the depletion layer extends reducing the amount of diffused carriers, thus reducing the tail of the distribution as shown in the inset in Fig. 1.11, where the timing response at $850\,\mathrm{nm}$ for two different biases is reported[51].

The relationship between the timing jitter (σ_t) and the shape of the signal from a SiPM is described by eq. 1.5, in terms of the slope of the signal at the threshold crossing point (f'_{th}) and amplitude of the combination of electronic noise and baseline fluctuation (σ_n)[52].

$$\sigma_t = \frac{\sigma_n}{f'_{th}} \tag{1.5}$$

As a direct consequence, the low pass filtering effect of the cell capacitance of a SPAD degrades the timing jitter, since it lowers the rise time of the signal output. Therefore, small-size SPADs have better timing response when compared to bigger SPADs due to their lower capacitance. For the same reason, SiPMs exhibit worst timing response when compared to a SPAD having the same size of the cell composing the SiPM[51].

1.4 Single Photon detection

The detection of very weak signals is the main strength of GM-APDs, and the reason why they are also known as Single Photon Avalanche Detectors. With reference to the different operation regions of a photodetector illustrated in Fig. 1.1, the detection limit in terms of number of photons are reported in Table 1.1.

Table 1.1: *Minimum detectable signal of different type of photodiodes. Table edited from [53]*

Photodetector type	**Minimal detectable singnal**
Silicon PIN photodiodes	200-300 photoelectrons
Silicon APD	10-20 photoelectrons
Silicon GM-APD	1 photoelectron

The single-photon sensitivity of GM-APDs is a direct consequence

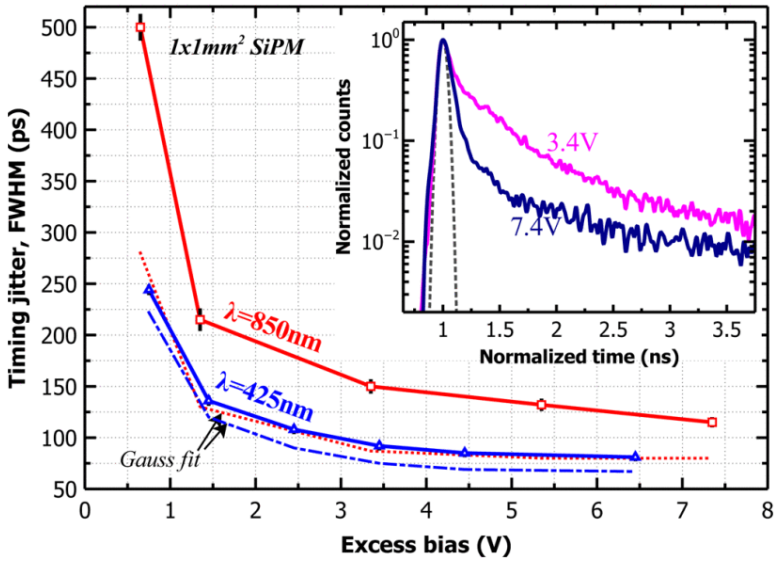

Figure 1.11: *Excess bias dependence of SPTR of a* $1\times1\,\mathrm{mm}^2$ *SiPM at* $\lambda = 425\,\mathrm{nm}$ *and* $\lambda = 850\,\mathrm{nm}$. *In the inset: SPTR histograms at two different excess bias voltages at* $\lambda = 850\,\mathrm{nm}$ *[51].*

of their high gain that make these detectors able to generate a measurable signal starting from the absorption of a single photon.

The efforts to detect vary faint optical signals have been fostered the development of many single-photon sensitive detectors in which different physical mechanisms are exploited to generate a detactables signal from the interaction with an incoming photon [54].

In PhotoMultiplier Tubes (PMTs) an electron extracted from a photocathode by an incoming photon is multiplied by means of the secondary emission multiplication process by a sequence of dynodes to generate a measurable signal [55]. MicroChannel Plates (MCPs) exploit the same working principle of PMTs, the secondary emission process, with the possibility to provide a spatial resolution, since they are composed of several microchannels [56].

Quantum Dots Field-Effect Transistors (QDFETs) rely on an optical absorber and quantum dots placed between the gate electrode and the conduction channel in a Field-Effect Transistor (FET). These detec-

tors exploit the changes of the conductance when the photo-generated charges are trapped in the quantum dots layer [57].

Superconducting Single-Photon Detectors (SSPD) are composed of a narrow superconducting wire biased just below the critical current density. The absorption of a photon in the superconductor promotes a local change in the resistance, thus increasing the current density in adjacent regions. The resistance change then spreads over all the detector width, thus causing a voltage drop across the detector, that can be amplified with an external circuit. [58].

Compared to other single-photon sensitive detectors, GM-APDs have the advantages of low bias voltage requirement, are insensitive to external magnetic fields and feature a small size, that make them the best performing detector in many applications [22].

1.5 Applications

In this section an overview of GM-APDs detection systems is reported in order to provide examples of the advantages of this detectors in different application fields.

The performance of GM-APDs in terms of sub-nanosecond time resolution and single photon sensitivity make them suitable for a wide range of applications and their integration with mixed-signal circuits in Deep-SubMicron (DSM) CMOS technologies is widening their use in the devolopment of high-performance imaging systems [59].

In the field of Biophotonics, GM-APDs can be used to detect the emission, the absorption and the scattering of light in order to investigate biological specimens ranging from single molecules up to complex biological systems thanks to their dynamic range [60].

CMOS technology is a powerful tool to design GM-APDs arrays with a geometry customized for the specific applications. The arrangement of detectors in a line sensor is an excellent solution for spectroscopic measurements, since it can be easily coupled with a grating to spread the acquired signal onto the whole array to detect the spectrum of the signal under investigation [61, 62, 63, 64, 65, 66], while the implementation of a 2D array is well suited for imaging sys-

tems [67, 68, 69, 70].

Several complex digital processing circuits have been integrated with GM-APDs to achieve high-performance functionality such as per-pixel Time-to-Digital Converters (TDCs)[71], gated counters[61], time-gated memories[62] and in-pixel center-of-mass computation[72].

Raman Spectroscopy (RS) is an investigation technique commonly used to provide a fingerprint of molecules in order to identify them. In Raman spectroscopy the weak inelastic spectrum from a sample illuminated with a monochromatic laser beam is acquired. A way to increase the amplitude of the weak Raman signal is to promote the inelastic scattering using the plasmonic resonance of nanoparticles in the so-called Surface-Enhanced Raman Spectroscopy (SERS) [73].

In Fig. 1.12, the block diagram of the per-pixel TDC co-integrated with a linear 4×128 SPAD array designed for Raman spectroscopy is depicted. The flash TDC is based on one common delay line for all the 512 channels of the system. The Raman signal is recorded by acquiring the times of arrival of the photons detected by the SPADs with respect to a synchronization signal generated by the laser source used to irradiate the sample under investigation.

TDC dead time following the sampling of an event limits the acquisition of one detected photon for every laser excitation pulse. The main effect of this limit is the presence of pile-up distortion when acquiring a signal with the TCSPC technique. This distortion is the main drawback in TCSPC systems and the acquisition frame rate should be limited in order to avoid this undesired effect[48].

Abbas et al.[67] have integrated a multi-event folded-flash TDC in a CMOS SPAD array which eliminates the converter dead time allowing the system acquisition rate to be further extended.

Within the framework of Proteus project, a research project combining several interdisciplinary research centres with the aim to develop a revolutionary technology that will provide a quick bedside diagnosis and management of lung diseases in the clinical environment, SPAD arrays with in-pixel CMOS data processing circuits have been proposed as detector for Raman Spectroscopy (RS) and Fluorescence Lifetime Imaging (FLIM) [74].

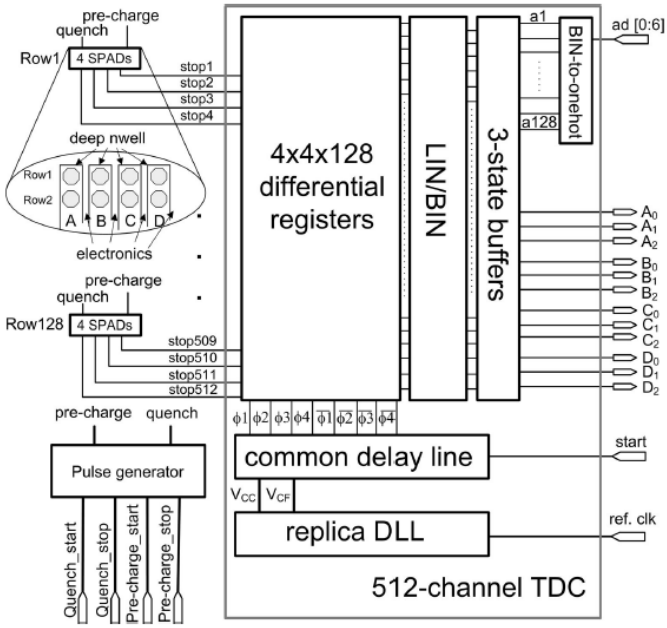

Figure 1.12: *Block diagram of the 512-channel per-pixel Time-to-Digital Converter implemented in a* 4×128 *SPAD array [71].*

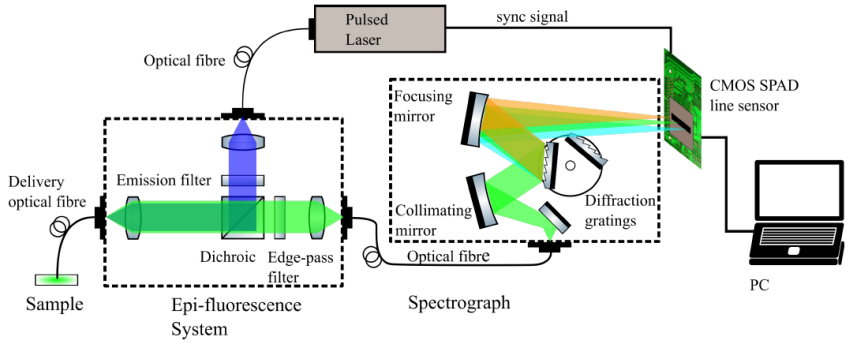

Figure 1.13: *Schematic representation of the time-resolved spectroscopy composed of an epi-fluorescence light collection system, spectrograph and CMOS SPAD line sensor [75].*

The Raman-spectroscopy endoscope depicted in Fig. 1.13 is composed of a pulsed laser, an epi-fluorescence light coupling and collecting system, a spectrograph and a CMOS SPAD line sensor [75].

The SPAD linear array sensor designed in $130\,\mathrm{nm}$ CMOS process features two different arrays with detectors optimized for the range from $450\,\mathrm{nm}$ to $550\,\mathrm{nm}$ and from $600\,\mathrm{nm}$ to $900\,\mathrm{nm}$ in order to extend the spectral range of use [72].

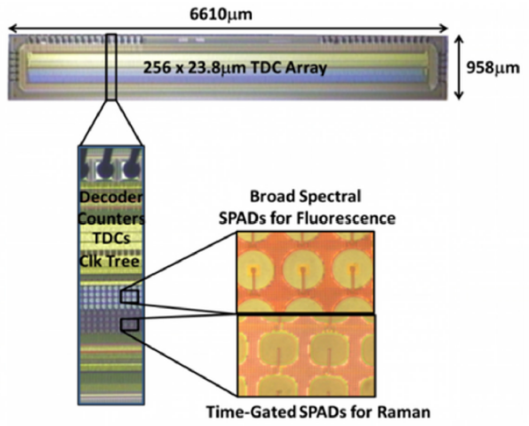

Figure 1.14: *Micrograph of the SPAD linear array for the Raman spectroscopy [72].*

A substantial limitation of Raman spectroscopy performed with a microendoscope is the scattered spectrum of the fibre that is acquired together with the sample signal. The different profiles of background fluorescence, fibre Raman scattering, and SERS signal can be resolved in time thanks to the good time resolution of SPAD sensor in order to separate in post processing the SERS signal from the background [76].

Background suppression is performed defining three different time windows along the histogram axis: in Fig. 1.15 a 3D representation of the acquired signal with the different time windows is depicted. The Dark Counts (DC) time window is defined to extract the dark counts of the sensor, that are then subtracted pixel-wise to take into account the differing count rates in the line array. The fibre time window is defined to extract the Raman spectrum of the fiber that is subtracted to the signal

in the SERS time window [76].

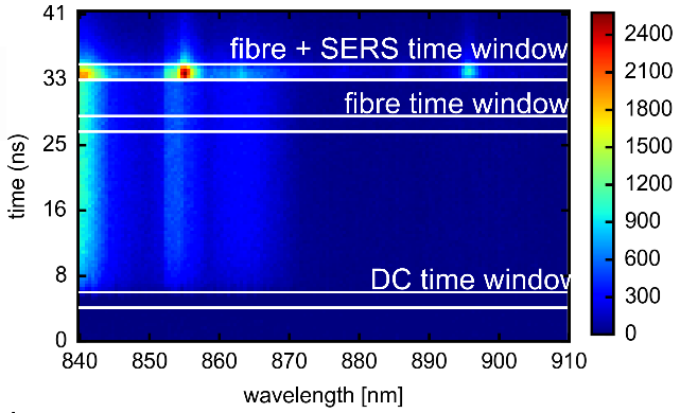

Figure 1.15: *3D representation of the time resolved measurement adapted from [76].*

This suppression could be performed at the pixel level by including time gatin circuits in each pixel. Pixel level suppression enables a reduction of the readout data stream; however, it is not a significant improvement since the measurement rate is limited by photon budget in TCSPC application [76].

Fluorescent molecules are characterized by a specific lifetime, defined as the mean time required by the molecule to decay from the excited to the ground state. Fluorescence lifetime imaging microscopy (FLIM) is a microscopy technique in which the microscopic structure under investigation is resolved by detecting the different lifetime of the fluorescent molecules present in the sample [77].

The single-photon sensitivity of GM-APDs plays a significant role in biomedical application where living cells are analysed, since the intensity of the excitation light source has to be kept weak in order to avoid photo-bleaching or photo-damages of the sample during the measurement [78].

A line sensor composed of 512×16 SPADs designed in a $130\,\mathrm{nm}$ CMOS technology has been characterized trough a spectral fluorescence lifetime imaging of different fluorophores with distinctive lifetimes. The block diagram of the line sensor is reported in Fig. 1.16.

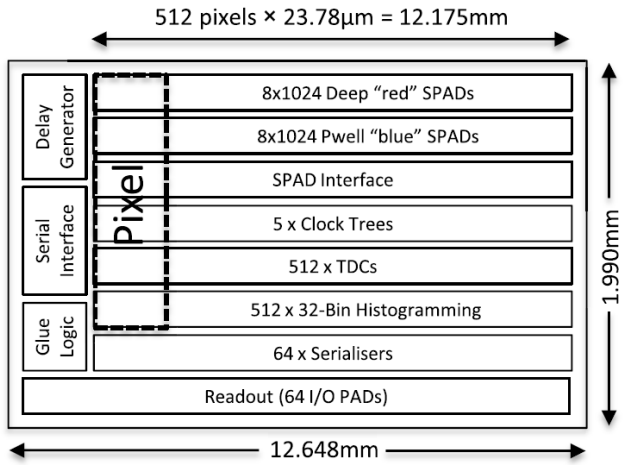

Figure 1.16: *Block diagram of the line sensor with the integrated electronics enabling the sensor to perform FLIM measurement simultaneously in both time and spectral domains [79].*

Several CMOS GM-APDs arrays[80, 81] have been proposed as detectors for Positron Emission Tomography (PET) for their insensitivity to magnetic fields, allowing the combination with Magnetic Resonance Imaging (MRI)[82], and for their sub-nanosecond time resolution in Time-of-Flight (TOF) PET, which allows improving the image quality with respect to PMT-based systems[83].

PET is a powerful imaging technique able to provide metabolic information of the body by using radioactive tracers that concentrate in a specific tissue. The decay of a radioactive atom of the tracer generates a positron that after a short distance emits a pair of 511-keV gamma photons travelling in opposite direction. The distribution of the radioactive tracer is reconstructed by the energy discrimination and the time coincidence detection of gamma photons[84].

Detectors for PET scanners are usually photo-detectors coupled with a scintillator that converts gamma photons into light. GM-APDs are excellent candidates for PET scanners thanks to their high sensitivity and fast time response, that enable good signal to noise ratio and high spatial resolution [85].

An 8×16 pixel array based on CMOS small-area Silicon PhotoMultipliers (mini-SiPMs) detectors for PET applications was reported by Braga et al. [80]. The basic building block of the detector is a digital mini-SiPM composed by 12×15 cells arranged in a group of four with shared integrated electronics, reaching a fill-factor of $35.7\,\%$. In Fig. 1.17 the pixel arrangement is reported with the DAta MAnaging Circuit (DAMAC), that handles gamma photon energy and timestamps, highlighted.

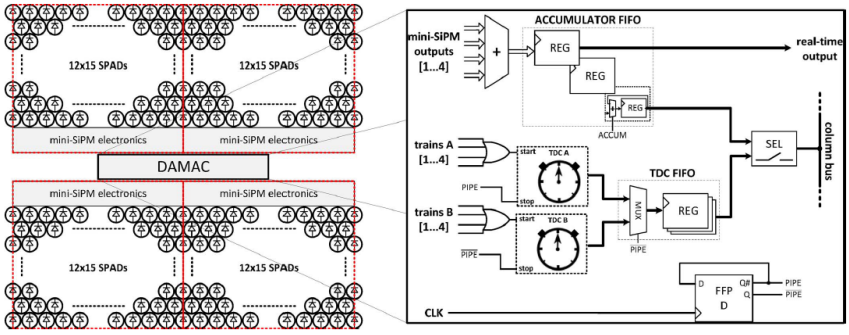

Figure 1.17: *Pixel building block with the simplified DAMAC [80].*

In association with fast Laser Diodes transmitters, the good timing performance of GM-APDs coupled with CMOS integrated TDC data processing make them well suited for Time-of-Flight measurement systems for 3D imaging and distance range measurements.

A 9×9 SPAD array with a 10-channel TDC was proposed by Jahromi et al. [69] as receiver in a 3D imaging system to map the target surface in an xy plane (perpendicular to the optical axis), while Δt is used to calculate the distance into the direction z (the optical axis). In Fig. 1.18 the receiver chip is shown with a magnified inset of the SPAD array, that is surrounded by the front-end electronics and the 10-channel TDC. In the chip, one channel is dedicated to detect the Laser synchronization signal as start of the measurement and 9 channels to detect the stop signal from a selected combination of 9 different 3×3 SPAD sub-arrays in order to measure the entire 9×9 array.

Fig. 1.19 reports a 3D image taken with a 64×64-Pixels digital SiPM

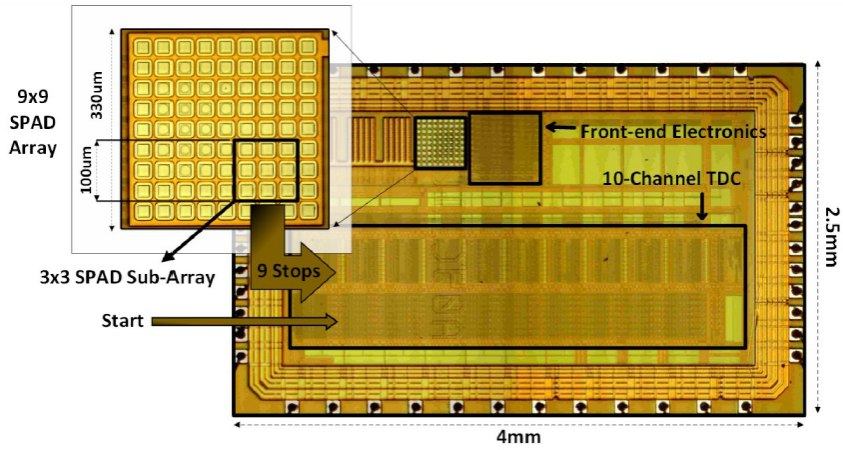

Figure 1.18: *3D imager receiver chip based on a* 9×9 *SPAD array [69].*

TOF sensor designed by Perenzoni et al. [70] for spacecraft navigation and landing. With a reconfigurable illuminating optics, the sensor can work as 3D imager at short distance by using a diffused illumination and as an altimeter at long range up to $6\,\mathrm{km}$ by collimating the laser in a single spot and read the array as a unitary detector. The in-chip electronics features also a DCR evaluator by measuring metal shielded SPADs in order to adjust the working SPAD bias voltage according to the environmental condition.

In the framework of SUPERTWIN European H2020 project aiming to the development of a super-resolution all solid-state microscope, a CMOS SPAD array has been proposed as image sensor in the field of quantum imaging for the detection of entangled photons. This innovative approach allows exceeding the Abbe diffraction limit resolution by exploiting the measurement of the spatial second-order correlation function of entangled two-photon states [86].

Coupled with an attenuated LED as light source, GM-APDs have been also proposed in criptography as True Random Number Generator (TRNG) with high quality performance in therms of high bit rate by exploiting the arrival time of photons[87] and good stability at different working conditions[88].

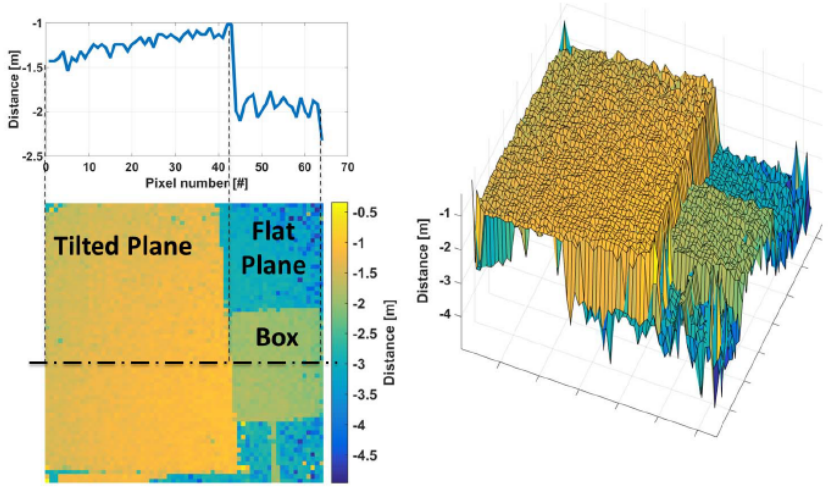

Figure 1.19: *3D Time-of-Flight image acquired with 30k points [70].*

Embedded CMOS electronics in SPAD array sensors is an effective development to increase system performance by implementing high level on-chip data processing. One of the main drawbacks for the current state of the technology is represented by embedded electronics for data processing, that extends for a great portion of the pixel area, limiting the active area of the sensor. Development of SPAD arrays with the 3D-stacking of detector layer and data processing layer can be used to better optimise the pixel design, ensuring a good pixel factor[89, 65].

CHAPTER 2

Particle Detectors

In this chapter an innovative prototype for particle tracking based on a two tier Geiger-Mode Avalanche Photo Diode array with in-pixel coincidence is reported.

In the first section, the interaction of radiation with silicon is briefly summarized, describing the different effects of charged particles, photons and neutrons. An overview of silicon solid-state particle detectors is then provided, together with the state of the art in particle detectors based on GM-APDs working in coincidence. In the last section of the chapter, a complete description of the prototype is reported, describing its architecture from the pixel level to the top level.

This innovative particle detector was designed and developed in the framework of APiX2 and ASAP projects founded by Istituto Nazionale di Fisica Nucleare (INFN).

2.1 Radiation Interaction with Silicon

The basic physical mechanism of radiation sensing in silicon-based detectors is the collection of free charges generated by the interaction of radiation with the silicon atomic structure. Depending on the detector characteristics, the position, the amount of released energy or both can be detected [90].

In order to better understand the mechanisms of detection, in this section the interaction of different types of radiation with silicon is discussed.

2.1.1 Charged Particles

The interaction of a charged particle with the silicon lattice arises from Coulomb forces between the particle and the electron cloud of the silicon atoms. During this interaction the particle loses part of its energy, promoting the ionization of the silicon atoms. The average energy loss can be estimated with the Bethe-Bloch equation [91]:

$$-\frac{dE}{dx} = \frac{4\pi e^4 z^2}{m_0 v} NZ[ln\frac{2m_0 v^2}{I} - ln(1-\frac{v^2}{c^2}) - \frac{v^2}{c^2}] \tag{2.1}$$

This equation relates the energy loss with the charge and the mass at rest of electron (e and m_0), the atomic charge and the velocity of the incoming particle (z and v) and the density and atomic number of the media (N and Z). I is a term that takes into account the ionization/excitation potential of the material that is experimentally evaluated. From eq. 3.1 the minimum energy deposited in the medium can be derived, leading to the definition of Minimum Ionizing Particles (MIPs), namely particles that provides this minimal energy loss [91].

It is worth mentioning that the energy deposition is affected by statistical fluctuations related to the number of collisions during the interaction. Moreover, in rare cases δ-rays or δ-electrons produced in the interaction can have sufficient energy to ionize the silicon atoms. Thanks to these mechanisms, the energy transfer distribution follows a Landau distribution in which the most probable energy transfer is generally $30\,\%$ lower than the average value of the distribution [92].

In silicon the average energy necessary to generate an electron-hole pair is $3.6\,\mathrm{eV}$, that is about three times its energy bandgap ($1.12\,\mathrm{eV}$). This extra amount of energy is involved in the creation of phonons that thermally dissipate the energy in excess. Considering a MIP releasing this minimal energy, 108 electron-hole pairs are generated in average in $1\,\mu\mathrm{m}$ of silicon with 76 as most probably value [93].

2.1.2 Electromagnetic Radiation

The interaction of electromagnetic radiation with silicon differs from the interaction with charged particles.

A photon beam travelling into a material is attenuated following the Beer-Lambert law:

$$I(x) = I_0 e^{-\frac{x}{\mu}} \tag{2.2}$$

where I_0 is the intensity of the beam before entering the material, x is the depth coordinate in the material and μ is the attenuation length that depends on the material and on the photon energy. In Fig. 2.1, the absorption depth of photons in silicon as a function of wavelength is reported for the ultraviolet, visible and near infrared part of the spectrum..

In Fig. 2.2 the probability of photon absorption in a $300\,\mu\mathrm{m}$ silicon layer is reported as a function of the photon energy for X and γ-rays. The three different processes that may take place in silicon are highlighted: photoelectric absorption, Compton scattering and pair production. According to the photon energy, the three different processes have a different absorption probability, with the photoelectric effect dominant at lower energy while pair production is attainable only at higher energy [95].

2.1.3 Neutrons

Being uncharged particles, the interaction of neutrons within silicon devices occurs mainly with the silicon nuclei, thus they can penetrate for relatively long distances before being absorbed or scattered. The probability of interaction between neutrons and nuclei is described by the cross section σ expressed in barn ($10^{-24} cm^2$). For slow neutrons

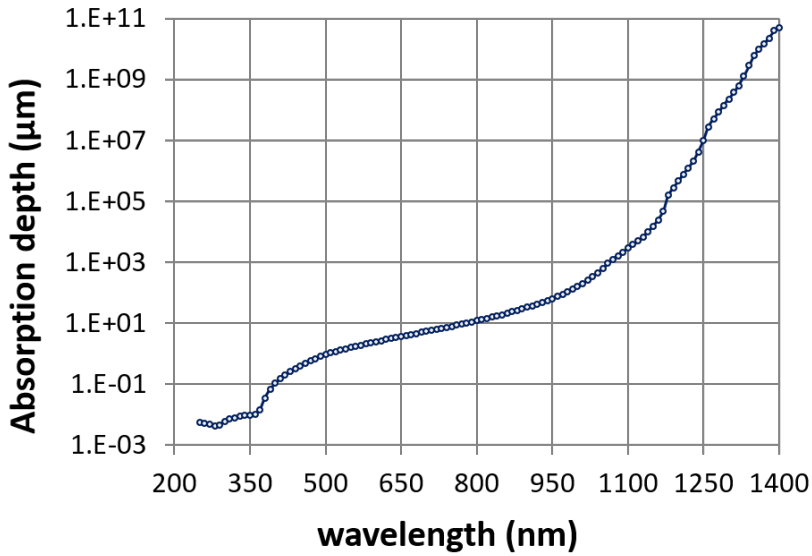

Figure 2.1: *Absorption depth in silicon with respect to photon wavelength. Edited from [94].*

the cross section is high, thus, nuclear reactions are promoted. The scattering is, on the contrary, the dominant interaction for fast neutrons which exhibit a low absorption cross section.

In table 2.1 the classification of neutrons according to their energy is reported.

2.1.4 Radiation induced effects

Radiation detectors operating in highly radioactive environment suffer from degradation of performance as a consequence of radiation damage generated in silicon during the radiation exposure[97].

Radiation induced effects of particles on silicon radiation detectors are generally classified in two different groups:

- Bulk damages

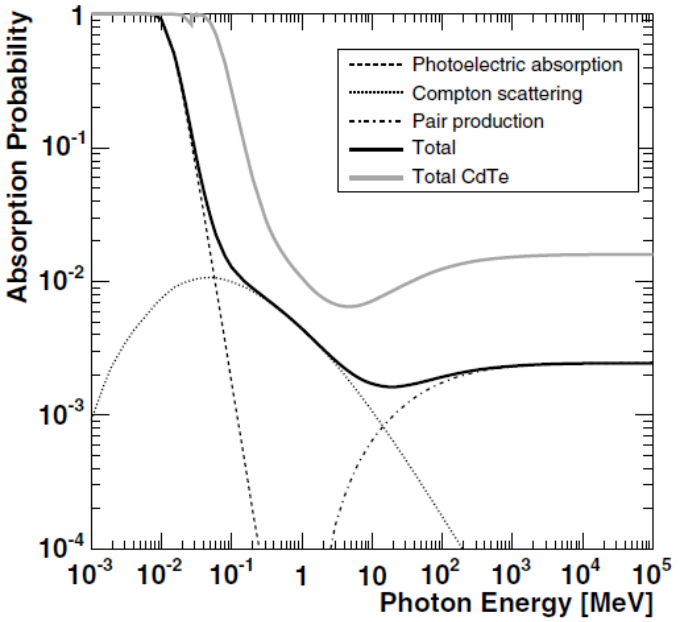

Figure 2.2: *Photon absorption probability for* $300\,\mu\mathrm{m}$ *silicon as a function of the photon energy [95].*

- Surface damages

Bulk damages

The interaction of incident particles with silicon bulk may lead to the displacement of silicon atoms from their lattice position, producing interstitial or vacancy defects. A minimum threshold energy of $25\,\mathrm{eV}$ is required to remove a silicon atom from its lattice position. Different particles need different energy to be able to perform this displacement, electrons need an energy of at least $260\,\mathrm{keV}$ while protons and neutrons require only $190\,\mathrm{eV}$ because of their higher mass [95].

In order to compare effects induced by different radiation sources that feature different mechanisms of interaction, radiation damages is related to the effect of a monoenergetic neutron flux with an energy of $1\,\mathrm{MeV}$. An energy-dependent hardness factor k is used to converts the

Table 2.1: *Classification of neutron according to the energy [96]*

Neutron Classification	Energy (meV)
Ultra-cold	0.00025
Cold	1
Thermal	25
Epithermal	1000
Fast	>1000

fluence of a particle into a neutron equivalent fluence [98].

The macroscopic effects of bulk damage are the increase of the leakage current, the change of the space charge in the depleted region and charge trapping. Leakage current increases as a consequence of new levels in the forbidden band introduced by the defects, that enhance the generation-recombination mechanisms. These forbidden levels may also act as trapping centres for free charges, with the capture probability that depends linearly with the fluence [99].

The effective doping concentration of the bulk can change according to the production of defects since these defects can be charged, thus the doping concentration can vary with respect to the radiation fluence. In Fig.2.3, the fluence dependence of effective bulk doping is reported. It is shown that, with increasing fluence, firstly the n-doping is reduced until the space charge is almost dissolved. By further increasing the fluence, the semiconductor behaves like a p-type material, since an inversion of the doping profile occurred [95].

Surface damages

Radiation interaction with silicon detectors produces effects also on the silicon oxide surface layer and in the interface between the silicon and the dielectric. Defects on the surface can create levels in the forbidden band, leading to an increase of the surface current, while charges trapped on the oxide can alter its passivation characteristics [101].

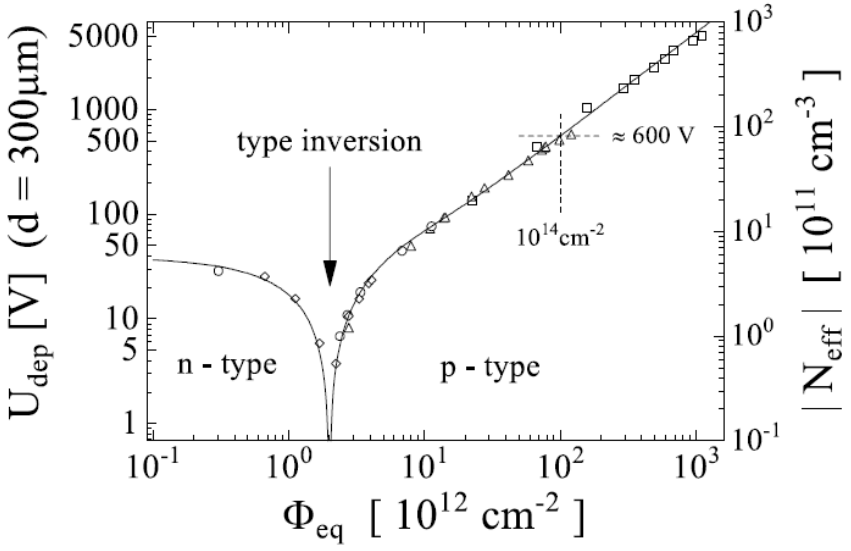

Figure 2.3: *Depletion voltage and absolute effective doping variations with respect to the normalized fluence on a* 300 μm*-thick silicon sensor after irradiation [100].*

2.2 Silicon Particle Detectors

The development of pixel detectors for particle physics experiment have been driven by the requirement of studying short-lived particles in modern particle accelerators, being able to reconstruct collision and decay vertices with good space and time resolution [95].

In addition to High Energy Physics (HEP) experiments, silicon radiation detectors are also used in medical imaging applications: for example in digital X-ray imaging, gamma detection in PET scanners and as beta-gamma digital imaging probe for radioguided surgery[102, 85, 80, 103].

In Fig. 2.4 the decay pattern of a short-lived particle is reconstructed by using three double-sided microstrip detectors [95].

Silicon particle detector can be divided into three main classes:

- Segmented Silicon Detectors
- Hybrid Pixel Detectors

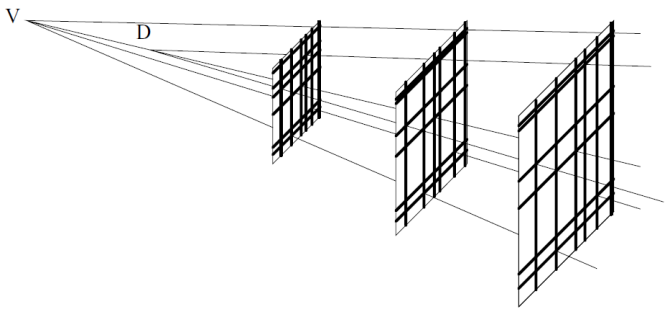

Figure 2.4: *Detection of short-lived particle decay track acquired by three double-sided microstrip detectors [95].*

- Monolithic Pixel Detectors

Microstrip detectors are caraterized by a segmentation in thin parallel strips of one (single-sided) or both (double-sided) device electrodes. The device is produced by implanting p^+-doped regions arranged in strips on a n-type substrate and by patterning metal electrodes covering the implants spaced with oxide layers. The deplation layer defines the active volume of the detector: as a particle crosses it or a photon is absorbed in it, the charged carriers generated in the event are detected as a current signal [104].

Compared to 2D pixel arrays, microstrips detectors require a lower number of readout channels, simplifying the connection of the sensing electrodes with the electronics.

Pixel detectors are characterized by electrodes segmented in a chessboard configuration in order to reconstruct 2D information. In the hybrid configuration, the detectors are realized by the post-production integration of the sensor tile with the electronics readout which were previously fabricated on different substrates in order to optimize their production. Their main limitation in terms of pixel size is related to the complexity of the electronics that have to fit the pixel detector size.

Monolithic detectors are produced by implementing both detectors and electronics in the same technological process. This approach can lead to the improvement of noise performance related to the reduction

of the capacitance of each pixel, avoiding also the high-density interconnection required by hybrid detectors. On the other hand, since the technological process cannot be fully optimized for both sensor and electronics their design requires a trade-off between the performance of sensors and of the electronics [95].

2.3 Geiger-Mode APD Particle Detectors

The increasing complexity of particle tracking systems at collider experiments demands for high performance detectors with high granularity and position accuracy, low material budget and power consumption[1].

The reduction of material budged is an important challenge to be addressed in order to avoid tracking deterioration due to multiple scattering within the detector. The development of thin hybrid pixel and Monolithic Active Pixel Sensors (MAPS) has been driven to pursue this goal[105, 106].

The DCR of GM-APDs has prevented their use as particle tracking detectors, since it is not possible to discriminate a particle-generated event from a dark event. To overcome this issue, the use of GM-APDs in coincidence has been proposed. An experimental validation of the coincidence detection was conducted using SiPM detectors by D'Ascenzo et al.[107] shortly after the first coincidence detection proposal patented by Saveliev [108]. In Fig. 2.5 the schematic representation of the experimental setup is depicted. The prototype, composed of two SiPMs with $1\times1\,\mathrm{mm}^2$ active area mounted face to face at a distance of tens of microns and placed between two scintillator counters of $10\times10\,\mathrm{cm}^2$, was exposed to a $120\,\mathrm{GeV}$ proton test beam in the CERN North Hall area. The coincidence detection events of the SiPMs were compared with a trigger signal formed by the coincidence between the counters. This first experiment demonstrated the feasibility of the coincidence approach, paving the ground to the development of a GM-APD particle tracker with low material budged[107].

A 3D-SiCAD (Silicon Coincidence Avalanche Detector) prototype composed of test structures and small pixel arrays was desgined by a reserch group of the University of Lyon and fabricated in CMOS High-Voltage 0.35 μm technology. A first characterization study for

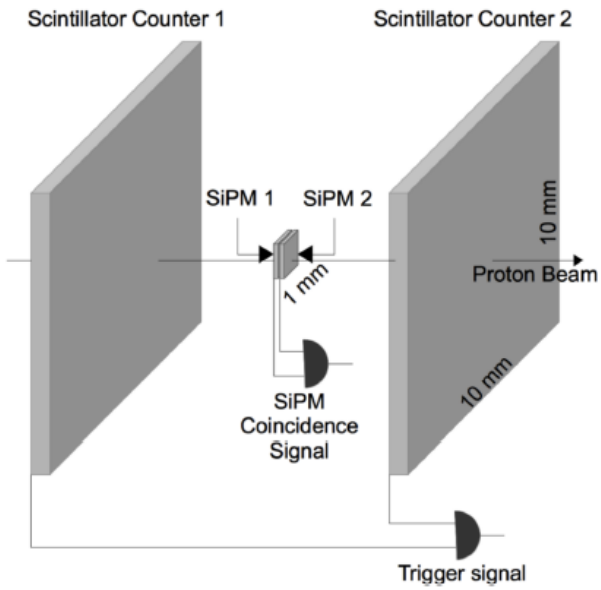

Figure 2.5: *First experimental setup of coincidence detection with SiPMs[107].*

the detection of β^- particles emitted by a ^{90}Sr source was performed to demonstrate its functionality[109].

2.4 APiX Projects

The research activity reported in this dissertation has been performed in the framework of APiX2 and ASAP projects funded by Istituto Nazionale di Fisica Nucleare (INFN). These projects are carried out by research units from the Universities of Trento, Pavia, Siena and Pisa and the INFN sections of Pavia, Pisa and Trento Institute for Fundamental Physics and Applications (TIFPA).

APiX2 project was proposed with the purpose of providing a proof-of-concept implementation and preliminary evaluation of a new type of silicon sensor formed by two vertically-aligned pixelated arrays based on Geiger-Mode Avalanche Photo Detectors, suitable for particle track-

ing and imaging. The proposed device exploits the coincidence between two simultaneous avalanche events to discriminate between particle-triggered detections and dark counts[110].

ASAP project has the goal to continue the development started with APiX2 by implementing technological improvements to increase system performance in terms of efficiency and dark count reduction[111].

In the framework of APiX projects, avalanche detectors were implemented using two different foundries. While this work is focused on the characterization of a prototype detector fabricated in a $150\,\mathrm{nm}$ CMOS process, another explorative chip has been fabricated and characterized in a $180\,\mathrm{nm}$ CMOS process[112].

2.5 Single Layer Chip Architecture

The basic working principle of the coincidence detection implemented in the APiX prototype pixel is reported in the schematic of Fig. 2.6. A charged particle crossing both the GM-APDs integrated in a pixel triggers an avalanche in both devices. The output signal of each detector reaches the coincidence electronics, that allow the device to discriminate the particle detection from dark events.

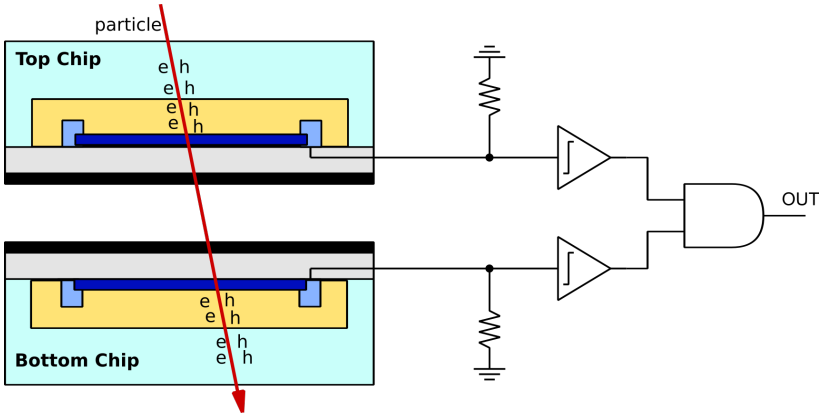

Figure 2.6: *Basic working principle of the coincidence detection of the APiX prototype pixel.*

This cell-to-cell coincidence ensures a strong DCR reduction with

respect to each single layer. The dark count rate in coincidence (DCR_c) can be calculated as follow:

$$DCR_c = DCR_{top} \times DCR_{bottom} \times 2\Delta T \tag{2.3}$$

with DCR_{top} and DCR_{bottom} the dark counts of top layer and bottom layer respectively and ΔT the coincidence time resolution. Since the coincidence time resolution can be set in the order of a few nanoseconds, the coincidence dark count rate can be reduced by many orders of magnitude compared to the dark count rate of each single layer.

2.5.1 Detector Cross-section

The particle detector was designed with two types of SPADs and various geometries to increase the amount of information obtained from the test of the prototype.

In Fig. 2.7, the cross section of both types of detectors is shown. Both types of detectors were fabricated starting from the same p-substrate and using only doping profiles included in the CMOS flow. One of the detectors is based on a shallow p^+/nwell junction, hereafter defined as Type 1 detector, while the second detector is based on a deep pwell/n-iso graded junction (Type 2 detector).

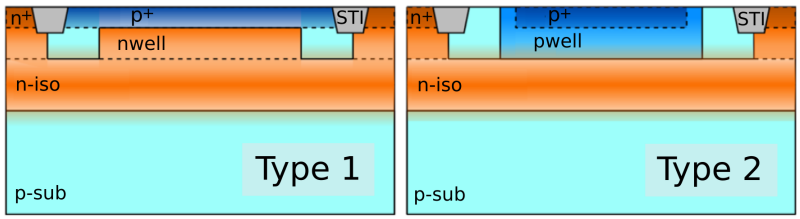

Figure 2.7: *Cross section of the two different types of detector integrated in the APiX prototype [113].*

In the Type 1 detector, the shallow junction is made of a p^+ region implanted in an nwell. The region without well implantation at the border of the junction works as a guard ring to confine the high electric field in the active region, preventing Premature Edge Breakdown (PEB).

The deep graded junction of the Type 2 detector is defined by a pwell implanted inside a n-iso region. An ohmic contact with the metallization is obtained with an implanted p^+ region at the surface of the pwell. The presence of a surface p^+ layer is effective in reducing the surface-generation contribution of the Dark Count Rate, since the electrons generated at the silicon/oxide surface recombine before reaching the active region where they would have triggered an avalanche. The region at the border of the junction without well implantations defines a virtual guard ring, that is shielded from the p^+ implantation by a poly-Si ring. The poly-Si is biased at the same potential of the p-type region by connecting it to the detector anode[114].

A design feature in common between the two types of devices is the n-iso layer, that isolates the devices from the p-substrate. This isolation allows the chip to be thinned down to few microns without compromising the detector functionality, in order to assess the low material budget required in HEP experiments.

2.5.2 Array Architecture

The pixel array was designed and fabricated in a standard $150\,\mathrm{nm}$ CMOS process with both types of detectors integrated in the array. The whole array is composed of 768 pixels arranged in 16 rows and 48 columns. Rows from 1 to 8 are composed of Type 1 devices while rows from 9 to 16 are composed of Type 2 devices.

Each pixel of the array has $50\,\mu\mathrm{m}$ width and $75\,\mu\mathrm{m}$ height, with the top region of each pixel ($50\,\mu\mathrm{m}\times25\,\mu\mathrm{m}$) dedicated to the in-pixel electronics and including pad for the bump-bonding connection required for the vertical integration.

Devices with different active areas are distributed in different columns of the array. In columns from 1 to 24 the active area is $43\times45\,\mu\mathrm{m}^2$, corresponding to a $51.6\,\%$ pixel fill factor. In columns from 25 to 27 the active area is $40\times40\,\mu\mathrm{m}^2$, in columns from 27 to 30 the active area is $35\times35\,\mu\mathrm{m}^2$ while in columns from 31 to 33 the active area is $30\times30\,\mu\mathrm{m}^2$.

The surface of most detectors (columns from 1 to 42) is covered with a metal layer in order to prevent inter-tier optical crosstalk while detec-

tors in the rest of the array (columns from 43 to 48) are left unshielded in order to perform optical measurements.

In Fig. 2.8 a micrograph of the chip is shown with shielded and unshielded pixel highlighted. In the close-up box, unshielded pixels with different active area can be seen.

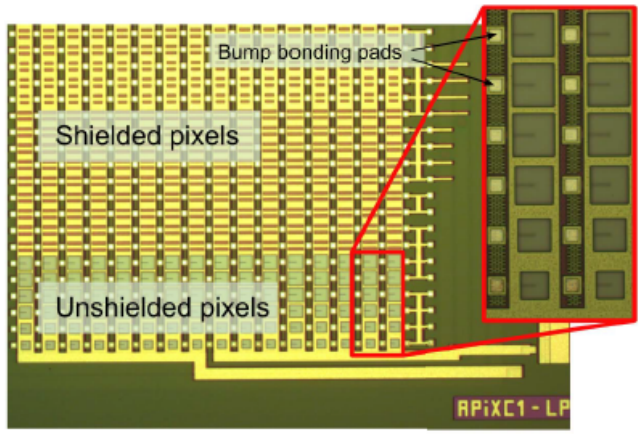

Figure 2.8: *Micrograph of the bottom chip [115].*

2.5.3 In-pixel Electronics

As mentioned in the previous subsection, the top area of each pixel is occupied by the in-pixel electronics, that is dedicated to the detector operation (biasing and signal extraction) and high level functionalities such as pixel selective enabling and coincidence detection.

In Fig. 2.9, a schematic block diagram of in-pixel electronics is reported for both top and bottom layers.

In-pixel electronics includes a passive quenching front-end, a comparator, a monostable for pulse shortening, an enable register, a coincidence detection circuit, a 1-bit memory and an output register.

The dead time (the time in which the detector is unable to detect an incoming particle) can be modified by the Vbn voltage applied at the gate of the quenching transistor M1.

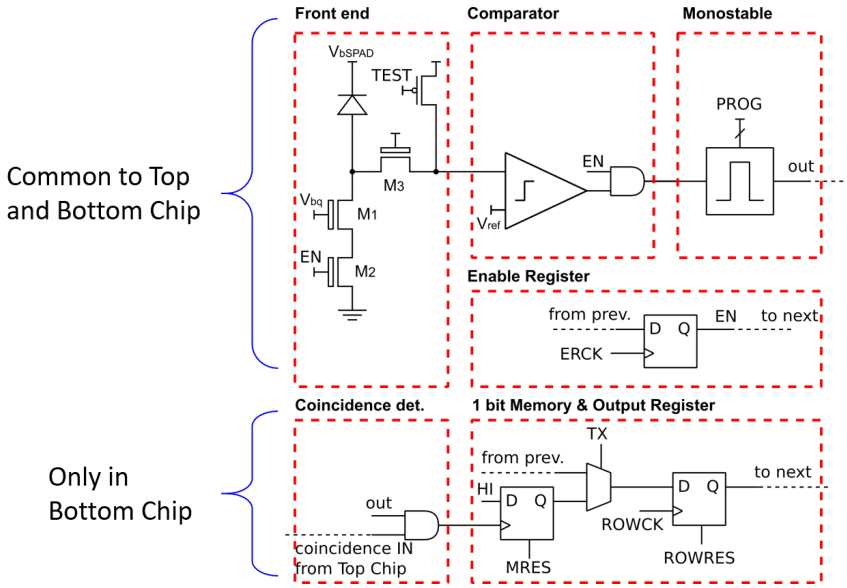

Figure 2.9: *Block diagram of in-pixel electronics.*

Transistor M2 has the function of selectively enable or disable the desired pixels in the array by means of an enabling pattern provided trough the enable register. This feature can be exploited to shut down noisy pixels, but was also used in the crosstalk characterization of the prototype, that will be reported in the next chapter.

In order to interface the comparator and digital electronics working at $1.8\,\mathrm{V}$ from the front-end electronics working at $3.3\,\mathrm{V}$ transistor M3 is used as a voltage clamp at $1.8\,\mathrm{V}$. The clamped voltage is then compared with a reference voltage (V_{ref}) to provide a digitized output signal to the next stages of the readout circuitry.

The output of the comparator enters an AND gate, that is transparent if the pixel is enabled through the enable signal (EN) and then feeds a programmable-length monostable. The width of the output pulse of the monostable can be set by means of a combination of two digital inputs.

By shortening the monostable output pulse width, it is possible to reduce the fake coincidence detection rate, generated by non particle-triggered spurious events related to the dark count noise of the two lay-

ers. In Fig.2.10 the effect of the reduction of coincidence time resolution is depicted comparing a long pulse width with a shorter one.

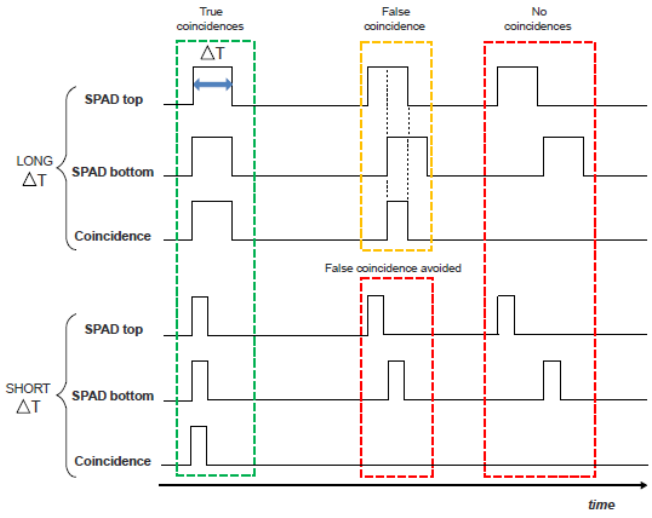

Figure 2.10: *Simplified timing diagram showing the effect of monostable pulse width on fake coincidence events [112].*

The core circuit of the device is the coincidence detection block that is integrated in the bottom pixel circuits, while the electronic blocks described so far are in common between both layer of the vertically-integrated device.

The coincidence detection is performed trough an AND gate connecting the outputs of the top-pixel monostable and the bottom-pixel monostable. The coincidence events are stored in 1-bit pixel memories, and the stored values are transmitted to the output through 8 output shift registers, each referring to two concatenated rows of the array in order to reduce the output pads. This configuration avoids any dead time in the data acquisition process since the data read out can be performed simultaneously with the signal detection.

The configuration register has the potential to increase the testability of the chip. In order to exploit this potential the monostable output is connected to a row-wise OR gate that combines the outputs of all the

active pixels in a row to a single signal stream. With a proper configuration, this read-out scheme allows the mapping of the DCR of each single layer chip.

In the bottom layer chip a row-wise coincidence detection circuit is also included to perform crosstalk measurements between arbitrarily-chosen pixels between two different rows. The output of the monostable is also connected to a row global OR, and the output of two different rows can be arbitrarily connected to a coincidence AND gate.

The coincidence detection performed at pixel level by using the embedded electronics was designed for a maximum frame rate of $100\,\mathrm{kHz}$ in global shutter mode. For a detection rate of up to a few kHz per pixel, the number of events lost due to the limited frame rate can be negligible. This rate is suitable for many applications requiring particle detection, from particle tracking in HEP experiments to radioactive source monitoring in biomedical applications.

2.6 Vertically-integrated Chip Architecture

Even though the bottom and the top chips have been designed to work as independent devices in order to fully characterize their performance, the ultimate goal of the research activity reported in this dissertation is the evaluation of the vertically integrated prototype.

The vertical-integration of the device was performed by connecting at pixel level the top and the bottom layers by means of SnAg solder bumps. This integration was executed at die level using the process available at IZM Fraunhofer, Berlin.

In Fig. 2.11 the concept view of the vertically-integrated sensor assembly is shown. After the vertical integration, the bottom layer chip was wire bonded to the package.

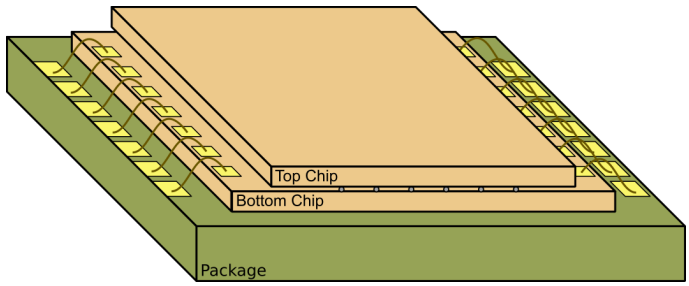

Figure 2.11: *Schematic representation of the vertically-integrated particle detector prototype[113].*

CHAPTER 3

Device Characterization

The characterization of CMOS detectors with embedded electronics calls for the design and the realization of a dedicated experimental setup to make the device operational and evaluate its functionality. The prototype requires an interface board to be connected to the instrumentation, to provide digital signals to control its functionality and acquire the outputs to test its performance. Moreover, environmental conditions such as temperature and illumination have to be kept constant during the characterization.

In this chapter the campaign of measurement to fully characterize the APiX particle detector is reported. The description starts with the presentation of the experimental setup with a detailed explanation of the firmware implemented to make the device operational. The results of the characterization are provided in terms of breakdown voltage, Dark Count Rate and optical crosstalk.

3.1 Setup

The APIX chip pair (Bottom and Top chips) was meant as a flexible platform to test the SPAD coincidence detection principle. The pair is composed by two chips: a master (Bottom Chip), which is larger and includes more functions, and a slave (Top Chip) to be flipped and bump bonded on the master. Both chips can be individually tested before bump bonding to ensure they are fully functional in advance. When bump-bonded, the master provides power supply, reference and digital signals to the slave.

A schematic representation of the experimental setup for the characterization of the device is reported in Fig. 3.1

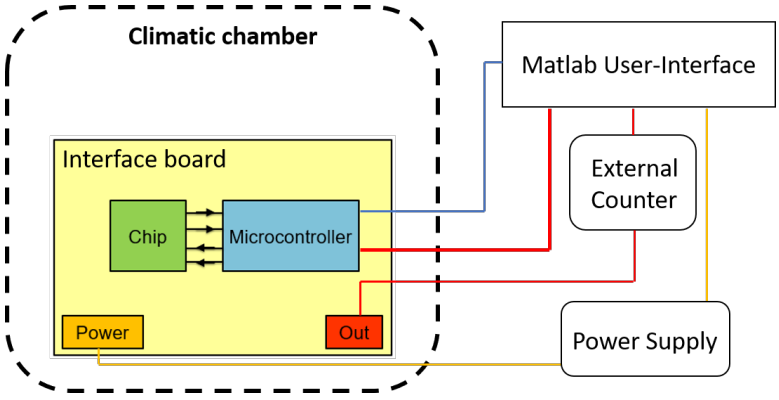

Figure 3.1: *Block diagram of the experimental setup with the interface board to connect the device to a microcontroller placed in a climatic chamber to stabilize the environmental condition. Orange connections refer to the programmable power supply, blue connections refer to the external user communication with the microcontroller and red connections refer to data output acquisition.*

The characterization setup is composed of an interface board to connect the device to a microcontroller, a programmable power supply to provide the voltage to the electronic circuitry and the bias for the avalanche diodes, a NI-DAQ board (National Instrument external counter having a maximum counting frequency of $50\,\mathrm{MHz}$) to extract the output counts and a PC to run the user interface software.

In both the chips, the comparators and the digital core are powered at

$1.8\,\mathrm{V}$, while the pads work at $3.3\,\mathrm{V}$. High voltage (15 to $30\,\mathrm{V}$) has to be used for SPAD biasing. The embedded digital electronics was designed to be compact, fast and with low power consumption: the core supply current at $1.8\,\mathrm{V}$ is in the order of $8\,\mathrm{mA}$ for the bottom chip device.

The microcontroller connected to the interface board (Atmel SAM3X8E running at $84\,\mathrm{MHz}$) was used to generate the digital signals required for the operation of the device and the extraction of the output signals. A PC user interface software was used to perform the desired measurements interacting with the microcontroller.

In order to stabilize the environmental condition, the interface board with the microcontroller were placed in a climatic chamber to ensure a constant temperature.

3.1.1 Interface Board

The function of the interface board is to hold the devices under test, provide the reference levels and bias voltages, and physically connect the device package pins to the I/O ports of the microcontroller.

Bottom chips and vertically-integrated devices were packaged in a standard PGA100 package while top chips were packaged in a standard JLCC44 package (Fig. 3.2).

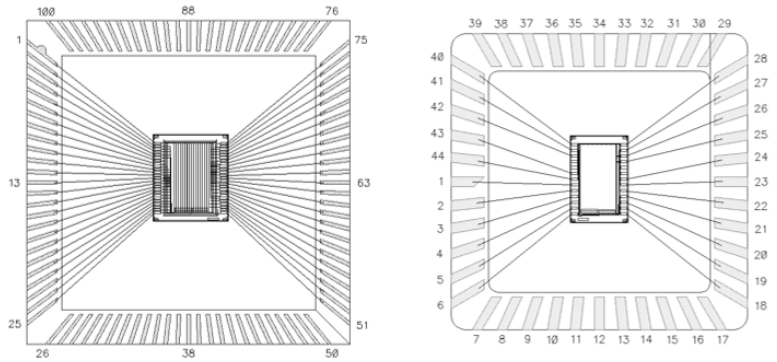

Figure 3.2: *(Left) PGA100 package for bottom chips and vertically-integrated devices. (Right) JLCC44 package for top chips.*

In order to easily replace the devices during the characterization

measurements, a fast plug-in/plug-out socket for the device package was inserted in the interface board.

The coincidence time is determined by the pulse width of the output of the programmable monostable described in section 2.5.3. This coincidence time can be set through a two-bit code (digital input signals M_S0 and M_S1) as shown in Table 3.1.

Table 3.1: *Coincidence time setting*

M_S0	M_S1	Time
0	0	SPAD dead time
0	1	1.5 ns
1	0	750 ps
1	1	10 ns

The voltage references for comparators, quenching transistors and clamping transistors are provided by a dedicated circuit integrated in the interface board. The voltage references can be manually-adjusted by the user to set the desired values. In the measurements, the reference voltage for the comparators, for the quenching and for the clamping transistors were set to $0.5\,\mathrm{V}$, $1.5\,\mathrm{V}$ and $2.5\,\mathrm{V}$, respectively.

The interface board incorporates also a set of connections to the programmable voltage supply for the SPAD biasing and the power supply for the electronic circuitry. Three different pins are available to connect the device outputs to the NI-DAQ external counter.

3.1.2 Microcontroller

The digital signals required to control the device and extract the output data were generated with a microcontroller.

Two different versions of firmware were developed according to the specific output of the device used for data extraction. The first version of the firmware, called Ext-Counter, was designed to be used together with an external counter to extract the counts from the OR output of the device. The second version, called Matrix-Generator, version was developed to extract the output from the in-pixel memory trough the

output shift register, designed with a First In First Out (FIFO) logic configuration.

Table 3.2: *List of digital input signals. B refers to Bottom chip while T refers to Top chip.*

Name	Idle state	Chip	Function
VSR2_CK	L	B	Vertical register 2 clock for row coincidence
VSR_RN	H	B & T	Vertical register reset
VSR_CK	L	B	Vertical register clock
TestN	H	B	Test input
FIFO_in	L	B	FIFO input for test only
FIFO_RN	H	B	FIFO reset
FIFO_SEL	H	B	FIFO select
FIFO_TX	L	B	FIFO transfer
mem_RN	H	B	Memory reset
EN_CK	L	B & T	Enable register clock
EN_RN	H	B & T	Enable register reset
EN_in	L	B	Enable register input
M_S0	L	B	Coincidence time setting bit 0
M_S1	H	B	Coincidence time setting bit 1
C2_VSR_CK	L	T	Vertical register clock for Top Chip
C2_TestN	H	T	Test input for Top Chip
C2_EN_in	L	T	Enable register input for Top Chip

In Table 3.2 the digital signals are reported with a brief description of their function.

The selection of the pixel in the array is performed through three vertical shift registers: two in the bottom chip and one in the top chip. The ”enable” configuration shift register requires a reset signal, a clock signal and two initialization signals, one for each layer of the device. Data readout trough the FIFO register from the internal memory is per-

formed with a reset signal, a FIFO selector, a data transfer signal, a memory reset and 8 different output signal referred to the 8 output pads of the device. Data readout is performed row-wise with the 16 rows concatenated in pairs, feeding the 8 output pads.

The first operation performed by the microcontroller after powering the sensor is the acquisition of the configuration parameters and the transmission of a feedback message. The configuration parameters are sent by the user interface software to set the ”enable” configuration register, the integration time and the acquisition modality. According to the measurements to perform, a desired pattern is loaded into the configuration register.

In Fig. 3.3 the timing diagram of the enable register loading signals is reported. During the loading of the configuration, the digital TESTN signals disable all the pixels of the array in each layer of the device. A sequence of clock pulses selects the position of each specific pixel, that is then enabled or disabled by the EN_IN signals.

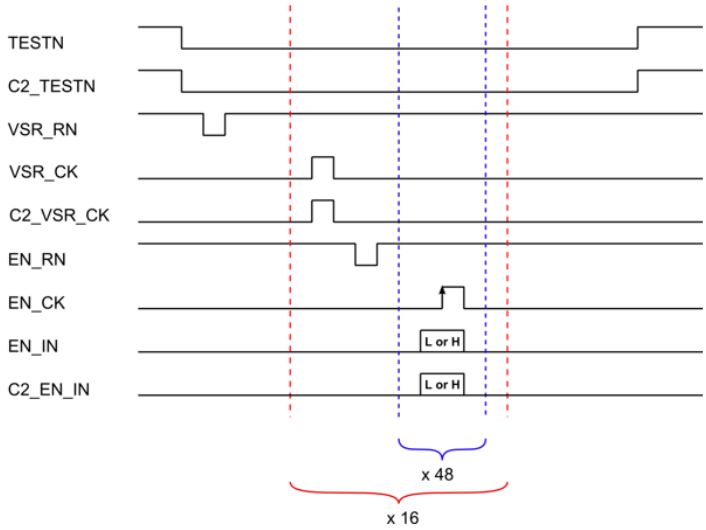

Figure 3.3: *Timing diagram of the enable register loading.*

Defined by the parameters row_min, row_max, col_min and col_max,

set by the user interface software, three different enable configuration patterns were designed to perform a variety of measurements:

- ROI (Region Of Interest) - A submatrix of pixels is enabled with the vertices defined by the (row_min-col_min) pixel and the (row_max-col_max) pixel.
- SPADs (two SPADs) - Only the (row_min-col_min) pixel and the (row_max-col_max) pixel are enabled.
- Rows (two rows enabled) - All the pixels of the row_min and row_max rows are enabled from col_min to col_max.

The enable configuration patterns described in the previous paragraph are reported in Fig. 3.4 to clarify their structures.

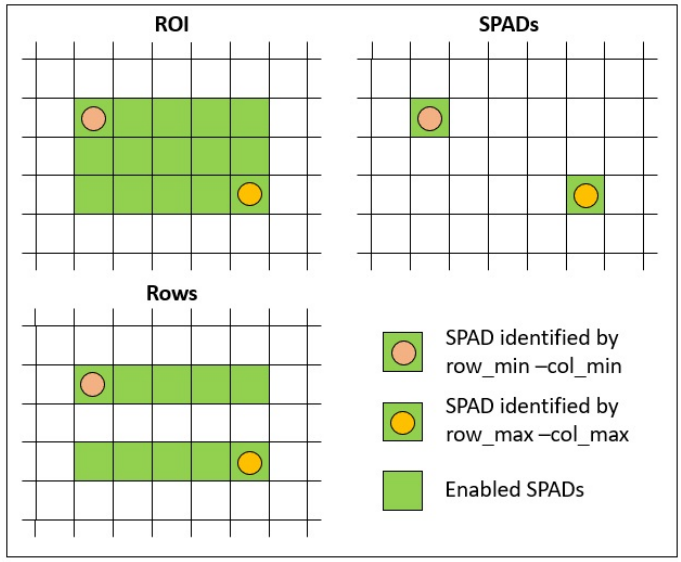

Figure 3.4: *Enable configuration patterns that can be selected after the identification of two SPADs trough the parameters row_min, row_max, col_min and col_max.*

After the configuration of the vertical registers, two different acquisition schemes can be performed depending on the runmode configuration parameter selected by the user. In the free-running mode, the output from the pixels enabled by the configuration pattern are acquired by

an external counter, while in the integration-mode the detection events are transferred from the internal memory to output FIFO registers to be directly acquired by the microcontroller.

In Fig. 3.5 the timing diagram of the data readout from the internal memory is reported. After a reset, the proper FIFO is selected, the data are transferred from the sensor to the microcontroller memory, and then transmitted to the PC under the control of the interface software.

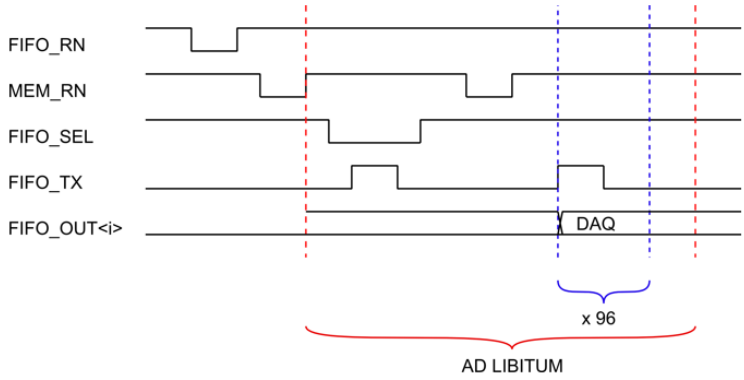

Figure 3.5: *Timing diagram of the data readout signals.*

3.2 Breakdown Voltage

The identification of the breakdown voltage is the first fundamental task to accomplish for a proper characterization of the device performance, since several characteristics such as dark count rate, optical crosstalk and afterpulsing depends on the excess voltage applied to the detector.

The extraction of the breakdown voltage is not a trivial procedure for detectors embedded with readout circuit and its uniformity has to be evaluated to select a mean voltage for the biasing of the whole array of detectors.

3.2.1 Extraction of the Breakdown Voltage

The acquisition of current-voltage curves is the standard procedure to identify the breakdown voltage in stand-alone devices. The integration of the detectors with the readout electronics makes the anodes unreachable while the cathodes are in common to all the detectors. Consequently, the measurement of the current-voltage curves is not possible and the breakdown voltage has to be extracted from DCR vs. bias voltage curves.

The DCR vs. bias voltage curves have been acquired by performing a voltage sweep with a voltage step of $25\,\mathrm{mV}$. The breakdown voltage has then been extracted through curve-fitting with a complementary error function of the data points.

In Fig. 3.6, an example of a fitted curve is reported. Since the voltage reference of the comparator is set to $500\,\mathrm{mV}$, this value has to be added to the the fitting parameter to determine the breakdown voltage.

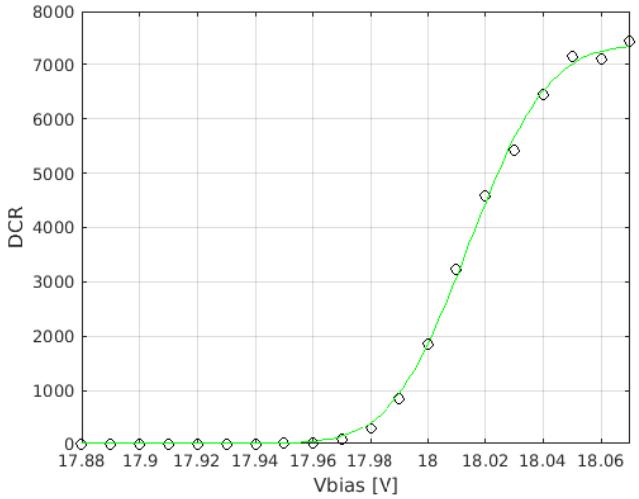

Figure 3.6: *Example of DCR vs. bias voltage curve. The symbols represent the data points, while the line is a fitting curve used for the extraction of the breakdown voltage.*

3.2.2 Breakdown Voltage Uniformity

The uniformity of the Breakdown voltage was evaluated by acquiring the DCR vs. bias voltage curves enabling a pixel at a time and scanning the whole array. Measurement results revealed an intra-array variability lower with respect to the variation between different chips.

In Fig. 3.7, the breakdown voltage distributions are reported on 5 different tested arrays. The uniformity among detectors of the same type is very good, with a standard deviation lower than $20\,\mathrm{mV}$ and a peak-to-peak variation in the order of $100\,\mathrm{mV}$.

The variation of the breakdown voltage between the same detectors on different chips is greater. Type 1 devices display a deviation of about $1\,\mathrm{V}$, while the range of variation for the Type 2 devices is lower, about $350\,\mathrm{mV}$.

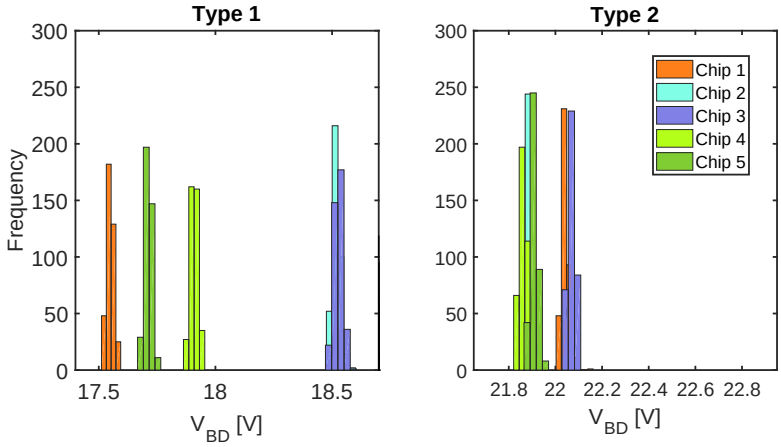

Figure 3.7: *Uniformity of the breakdown voltage measured on 5 dies.*

3.3 Dark Count Rate

Dark counts are avalanche events not triggered by an incoming particles or photons, but generated by internal noise. The generation mechanisms such as thermal generation and tunneling have been discussed in subsection 1.3.1. In this section, the evaluation of the DCR is reported and

the measurement configuration is described. DCR measurements were performed by placing the devices in a dark environment at a stable temperature.

The starting material, the fabrication process quality and the presence of contaminants affect the DCR distribution. In order to investigate the effects of local defects, a DCR map of all the pixels was acquired through a raster-scan of the whole array, enabling a pixel at a time for an acquisition time of 1s. The dark counts were acquired with the external counter.

In Fig. 3.8 the 2D map of the dark counts are reported for the Type 1 detector array. Since high DCR pixels are randomly distributed across the array, it can be concluded that the fabrication process did not introduce any gradients in the defects concentration. The 2D map for Type 2 detector array it is not shown since it features a similar behaviour.

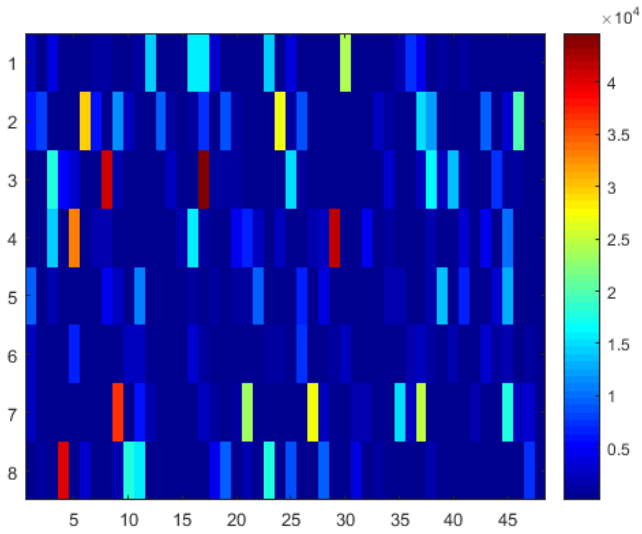

Figure 3.8: *2D map of the dark counts for Type 1 detectors at an excess voltage of 1V at 20°C.*

3.3.1 DCR Uniformity

The DCR uniformity within the pixel array was evaluated by acquiring the dark counts at different overvoltages. The DCR cumulative distributions of $43\,\mu\mathrm{m}\times45\,\mu\mathrm{m}$ detectors biased at $1\,\mathrm{V}$ and $3.3\,\mathrm{V}$ of overvoltage and measured on 5 different chips is reported in Fig. 3.9.

The DCR of devices of the same type spans several orders of magnitude, a typical behaviour that has been observed in different processes [116]. The uniformity of the DCR distribution between different chips is quite good. The median DCR is in the order of $3\,\mathrm{kHz}$ for both device types at $3.3\,\mathrm{V}$ excess bias, while the best detectors in the distribution exhibit a DCR in the order of $300\,\mathrm{Hz}$.

The best DCR corresponds to $0.15\,\mathrm{Hz}\,\mu\mathrm{m}^{-2}$ that is a rate comparable with commercial SiPM cells of the same size, while the median DCR is an order of magnitude larger than typical SiPMs ($1.5\,\mathrm{Hz}\,\mu\mathrm{m}^{-2}$). This higher DCR is a consequence of the standard CMOS process adopted for the fabrication of the devices that has no dedicated processing steps.

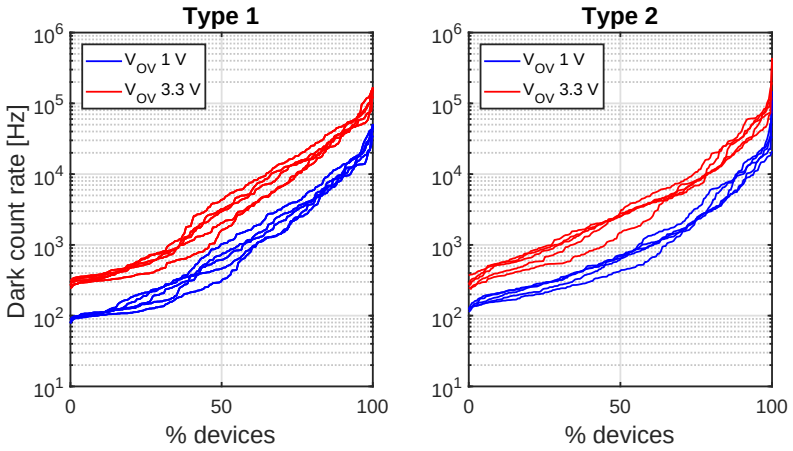

Figure 3.9: *DCR cumulative distributions of* $43\,\mu\mathrm{m}\times45\,\mu\mathrm{m}$ *detectors biased at* $1\,\mathrm{V}$ *and* $3.3\,\mathrm{V}$ *of overvoltage and measured on 5 different chips.*

3.3.2 Temperature Dependence

The effect of temperature on the DCR distributions was evaluated by measuring the dark counts at different temperature in the range from -30 °C to + 50 °C with 10 °C steps. As shown in Fig. 3.10, the experimental results are in good agreement with the theoretical expectation with a global reduction of dark counts as the temperature reduces [29]. While at high temperature SRH generation is the dominant mechanism responsible for the dark count rate, at low temperature its effect is widely reduced and the DCR is dominated by tunneling effect. The DCR distributions at lower temperature trends to overlap for the lower DCR detectors, since dark counts generated by tunneling have a very weak dependence on temperature variation.

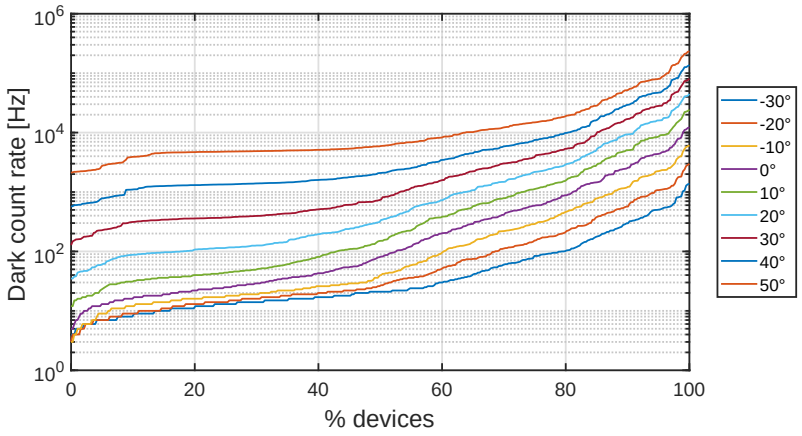

Figure 3.10: *DCR distributions for Type 1 detectors at an excess voltage of* 1 V *from* −30 °C *to* 50 °C.

In order to discuss the dominant physical mechanism responsible of DCR for the fabrication technology under analysis, the temperature dependence of three devices representative for the whole distribution is reported in Fig. 3.11. Although the devices have the same area, different activation energies can be inferred from the data.

An activation energy (E_A) smaller than $E_G/2$ indicates that trap-assisted tunnelling is the dominant mechanism for DCR generation in

devices with the largest DCR.

The detector with the lowest DCR in Fig. 3.11 exhibits two different slopes, thus two different generation mechanisms are dominant in different temperature ranges.

The low E_A observed at low temperature suggests that band-to-band tunnelling is probably the dominant mechanism. At high temperatures the activation energy is very close to the silicon band gap, hence the DCR is likely to be dominated by injection from the neutral regions.

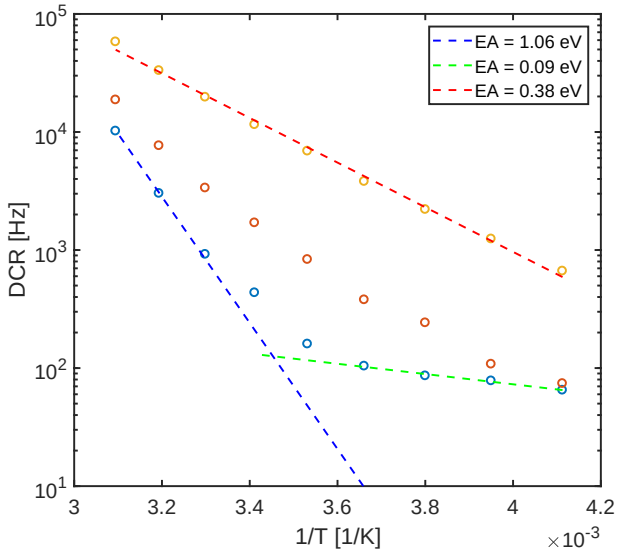

Figure 3.11: *Temperature dependence of dark count rate for three nominally equal detectors (Type 1,* $43\,\mu\text{m}\times45\,\mu\text{m}$*, Vex* $3.3\,\text{V}$*).*

3.4 Optical Crosstalk

The description of the physical generation mechanism of optical crosstalk and its effect in terms of performances of GM-APDs have been examined in the subsection 1.3.1, by discussing the theoretical and the experimental studies reported in literature.

The characterization of optical crosstalk in GM-APD arrays have often been performed through pseudo-crosstalk measurements [117, 118]. In this type of measurements, a pixel in the array is designed as the emitter of secondary photons while another pixel is defined as the detector. The crosstalk is extracted from the acquisition of the DCR of the detector in two different configuration. The first DCR is collected when the emitter of secondary photons is enabled while the second DCR is measured when the emitter is disabled. Crosstalk coefficient is then calculated by subtracting the second DCR from the first DCR. Since the increment of DCR related to the crosstalk can be very small, this measurement is performed several times to obtain an adequate statistics to evaluate the crosstalk with sufficient accuracy.

The coincidence detection electronics included in the APiX prototype represents a good opportunity to perform direct measurement of intra-tier crosstalk in single-layer devices and inter-layer crosstalk in vertically-integrated devices.

To perform a crosstalk characterization campaign, coincidence rate measurements were acquired between pairs of detectors while disabling all the other pixels in the array. To ensure a good acquisition rate, a pixel with high DCR was selected from a preliminary DCR mapping of the array to be used as the emitter of secondary photons. The coincidence rate was then acquired by enabling one-by-one the other detectors in the array.

To extract the coefficient of crosstalk from the measured coincidence rate, all the parameters involved should be considered both in the absence and in the presence of crosstalk. In the absence of crosstalk, the theoretical coincidence rate CR_t can be expressed as:

$$CR_t = 2\Delta T \times DCR_e \times DCR_d \tag{3.1}$$

where DCR_e and DCR_d are the dark count rates of the emitter and the detector, respectively. ΔT is the length of the monostable output that was set to 10 ns in the crosstalk characterization campaign of measurement. The factor 2 derives from the correlation of two pulses of the same length.

In the presence of crosstalk, the measured coincidence rate CR_m is

larger than CR_t, and can be expressed as:

$$CR_m = CR_t + K \times (DCR_e + DCR_d) \tag{3.2}$$

where K is a crosstalk coefficient. The value of crosstalk coefficient can be calculated replacing eq. 3.1 into eq. 3.2 and expliciting K.

$$K = \frac{CR_m - 2\Delta T \times DCR_e \times DCR_d}{DCR_e + DCR_d} \tag{3.3}$$

The intra-tier crosstalk was evaluated by measuring the CR_m with the external counter through the row-wise coincidence circuit, while the inter-layer crosstalk was evaluated in the vertically-integrated device by acquiring the coincidence counts using the internal memory.

In order to keep a constant temperature during the measurements, the interface board with the sensor and the microcontroller were placed in a climatic chamber at a constant temperature T=20°C.

3.4.1 Crosstalk dependence on excess voltage

In a first set of measurements, the effect of the excess voltage (i.e., bias voltage above breakdown) on the crosstalk coefficient was evaluated. The DCR of both emitter and detector was acquired with 1s integration time while the row-wise coincidence rate was acquired with $100\,\mathrm{s}$ integration time to minimize the relative measurement error. A voltage sweep was performed to modify the excess voltage from $0.5\,\mathrm{V}$ to $3.25\,\mathrm{V}$ with a $250\,\mathrm{mV}$ voltage step.

The results of this measurements are summarized in Fig. 3.12 where a comparison between Type 1 and Type 2 devices is shown. Both types of devices show the same qualitative behaviour, with Type 2 devices showing higher values of crosstalk coefficient.

In order to explain the observed behaviour we have to consider the dependence of crosstalk probability on both photon emission and detection probability.

During an avalanche event, the number of carriers generated in the emitter is proportional to the applied excess voltage. The trigger probability in detectors depends linearly on the excess voltage at low voltages while it reaches a saturation level at higher voltages. The combination

of these two processes leads to a quadratic dependence of the crosstalk coefficient at lower voltages, while at higher voltages a linear trend follows. This bi-folded nature is highlighted by data fitting reported in Fig. 3.12, quadratic at low voltages and linear at higher voltages.

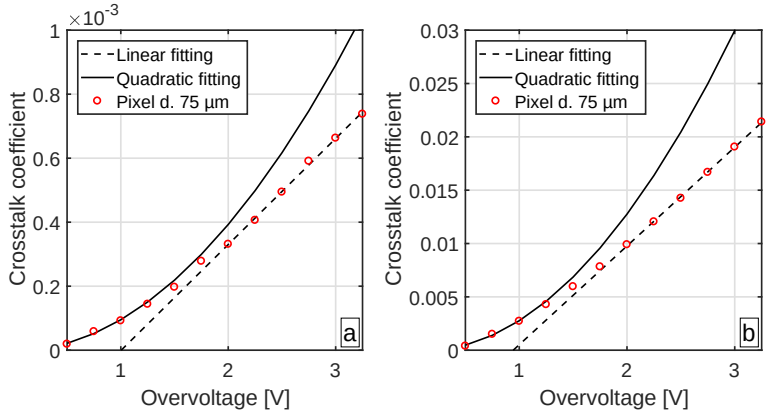

Figure 3.12: *Crosstalk coefficient as a function of the overvoltage. (a) Type 1 devices (b) Type 2 devices. Linear and quadratic fitting lines are also shown. The maximum measurement error is* 1.4×10^{-5} *for Type 1 devices and* 1.1×10^{-4} *for Type 2 devices.*

3.4.2 Dependence on substrate thickness

As discussed in the subsection 2.5.1, the presence of an isolation layer (n-iso) that isolates the devices from the p-substrate allows in principle the chip to be thinned down to few microns without compromising its functionality. This reduction of the substrate thickness features an opportunity to enhance the performance of the particle tracker since the particle is less perturbed by the reduced substrate.

In order to test the feasibility of the thinning procedure, the original $280\,\mu\text{m}$ substrate thickness of some dies was reduced to $50\,\mu\text{m}$ and $25\,\mu\text{m}$. The thinning process was performed in two consecutive steps: a grinding process, to remove the substrate to a desired depth, and a polishing step, to relieve the stress produced by the back grinding step. Since this process was performed starting from diced sensors, the sur-

face was covered with a protective wax to hold the samples and avoid damages during the grinding step. The functionality of thinned devices was tested by performing a set of DCR measurements that revealed that the grinding process did not damaged the devices.

In this section, the role of the substrate thickness in the crosstalk process is reported. A set of measurements was performed to calculate the crosstalk coefficient as a function of the distance between emitter and detectors.

This set of measurements was executed on dies with three different thicknesses: $280\,\mu m$, $50\,\mu m$ and $25\,\mu m$. Both Type 1 and 2 detectors were analysed by measuring two 8×24 pixel sub-arrays with uniform size. The avalanche detectors in the sub-arrays have a maximum active area of $43\times45\,\mu m^2$. A high DCR pixel at the border of the array was employed as an emitter of secondary photons while the rest of the array was enabled a pixel at a time. After the acquisition of the DCR of emitter and detectors, and of the coincidence rates CR_m, the coefficient of crosstalk K was calculated using eqn. 3.3. In Fig. 3.13 a map of the crosstalk coefficient is reported for a die with $25\,\mu m$ tickness at $3\,V$ of excess voltage.

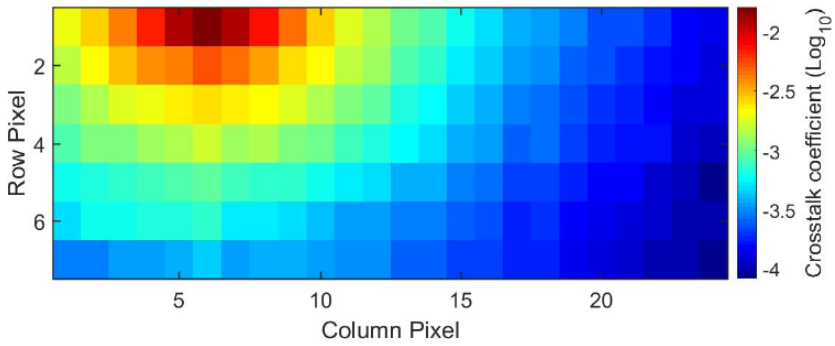

Figure 3.13: *Crosstalk coefficient 2D map measured on a die with* $25\,\mu m$ *tickness at Vex* = $3\,V$ *(Type 1 detectors) [119].*

Fig. 3.14, Fig. 3.15 and Fig. 3.16 show the crosstalk coefficient as a function of the distance between detector and emitter for both types of detectors respectively for the $280\,\mu m$, $50\,\mu m$ and $25\,\mu m$ thick devices.

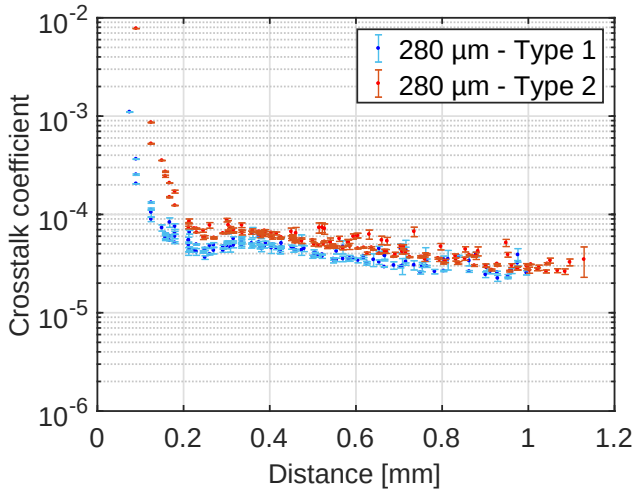

Figure 3.14: *Crosstalk coefficient as a function of detector distance for a die with* $280\,\mu\mathrm{m}$ *substrate thickness.*

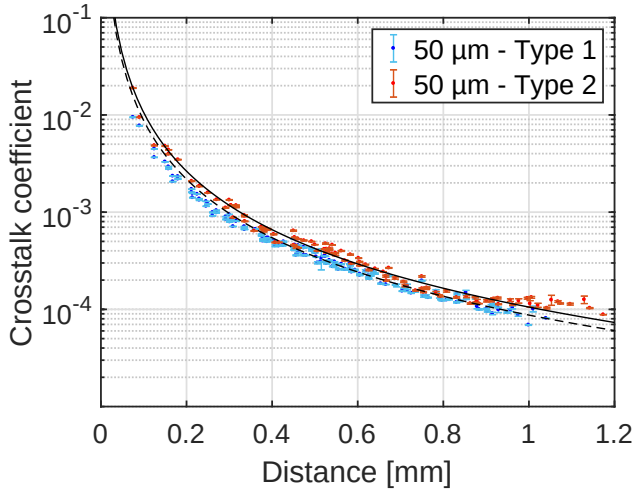

Figure 3.15: *Crosstalk coefficient as a function of detector distance for a die with* $50\,\mu\mathrm{m}$*substrate thickness. Dashed and continuous black lines are* $A\frac{1}{r}e^{-\alpha r}$ *fitting curves for Type 1 and Type 2 devices, respectively.*

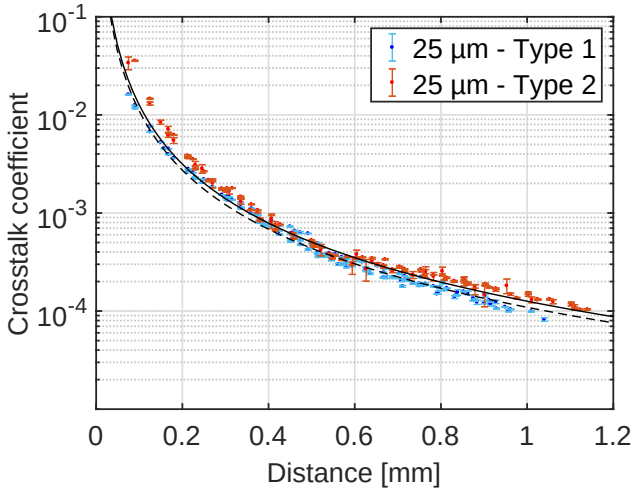

Figure 3.16: *Crosstalk coefficient as a function of detector distance for a die with* $25\,\mu\mathrm{m}$ *substrate thickness. Dashed and continuous black lines are* $A\frac{1}{r}e^{-\alpha r}$ *fitting curves for Type 1 and Type 2 devices, respectively.*

The crosstalk coefficient decreases with the distance from emitter and detector since, as the distance increases, the probability that emitted photons are absorbed outside the active region is higher. At low distances the decrease is very rapid, while at higher distances the decrease is less pronounced. The crosstalk coefficient decreases monotonically for thinner samples, while the $280\,\mu\mathrm{m}$ thick devices display a secondary peak at a distance of about $350\,\mu\mathrm{m}$ for both device types.

This secondary peak can be explained considering the combined presence of direct and indirect crosstalk. As observed by Rech et al. [118], total internal reflection at the bottom of the substrate can produce a peak in the crosstalk at distances corresponding to the transition from partial to total internal reflection. Thinner samples do not exhibit the secondary peak, since the distance between neighboring pixels is in the order of or even larger than the thickness of the substrate, and the substrate behaves as a 2D wave guide for secondary photons. Due to the waveguide effect, K is expected to be proportional to $A\frac{1}{r}e^{-\alpha r}$, where r is the distance between the emitter and the detector, α is the silicon absorption

coefficient and A is a fitting parameter. This model has been used to interpolate the experimental data in Fig. 3.15 and Fig. 3.16.

3.4.3 Detectors Comparison

Differences in the structures between the two types of detectors lead to different values of crosstalk coefficient. Type 2 devices exhibit higher value of crosstalk coefficient compared to Type 1 detector independently from the thickness of the substrate. This higher value is a consequence of the higher active volume and higher depth of the junction for Type 2 detectors.

Considering the ratio between crosstalk coefficients for Type 2 devices over Type 1 at a distance where the direct crosstalk can be considered negligible, the value is 1.36 ± 0.13, close to the ratio between the junction active thicknesses of the two devices (~ 1 μm for Type 1 and ~ 1.5 μm for Type 2). This higher active volume features a lower capacitance for Type 2 detectors, thus, a lower number of carriers are generated during the avalanche at the same excess voltage if compared to Type 1 detectors [29]. Consequently, the probability of emission of secondary photons is decreased, an effect that is in disagreement with the higher crosstalk for Type 2 detectors compared to Type 1. This discrepancy can be explained by considering the different PDE of NIR photons for the two types of detectors. The higher PDE for Type 2 detectors overcompensates their lower capacitance leading to a higher crosstalk coefficient; however, the crosstalk coefficient ratio is lower with respect to the PDE ratio thanks to the lower capacitance of the Type 2 detectors.

At short distances the ratio of the crosstalk coefficients is greater than 2, implying that the difference in the active volume between the two types of detectors is not the only factor to be taken into account. It should also be taken into account that at closer distances the direct crosstalk can be contemplated as the dominant component. The higher ratio of crosstalk coefficient can thus be linked to the larger depth of the the p-n junction for Type 2 devices. With a deeper junction, the effectiveness of Shallow Trench Isolation (STI) in shielding secondary photons following a direct path is smaller, and thus the crosstalk effect

is higher.

3.4.4 Overall effect of Crosstalk

The crosstalk measurements reported so far were acquired by enabling a pair of pixels at a time. This configuration was useful to extract information about the crosstalk coefficient behaviour, but does not correspond to the operating condition of the device in which the entire array is enabled. In this section the global effect of crosstalk observed when the whole array is enabled is reported and discussed.

For this type of measurement the DCR can only be extracted from the in-pixel memory that stores the pixel counts independently. The in-pixel memory was also used to acquire the DCR distribution with one active pixel at a time for comparison.

In Fig. 3.17 the cumulative DCR distributions for Type 1 detectors with (a) $280\,\mu\mathrm{m}$, (b) $50\,\mu\mathrm{m}$, and (c) $25\,\mu\mathrm{m}$ thickness are reported. The DCR distributions measured when enabling a pixel at a time are depicted in light blue, while the distributions measured when the whole array is enabled are depicted in orange.

It is worth mentioning that the variability between the light blue curves of different devices is not related to their substrate thicknesses. As widely discussed in section 2.5.1, the presence of a n-iso layer between the active region and the substrate makes the DCR independent from the substrate thickness. Therefore, the cause of the differences in the DCR distributions has to be ascribed to the fabrication process. The DCR depends mainly on the defects present in the active region, and devices fabricated on different wafers or even different positions of the same wafer may exhibit a slightly different DCR distribution.

Although the graphs are related to different dies having different DCR distributions (light blue curves), the increase in the average crosstalk with decreasing thickness is clearly visible. The global effect of crosstalk is to increase the DCR of a factor of 2, 6 and 8 shifting from the thickest to the thinner substrate.

As depicted in Fig. 3.18, the crosstalk dependence on the substrate thickness for the Type 2 detectors is in qualitative agreement with the one observed for Type 1 devices. The higher magnitude of crosstalk

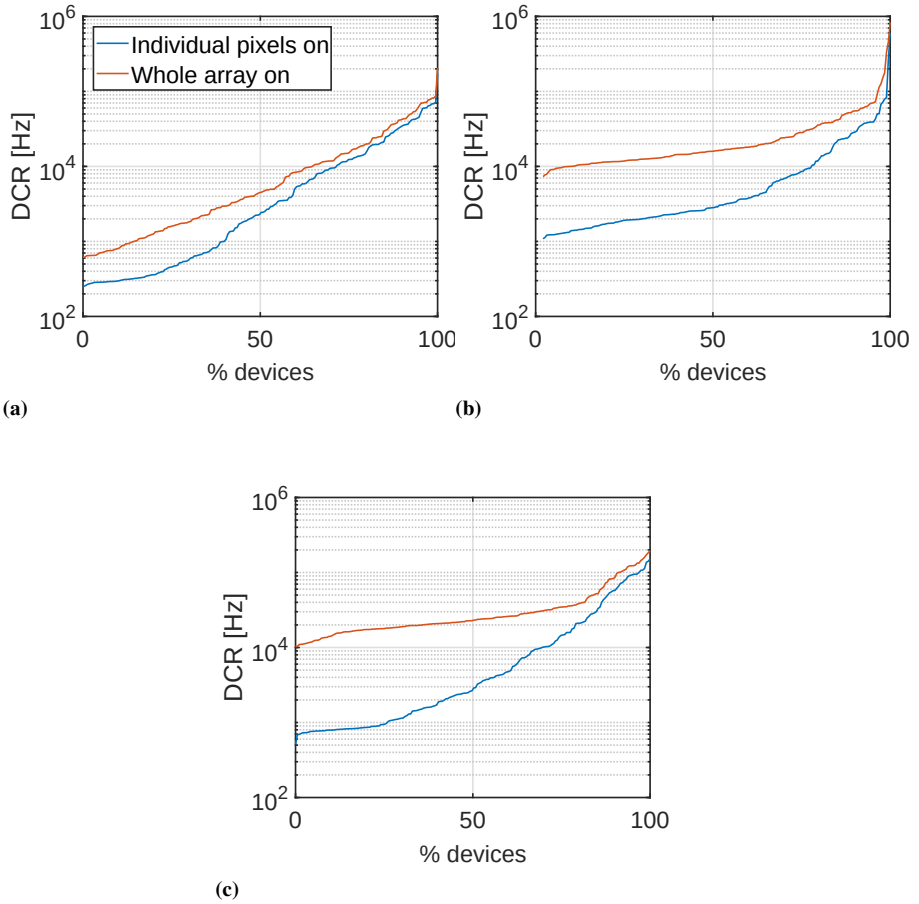

Figure 3.17: *DCR distributions acquired at* $3\,\mathrm{V}$ *of excess voltage by switching on one individual pixel at a time and by simultaneously enabling all the pixels in the array. Type 1 devices: (a)* $280\,\mu\mathrm{m}$ *thickness, (b)* $50\,\mu\mathrm{m}$ *thickness, and (c)* $25\,\mu\mathrm{m}$ *thickness.*

coefficient for the Type 2 detectors is a consequence of the larger active volume and deeper junction as discussed in the previous section 3.4.3. The median DCR observed when all the pixels are enabled is 3 times the DCR obtained when enabling a pixel at a time for the $280\,\mu\mathrm{m}$ device, 24 times for the $50\,\mu\mathrm{m}$ device, and 59 times for the $25\,\mu\mathrm{m}$ device.

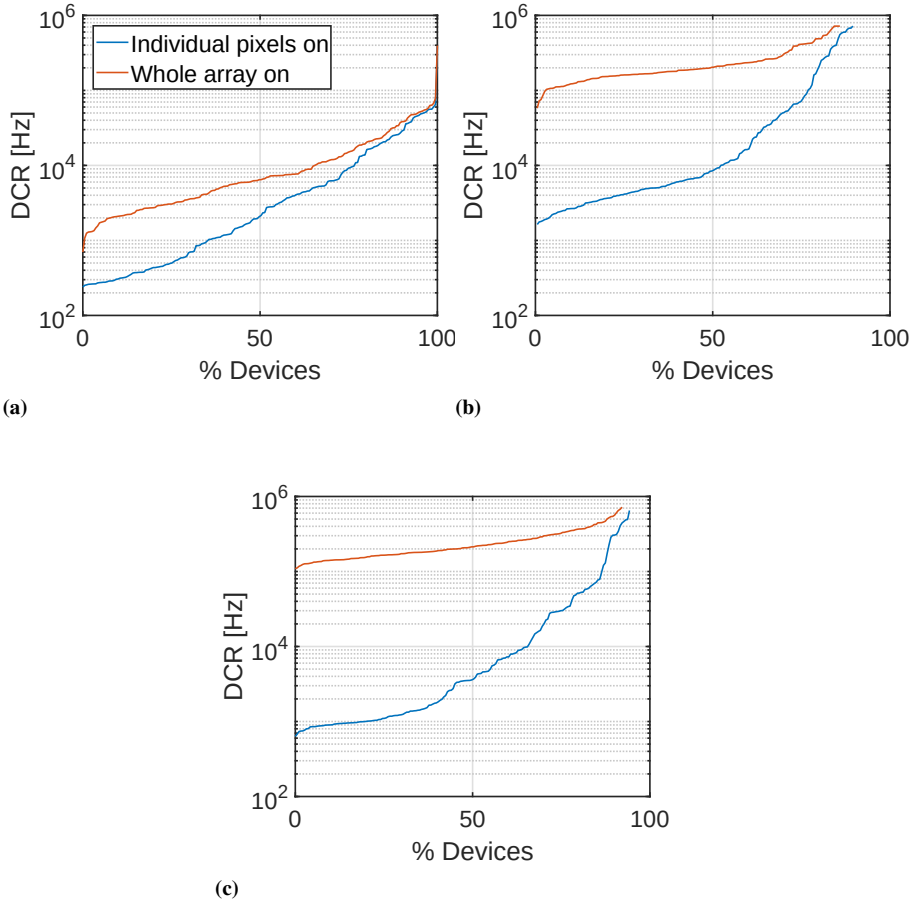

Figure 3.18: *DCR distributions acquired at* $3\,\mathrm{V}$ *of excess voltage by switching on one individual pixel at a time and by simultaneously enabling all the pixels in the array. Type 2 devices: (a)* $280\,\mu\mathrm{m}$ *thickness, (b)* $50\,\mu\mathrm{m}$ *thickness, and (c)* $25\,\mu\mathrm{m}$ *thickness.*

While for the $280\,\mu\mathrm{m}$ thick devices of both types the increase is similar, when lowering the thickness of the substrate, Type 2 devices exhibit a much larger effect than Type 1 devices, that is up to 7 times larger for the thinnest dies. This enhanced effect can be attributed to the combination of the waveguide effect when lowering the substrate and the larger

active area of Type 2 detectors.

In order to provide the same operating condition to compare different types of detectors and devices with different substrate thickness, the measurement reported so far were acquired with the same excess voltage of $3\,\mathrm{V}$. The effect of excess voltage on the overall crosstalk was investigated and the results for a Type 2 die with a thickness of $50\,\mu\mathrm{m}$ are reported in Fig. 3.19 , where an excess voltage of $1\,\mathrm{V}$, $2\,\mathrm{V}$ and $3\,\mathrm{V}$ was respectively applied. As a consequence of the increase of the gain, as the excess voltage increments the crosstalk effect gets more significant. As a term of comparison we can consider the variation on the median DCR when the whole array is enabled, that increases up from $16\,\mathrm{kHz}$ at $1\,\mathrm{V}$ to $188\,\mathrm{kHz}$ at $3\,\mathrm{V}$. This overall effect of crosstalk is a critical aspect that can leads to a severe reduction of the operating excess voltage of the device. A trade-off between the DCR and the detection probability has to be made when considering the operating excess voltage.

3.4.5 Inter-Layer crosstalk

The crosstalk measurements described in the previous subsections analyse the increase of dark counts caused by secondary photons generated and propagating within the substrate of the device. In this subsection the vertically integrated prototype was employed to evaluate the vertical crosstalk between pairs of pixels of the two layers. In this configuration, a secondary photon can trigger an avalanche not only in another pixel of the same layer, but also in the other layer of the device.

The evaluation of crosstalk between different tiers is a useful investigation with an increasing importance now that 3D-integrated SPAD imaging devices are being demonstrated [89, 65]. The photon emission in a stacked CMOS Image Sensor (CIS) device may leads to a reduction of the image quality. In this type of device the photons are emitted by the electronics of the ASIC layer and are detected in the top pixel array [120].

Three different pairs of vertically aligned unshielded pixels for each type of detectors have been selected to evaluate the vertical crosstalk. The DCR of each device was acquired together with the coincidence rate between the detectors in the two layers, and the result was used

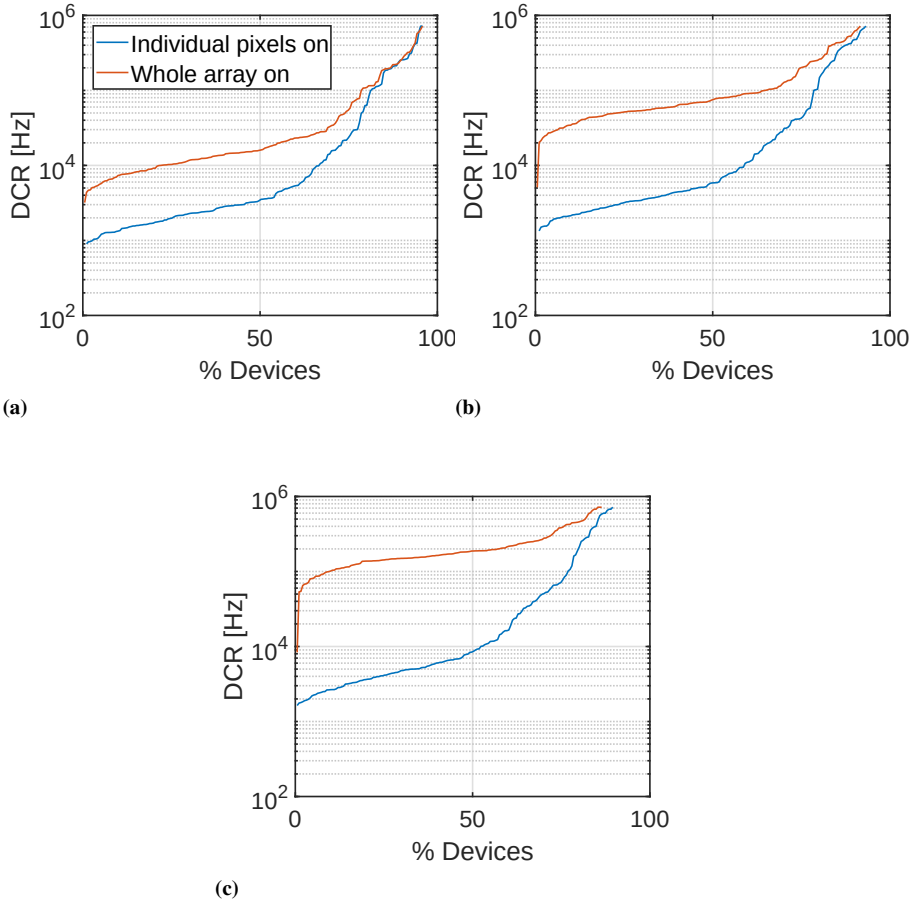

Figure 3.19: *DCR distributions acquired by switching on one individual pixel at a time and by simultaneously enabling all the pixels in the array. Type 2 devices with* $50\,\mu\mathrm{m}$ *thickness biased at three different excess voltages: (a)* V_{EX}=$1\,\mathrm{V}$*, (b)* V_{EX}=$2\,\mathrm{V}$*, and (c)* V_{EX}=$3\,\mathrm{V}$.

to calculate the crosstalk coefficient. The DCR of each layer was measured with the external counter setting an acquisition time of $10\,\mathrm{s}$, while the coincidence rate was acquired with the internal memory, setting an acquisition time of $100\,\mathrm{s}$. In order to evaluate the variability, 10 measurements for each voltage step were acquired.

Fig. 3.20 shows the inter-layer crosstalk coefficient as a function of excess voltage. Type 2 detectors show a higher crosstalk coefficient with respect to Type 1 detectors. At lower voltages, the difference of crosstalk coefficient between the two types of detectors is larger than the difference at higher voltages.

This behaviour can be explained considering the different photon detection efficiencies of the two types of detectors. The efficiency of Type 2 detectors for infrared photons is larger than for Type 1 detectors, and the avalanche triggering probability increases more sharply with overvoltage for Type 2 detectors than for Type 1 [121].

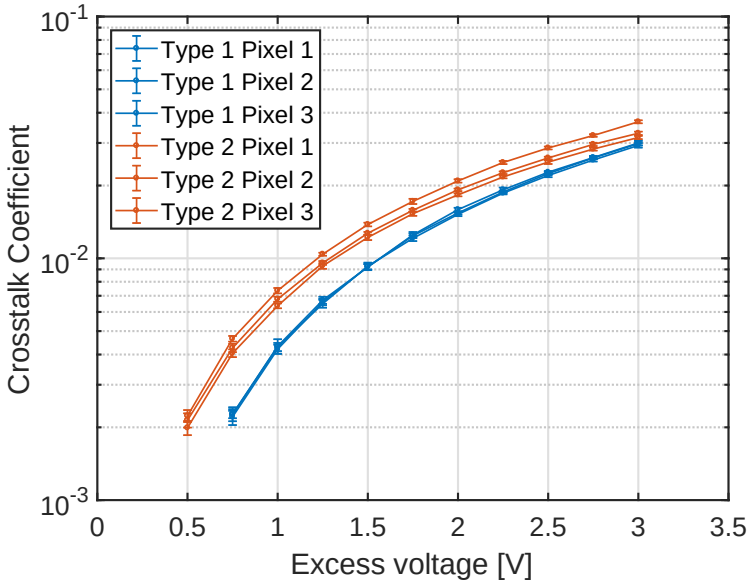

Figure 3.20: *Crosstalk coefficient as a function of the excess voltage for three different pairs of pixels of each type of detectors measured on the vertically integrated prototype.*

CHAPTER 4

Characterization with radiation sources

In this chapter the functional characterization of the APiX prototype with a β-source is reported and an evaluation of the radiation hardness of the devices is discussed.

To the best of the author's knowledge, the evaluation of the radiation damage in devices based on SPADs fabricated in commercial CMOS technology has been reported only in few works available in literature. In these works, different types of radiation sources are employed and the effect of ionizing particles is not clearly distinguished from non-ionizing particles[122, 123, 124, 125].

A radiation damage study that is complementary with respect to the analysis described in this dissertation has been conducted in the framework of the APiX projects. This study reports on the effects of ionizing and not ionizing radiation on SPADs designed in a $180\,\mathrm{nm}$ CMOS process[126].

In section 4.1, the experimental validation of the vertically-integrated APiX prototype using a β source is reported, in section 4.2 a neutron irradiation campaign is reported with a discussion on the dependence of the radiation induced DCR increase as a function of the neutron fluence. In section 4.3, an on-line measurement of a proton flux is reported.

4.1 Experimetal characterization with a β source

In order to demonstrate the particle detection ability of the APiX prototype, a set of measurement with a ^{90}Sr β source was performed.

The radioactive source employed in this work is a SIR1211 Eckert & Ziegler planchet source with an active diameter of $16\,\mathrm{mm}$, corresponding to an area of $2\,\mathrm{cm}^2$ and an activity of $39\,\mathrm{kBq}\pm6\,\%$. The source was kept at a distance of $5\,\mathrm{mm}$ from the detector surface by positioning it on a plexiglass holder placed on top of the detector package. The plexiglass holder fulfilled the double function of source holder and protection for the wire bonding connecting the detector to its package PCB.

4.1.1 Preliminary Evaluation

The optimal operative conditions for the acquisition of β-events was evaluated in a set of preliminary measurement aiming to select the pulse width of the monostable output and the operative excess bias. A submatrix of the pixelated array composed of 8×24 detectors with the same active area of $43\times45\,\mu\mathrm{m}^2$ was used in order to ensure uniformity of detection.

In Fig. 4.1, the coincidence DCR distribution of the 8×24 submatrix for Type 1 detectors is reported together with the DCR of each single layer. As described in chapter 3, Type 1 detectors exhibit a lower crosstalk coefficient with respect to the Type 2 detectors. Consequently, the validation β-event detection measurements were performed on the Type 1 detectors.

In order to better clarify the effect of the monostable output pulse width on the coincidence Dark Count Rate (DCR_c), the theoretical dependence of DRCc on the coincidence time resolution ΔT, already discussed in Chapter 2 is reported again here:

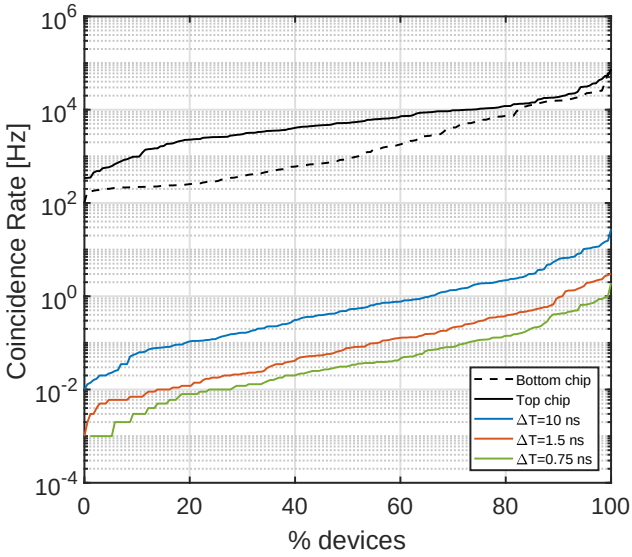

Figure 4.1: *Distribution of the Dark Count Rate in coincidence with the three different selectable values of time resolution ΔT. Measurement performed on Type 1 detectors at $V_{EX} = 1V$ and T =20 °C).*

$$DCR_c = DCR_{top} \times DCR_{bottom} \times 2\Delta T \tag{4.1}$$

Shrinking the monostable output pulse width, the mean DCR_c is effectively reduced down to $93\,\mathrm{mHz}$ corresponding to $24\,\mathrm{Hz\,mm^{-2}}$ in the best case of $0.75\,\mathrm{ns}$ time resolution. In table 4.1, the mean and median DCR_c for the three different values of time resolution for the Type 1 detector is reported.

4.1.2 Particle Detection Rate Simulation

Monte Carlo (MC) simulations were performed to quantify the expected events to be detected in the experimental condition previously described.

In Fig. 4.2, the energy distribution of the simulated β particles is reported, highlighting the reduction of the fraction of particles entering the bottom chip with respect to the amount of particles entering the

Table 4.1: *Mean ad median DCR at different values of time resolution*

	Mean DCR	Median DCR	
Top chip	6.7	1.3	kHz
Bottom chip	7.9	4.2	kHz
ΔT = 10ns	1426	337	mHz
ΔT = 1.5ns	268	64	mHz
ΔT = 0.75ns	93	24	mHz

surface of the detectors. This reduction is due both to the acceptance of the detector and the absorption of low energy particles in the bulk of the top chip.

Together with the geometrical fill factor of about $51.6\,\%$, the acceptance of the detector is one of the main limiting factors in the β-measurement here reported, considering the wide extension of the radioactive source with respect to the small size of the detector.

The bulk of the top chip defines the entrance window of the detector, in which the low-energy particles emitted by the β radioactive source can be absorbed within its $280\,\mu\mathrm{m}$ thickness before reaching the active layer. Only $40\,\%$ of the β particles entering the top chip surface are able to reach the active layer: this reduction is highlighted in Fig.4.2 with the red arrows.

The angle of incidence constitutes another source of inefficiency, since particles hitting the sensor with a non-orthogonal angle might generate a signal only in one of the two layers. Particles incident at large angles are more likely to fail hitting both layers.

Taking into account all the parameters considered in the simulations an expected rate of $7.3\,\mathrm{Hz\,mm^{-2}}$ is predicted. Thus, to be able to resolve such rate with a good contrast, a further reduction of the DCR_c is required to perform the measurement.

In Fig. 4.3, the coincidence DCR distribution is shown as a function of the applied excess bias. An excess voltage of $1\,\mathrm{V}$ was selected in order to limit the DCR_c, thus accepting the disadvantage of working with a triggering probability that was far from its saturation value. In the MC simulations the generation of charges induced by the energy

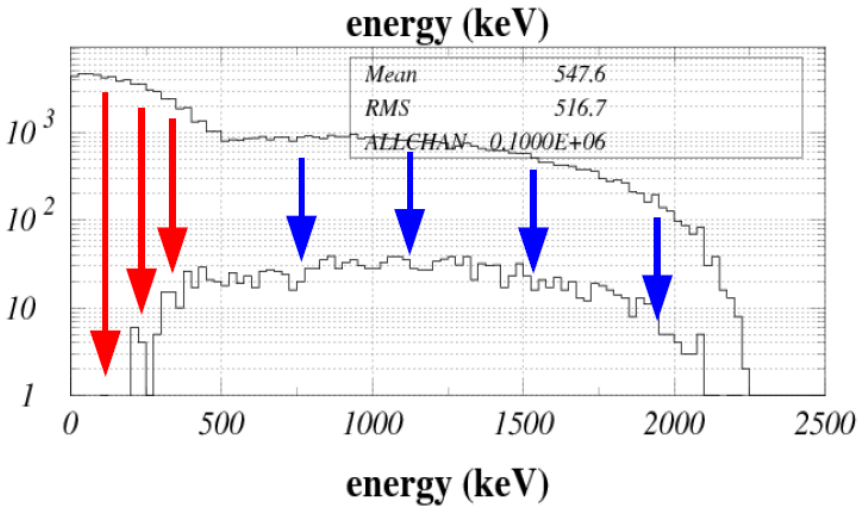

Figure 4.2: *Energy distributions of the simulated β particles (generated & entering the active region of bottom the chip). Blue arrows refer to reduction due to the acceptance, while red arrows refer to the absorption in the bulk of the top chip.*

release of beta particles crossing the active volume of the sensor has been predicted. Notwithstanding the granularity of charge release in the very thin active region of the sensor (less than $1\,\mu\mathrm{m}$), in more than $99\,\%$ of the cases, at least 1 electron is released in the active volume, while at least 5 electrons are generated in $97.5\,\%$ of cases.

The triggering probability of an electron-hole pair generated by a charged particle can be estimated from the optically-measured probability using NIR radiation, that in the case of multiple photon absorption is predicted by the equation:

$$P_{tN} = 1 - (1 - P_{t1})^N \tag{4.2}$$

With P_{t1} the triggering probability of a single photon absorption and P_{tN} the probability related to N-photons absorbed. Since in most of the cases more than 1 electron-hole pair is generated by the beta particle crossing, it is reasonable to assume that even if P_t at $1\,\mathrm{V}$ excess voltage is low the combined probability of multiple pairs generation predicted with eq. 4.2 can be close to $100\,\%$.

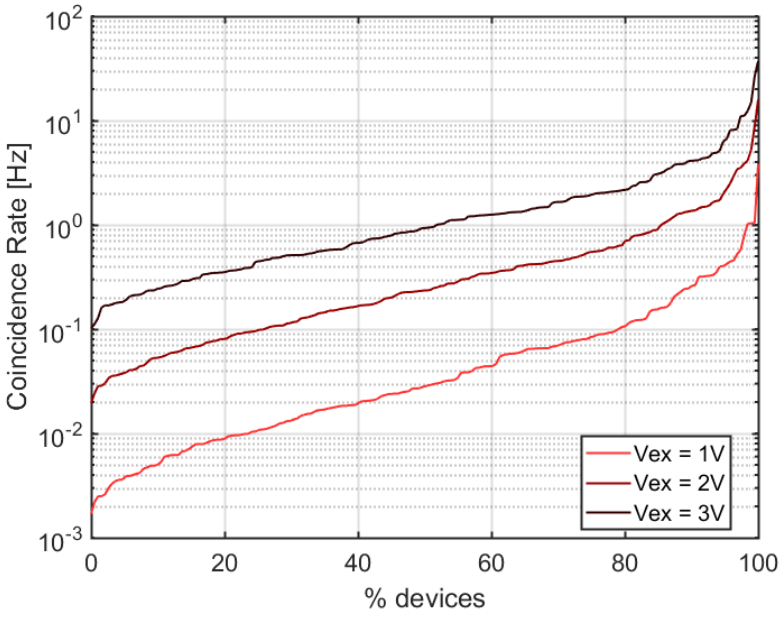

Figure 4.3: *Distribution of DCR in coincidence at different excess voltages. (Measurement performed on Type 1 detectors at* T =20 °C *and* ΔT =0.75 ns.*)*

To further decrease the DCR_c, the temperature at which the measurement is performed can be reduced. In Fig. 4.4 the coincidence DCR distribution is shown as a function of temperature. Since both the DCR of each layer of the vertically-integrated detector depends on temperature, its effect on the DCR in coincidence is enhanced.

By cooling the device down to 5 °C, the DCR_c is reduced down to $4.6\,\mathrm{Hz\,mm^{-2}}$ a value that is in the order of the particle rate expected in the radioactive source measurement, thus making the device to be able to detect the β particles with a good Signal-to-Noise ratio.

4.1.3 Experimental characterization

The experimental characterization with β-particles was performed by acquiring a large number of frames with 1 ms integration time using the in-pixel memory. The frames were summed to obtain a total accumu-

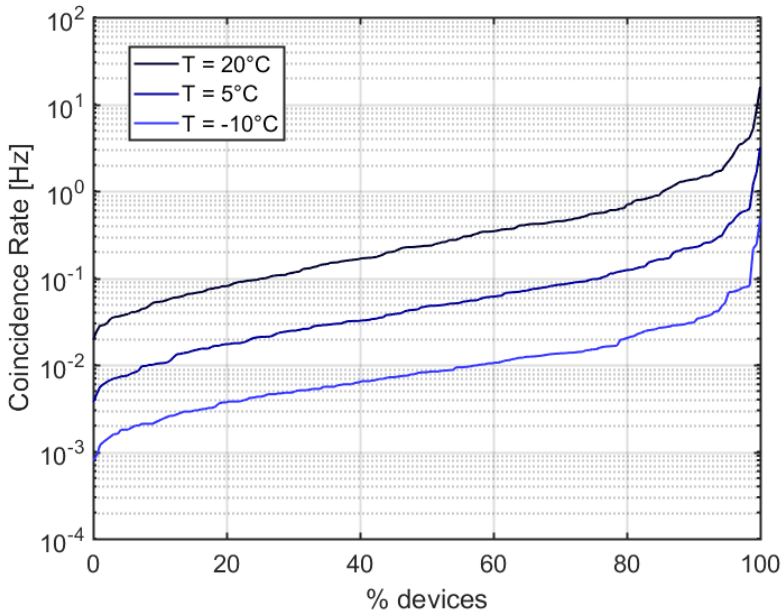

Figure 4.4: *Distribution of DCR in coincidence at three different environmental temperature. (Measurement performed on Type 1 detectors at $V_{EX} = 2V$ and $\Delta T = 0.75ns$.)*

lation time of $10\,000\,\mathrm{s}$, in order to obtain a good statistics. The count rate distribution was acquired both in the presence and in the absence of the radioactive source. The pixel-by-pixel map of the differences between the acquired counts in the presence and in the absence of the radioactive source is reported in Fig. 4.5. The map does not exhibit any apparent gradient as expected from the experimental conditions, since the source size is much larger than the detector and was centered on it for the measurements.

In Fig. 4.6 the the count rate distribution in the presence and in the absence of the radioactive source is reported.

As highlighted by the histogram fitting in Fig. 4.7, the distribution follows a Poisson statistics with an average count rate per pixel induced by β particles of about $33\,\mathrm{mHz}$. The expected uncertainty due

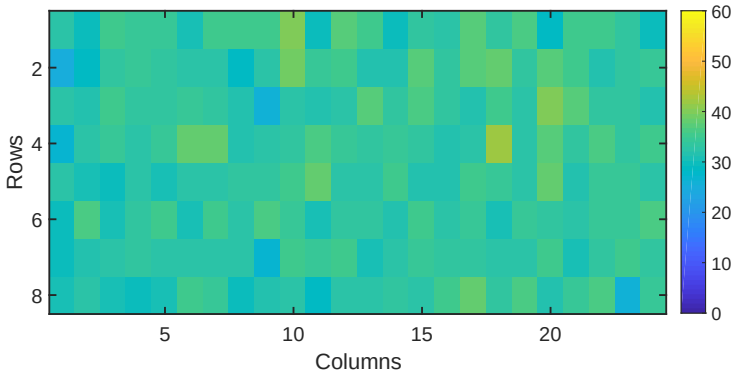

Figure 4.5: *Map of the differences pixel-by-pixel between the acquisition in the presence and in the absence of the radioactive source.*

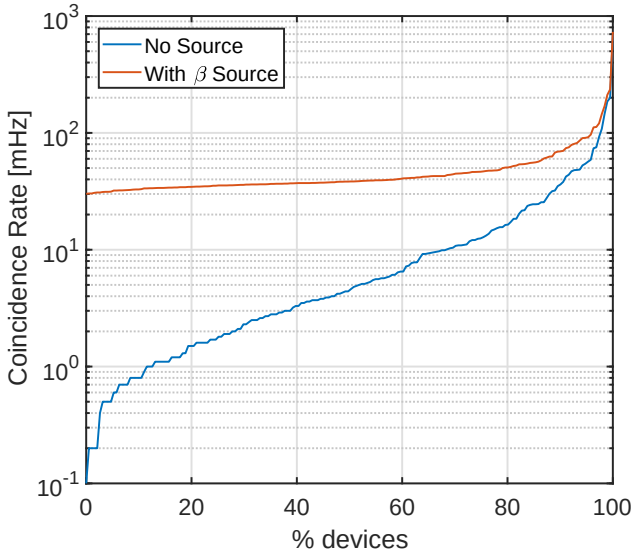

Figure 4.6: *Coincidence rate distribution in the presence and in the absence of the radioactive source.*

to Poisson statistics calculated by dividing the average counts by the total time of acquisition is $1.8\,\mathrm{mHz}$ very close to the measured uncertainty

of $2\,\mathrm{mHz}$.

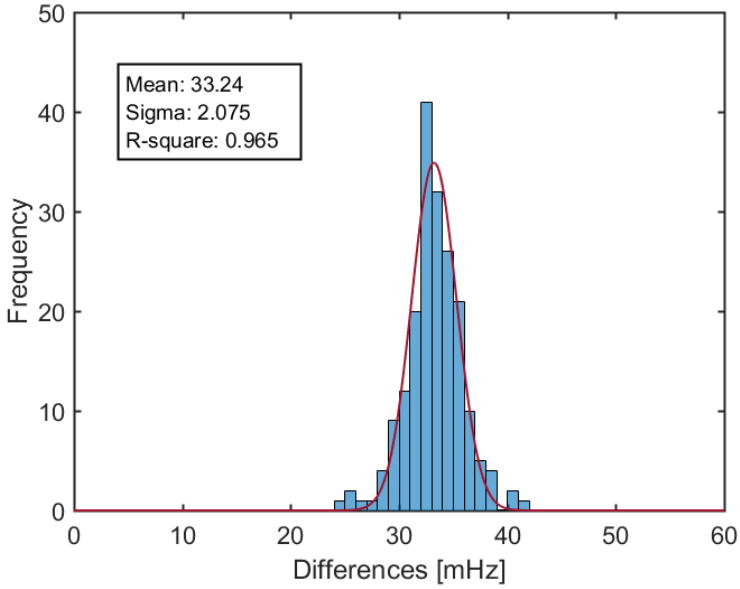

Figure 4.7: *Histogram of the differences pixel-by-pixel between the acquisition in the presence and in the absence of the radioactive source.*

The experimentally measured $33\,\mathrm{mHz}$ per pixel count rate corresponds to $8.8\,\mathrm{Hz\,mm^{-2}}$ that is in good agreement with the expected particle-induced count rate of $7.3\,\mathrm{Hz\,mm^{-2}}$ predicted by the MC simulations. The small difference between the measured rate and the predicted rate can be attributed to uncertainties within the MC simulation.

In particular, the geometrical fill factor for charged particles could be higher with respect to the optically measured one. Although this hypothesis should be experimentally confirmed in the APiX prototype with a nearly orthogonal incidence particle beam, measurements performed by Marrochesi et al.[127] on SiPMs suggested an increase of the geometrical fill factor for charged particles with respect to the optical fill factor.

4.2 Neutron irradiation

The measurement reported in the previous section demonstrated functionality of the prototype for the detection of charged particles. In order to evaluate the degradation of this device if operated in hard radiation environments, an irradiation campaign with neutrons has been performed. In this section the results of this characterization are reported.

4.2.1 Description of the irradiation campaign

An irradiation campaign with neutron was performed at the INFN Laboratori Nazionali di Legnaro (LNL) in order to evaluate the radiation tolerance of the detectors.

The irradiation campaign was carried out at the "Van de Graaff" CN accelerator facility of the LNL where different neutron fluences were generated by the collision of $5\,\mathrm{MeV}$ protons on a thick beryllium target. The neutron fluences were produced by the variation of the proton current hitting the beryllium target.

The neutron yield Y_n, which depends on the number of emitted neutrons per unit energy and on the charge hitting the beryllium target, is defined by the following equation:

$$Y_n = \frac{dN}{dEdQd\Omega} \tag{4.3}$$

where N is the number of neutrons emitted, E is the energy, Q is the impinging charge and Ω is the emission solid angle [128].

It is worth noticing that even if the neutron yield depends on the emission solid angle Ω, at the experimental condition at which the irradiation was performed the variation of the neutron yield with the angle can be considered negligible. This assertion is a consequence of the small solid angle covered by the device during the irradiation, since its area is few mm^2, much smaller with respect to the distance of the device from the beryllium target ($48\,\mathrm{mm}$). In Fig. 4.8 the schematic representation of the irradiation setup is depicted.

The irradiation campaign was planned to be performed on several dies of single-layer devices (i.e. 5 top chip devices). To be able to

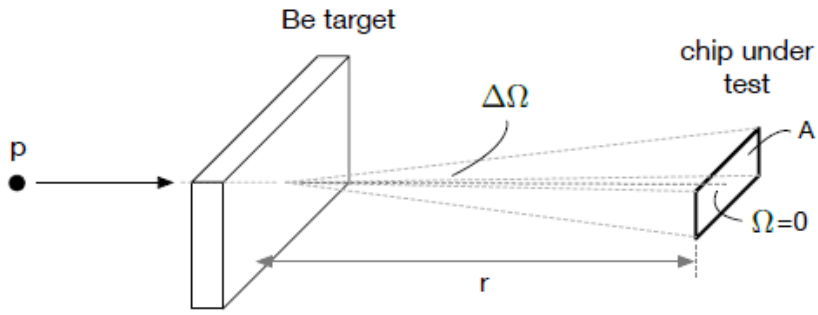

Figure 4.8: *Sketch of the irradiation setup[112].*

acquire the DCR distributions of irradiated samples shortly after the irradiation, a portable experimental setup was designed and produced to provide bias to the detectors and to connect the acquisition board. The in-situ acquisition of the DCR offers two main advantages: the neutron fluences can be tuned according to the results and the short-term annealing component of radiation damage can be evaluated.

In table. 4.2 the list of the runs performed during the irradiation campaign is reported with the exposure time and relative fluences obtained.

Table 4.2: *List of the irradiation runs reporting the exposure time, the proton current and neutron fluence.*

run ID	Chip ID	Charge [μC]	Irradiation time [s]	Proton current [μA]	Fluence [$n\ cm^{-2}$]
run 1	C4	240	260	1.2	1.E+09
run 2	C3	6	9000	800	1.E+11
run 3	C2	600	750	850	1.E+10
run 4_1	C1	1.8	2300	800	3.E+10
run 4_2	C1	18	22628	800	3.E+11
run 5	C5	180	412	0.44	3.E+09
run 6	C5	120	135	0.89	2.E+09

Five devices were irradiated with different fluences from a minimum of $10^9 n\ cm^{-2}$ up to a maximum fluence of $3 \times 10^{11} n\ cm^{-2}$.

After each irradiation run the DCR distributions of both types of detectors were acquired. The irradiation and the DCR acquisition were

performed at room temperature, while when not being characterized the devices were kept at $-18\,^{\circ}\mathrm{C}$ to prevent annealing.

4.2.2 Results of the irradiation campaign

In Fig. 4.9 and in Fig. 4.10, the DCR distribution of the devices irradiated at different neutron fluences is reported respectively for Type 1 and Type 2 detectors. As the fluence increases the DCR becomes higher. While the continuous lines refer to the DCR at the end of the irradiation run, dashed lines refer to DCR measured during an interruption of the irradiation within the same run.

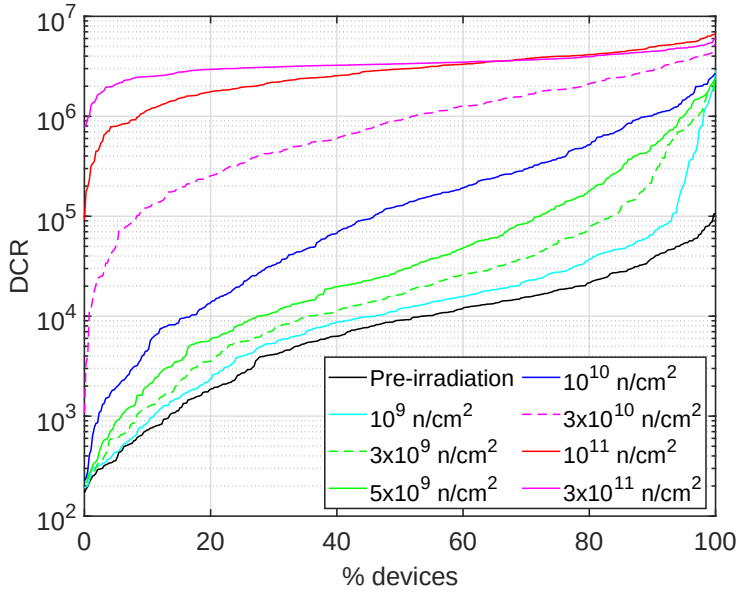

Figure 4.9: *DCR distributions for the Type 1 detectors irradiated at different neutron fluences.* $V_{EX} = 1V$ *at room temperature.*

While the irradiation and in-situ measurements were performed at room temperature, the post irradiation characterization was performed in a stabilized environment at $20\,^{\circ}\mathrm{C}$ placing the setup in a climatic chamber. After the irradiation campaign an annealing procedure was

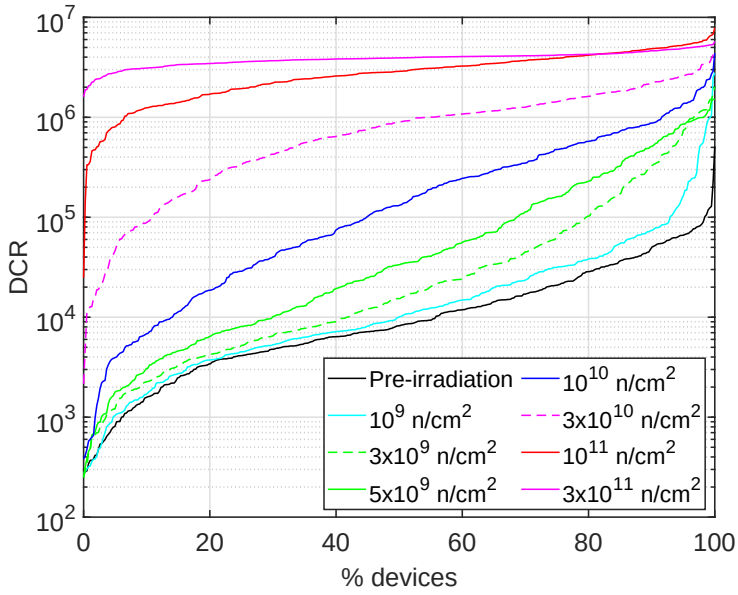

Figure 4.10: *DCR distributions for the Type 2 detectors irradiated at different neutron fluences.* $V_{EX} = 1V$ *at room temperature.*

performed in order to partially recover the radiation damages by heating the devices at $60\,^{\circ}\mathrm{C}$ for 80 minutes.

In Fig.4.11, the comparison of the DCR distributions of two different irradiated devices before and after annealing is reported to show the effect of the annealing procedure.

The interaction of neutrons with the detectors generates defects in the bulk with the number of displacements and the volume of interaction depending on the neutron energy. The DCR increase in the irradiated detectors is a consequence of displacements generated in the depletion region of the detectors, that act like Shockley-Read-Hall generation centers[129].

The number of displacements generated in the active volume of the detectors (i.e. depletion region) by the neutron irradiation can be reasonably assumed proportional to the neutron fluence and to the thickness of the depletion region times the detector area.

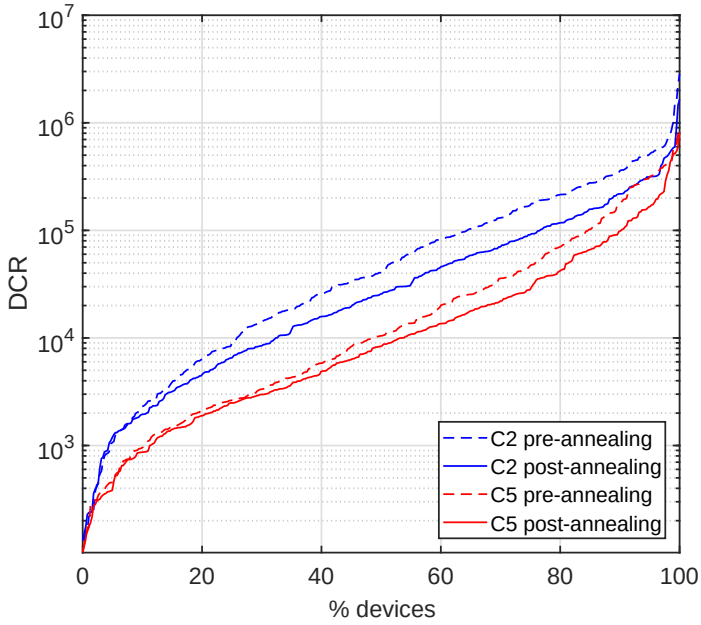

Figure 4.11: *DCR distributions of two different devices (C2 & C5) before and after the annealing procedure. Type 2 detectors,* $V_{EX} = 1V$ *and* $T = 20°C$.

The DCR increase is subjected to the stochastic nature of the processes involved in the creation of defects, that can be emphasized by the small sensitive volume of the SPADs.

Moreover, the effectiveness of a defect on the increase of DCR may change depending on the position of the defect inside the active region of the device. Defects closer to the junction are subject to a high-field region that enhance their probability to generate an electron-hole pair through trap-assisted tunneling with respect to defects located near the neutral region, that experience a smaller electric field leading to a lower generation rate.

At smaller fluences only a portion of the pixelated array experience an increase of DCR. This behaviour is a consequence of the defect generation in the small active volume that involves a limited number of pixels at these fluences. As the fluence increases, the generation of defects

in the active volume extends to all the pixels in the array; furthermore, an accumulation of defects may take place in single pixels, leading to an increase of the DCR of more than two order of magnitude. At the highest fluence considered in this study, the DCR distribution exhibits a saturation level due to the detector dead-time that limits the maximum count rate in each pixel.

In addition to the DCR increase related to the neutron-induced generation of defects in the active region of the detectors, a possible change in the breakdown voltage due to irradiation has also been considered.

The effect of radiation damages on the breakdown voltage was evaluated by performing a voltage sweep and measuring the DCR for each voltage value, as described in chapter 3. In Fig.4.12, the histograms of the breakdown voltage are reported for both types of detectors for the chip C1, that was irradiated at the highest fluence. For both type of detectors the radiation effect was not so severe, leading to a reduction of the breakdown voltage in the order of few tens of mV, while the annealing does not affect its value.

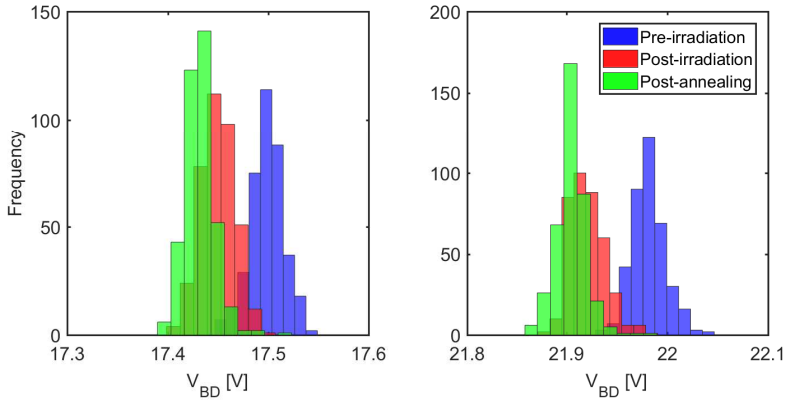

Figure 4.12: *Histograms of the breakdown voltage for chip C1 before and after the irradiation. (Left) Type 1 detectors, (Right) Type 2 detectors*

It is worth noticing that at the radiation levels reached during this irradiation campaign the performance of the front-end electronics composed of CMOS transistors is not substantially affected by the neutron

irradiation. Indeed, the bulk damages induced by neutron irradiation does not interfere with the readout circuit since it is based on MOSFET transistors that are known to be largely insensitive to bulk damage, since their working principle is based on the drift of majority carriers at the device channel surface[130]. Furthermore, $180\,\mathrm{nm}$ CMOS transistors have been proven to be tolerant to much higher radiation levels than the ones applied this campaign[131].

4.2.3 Dependence of the dark counts on neutron fluence

The dependence of dark current on the fluence in silicon radiation detectors have been studied in several works. The exposure to highly energy particles able to generates cluster defects makes the dark current linearly proportional to the particle fluence. Hence, in neutron irradiated samples a liner behaviour is expected since neutron irradiation generates mainly cluster defects. Conversely, for other types of radiation, such as γ-rays or low energy electrons, the dark current exhibits a strong non linear behaviour with respect to the particle fluence[97].

In Fig. 4.13, the mean DCR as a function of the neutron fluence is reported. Up to a fluence of $10^{11} n/cm^2$, the DCR exhibits a linear dependence with the fluence, as expected for neutron radiation. The loss of linearity at the highest fluence is a consequence of the DCR saturation due to the detector dead-time.

4.3 Proton irradiation

In this section a proton irradiation performed at the micro-beam line of the AN2000 accelerator facility of the INFN Laboratori Nazionali di Legnaro (LNL) is reported.

In this micro-beam line the apparatus is able to provide an ion pencil beam having just a few micrometer transverse size, typically used for probing or changing the surface characteristics of materials in a highly controlled way.

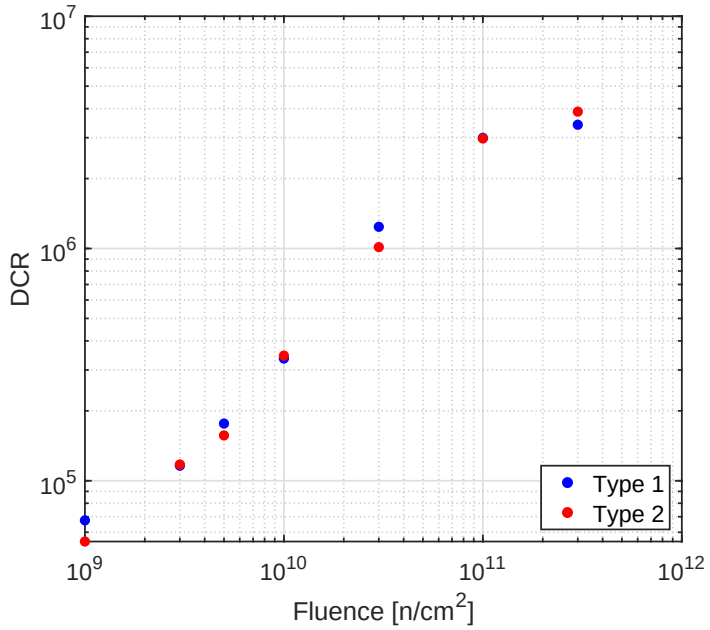

Figure 4.13: *Mean DCR as a function of the neutron fluence*

4.3.1 Experimental setup

The irradiation of samples with neutrons described in the previous section was performed without biasing the detectors during the irradiation and performing the functional characterization off-line shortly after the irradiation.

The primary purpose of the proton irradiation with a micro-beam was to perform on-line measurements on single layer devices. To avoid the ionization of ambient air with related scattering effects, the proton micro-beam is confined in a vacuum chamber where the devices under investigation have to be placed. This configuration required the design and fabrication of a dedicated sample holder with custom cables to connect the devices to the external interface board to perform the measurements.

In Fig. 4.14, the vacuum chamber with the designed samples holder

is reported together with the custom connection cables. In the metal frame employed to hold the PCB for the device connection, a commercial SiPM covered with a scintillator layer was placed to acquire the proton count rate. On the same vertical axis connecting the SiPM and the device under test a small copper micro-grid was also placed to be able to align and define the cross-section of the proton micro-beam.

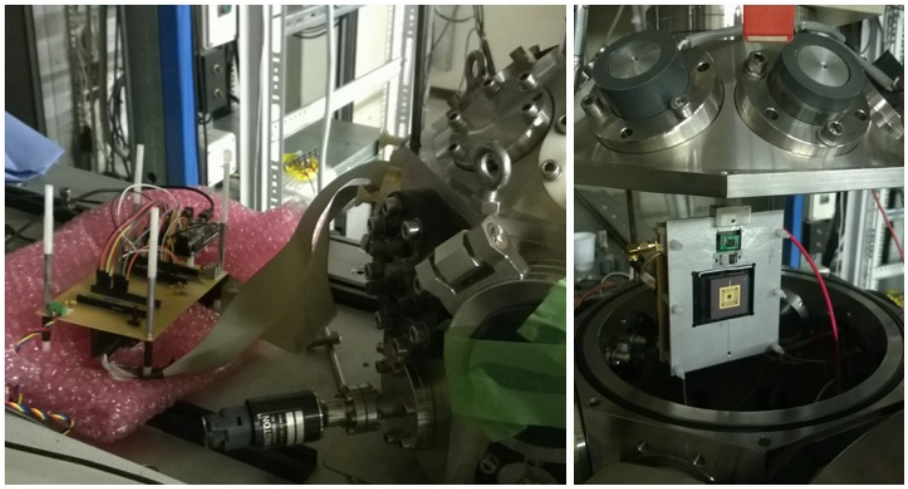

Figure 4.14: *Experimental setup used in microbeam irradiation experiments. Interface board connected trough custom cables to the vacuum chamber (Left). Vacuum chamber open with the metal frame holding the device PCB, the SiPM and copper micro-grid (Right).*

4.3.2 Preliminary setup configuration

A first beam configuration was performed hitting the copper micro-grid placed on the metal frame of the sample holder in order to reconstruct a secondary X-ray image of the grid to evaluate the beam parameters in terms of cross-section and divergence.

As described in the previous subsection, a commercial SiPM covered with a scintillator layer was used to measure the proton rate. The pencil micro-beam of $2\,\mathrm{MeV}$ protons, having a cross-section of $\sim 1\,\mu\mathrm{m}^2$ was used to make a raster scan of $250 \times 250\,\mu\mathrm{m}^2$ over the scintillator sur-

face. The raster scan over a large area was performed to prevent a fast degradation of the scintillator, while the acquisition of different proton rates, obtained by varying the beam intensity, was completed by changing the illumination spot over the scintillator surface, also in this case to avoid the degradation.

In Fig. 4.15, the proton rate at different beam intensities is reported for two different spots over the scintillator surface. The proton rate can be efficiently tuned by the variation of beam intensity, raster scan area and the velocity of the scan.

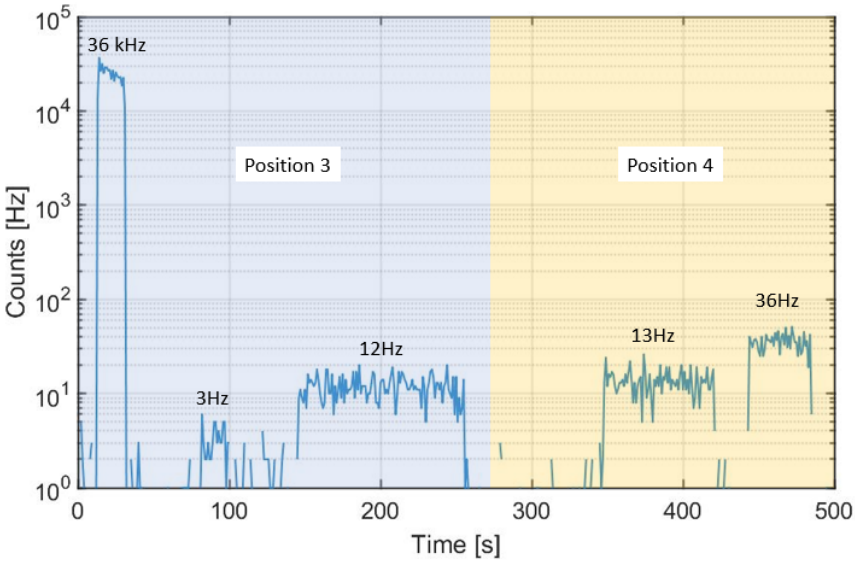

Figure 4.15: *Evaluation of the proton count rate with the SiPM covered with a scintillator layer. In order to avoid the degradation of the scintillator during the measurement, different spots on the scintillator surface were monitored during the measurement.*

The last phase of the preliminary setup configuration was the precise alignment of the micro-beam on a desired pixel within the array, having a low DCR in the order of few hundreds of Hz. To enable this fine alignment, a coarse scan in the border region of the device was performed to acquire a secondary X-ray image of a marker of the chip. Once detected the marker position the beam can be easily moved to the desired pixel

within the array.

In Fig. 4.16, the secondary X-ray image of the alignment is reported together with a micrograph of the same area for comparison.

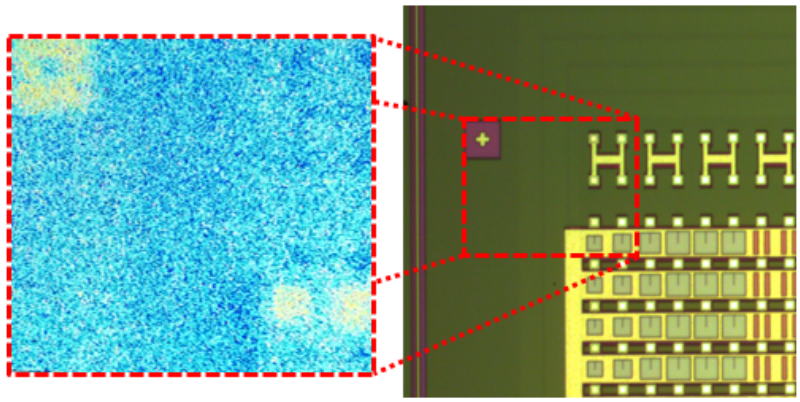

Figure 4.16: *Secondary X-ray image of the alignment marker compared with a micrograph of the same area.*

4.3.3 On-line proton measurement

The on-line detection of protons was performed using selected pixels with low DCR. After the selection of a low noise pixel, its output signal was recorded biasing the pixel at $1\,\mathrm{V}$ of excess voltage while illuminating its surface with the micro-beam. To ensure a uniform illumination of the pixel with the $\sim 1\,\mu\mathrm{m}^2$ micro-beam, a raster scan over the pixel active area was performed avoiding to illuminate the in-pixel electronics at the side of the detector.

In Fig. 4.17, the signal output of the pixel under proton irradiation is reported. As soon as the micro-beam was switched on the count rate increases by $100\,\mathrm{Hz}$, which is the expected proton rate on the detector. However, shortly after, an increase of DCR is detected. Also in this case, the increment could be attributed to the generation of defects within the active region of the detector. The DCR increase as a function of the proton dose was acquired also in the second switching-on of the micro-beam.

The step-shaped increase of DCR with the radiation dose in silicon GM-APDs detectors has already been reported in literature[132]. The creation of defects in the active region explains the DCR increase, while the step shape could be addressed to the generation of cluster of defects.

In the transient signal reported in Fig. 4.18, the proton rate is lower than the pixel DCR, and thus it was not possible to detect it at the micro-beam switch-on. Moreover, for about $100\,\mathrm{s}$ after the beam has been switched on, no DCR increase related to defects generation is detected. This can be explained considering the stochastic nature of defects generation, that during this time window were not generated in the active region of the detector. As the dose increases by keeping the beam on, the DCR increases in steps as the cluster defects are generated.

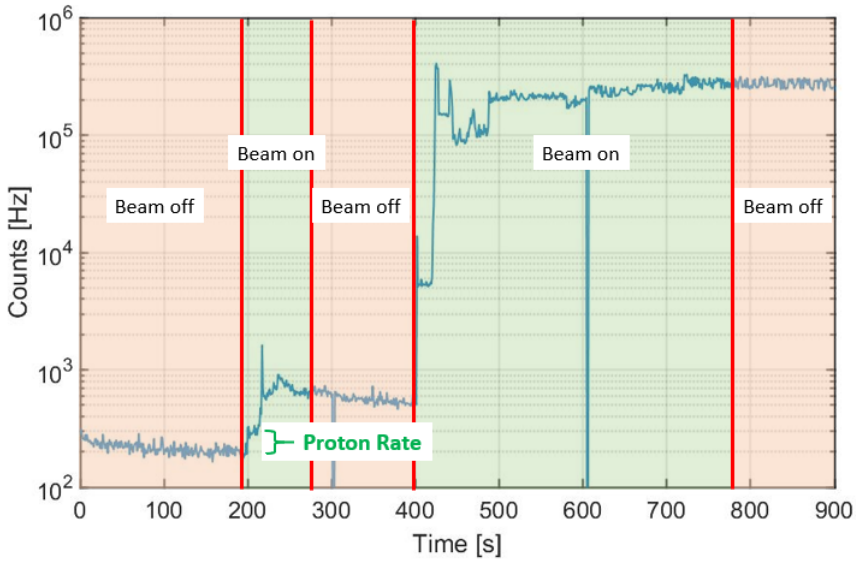

Figure 4.17: *Output signal of a pixel detector under proton irradiation with a* $\sim 1\,\mu\mathrm{m}^2$ *micro-beam raster scanned over the pixel surface. At the micro-beam switching on the proton rate was detected.*

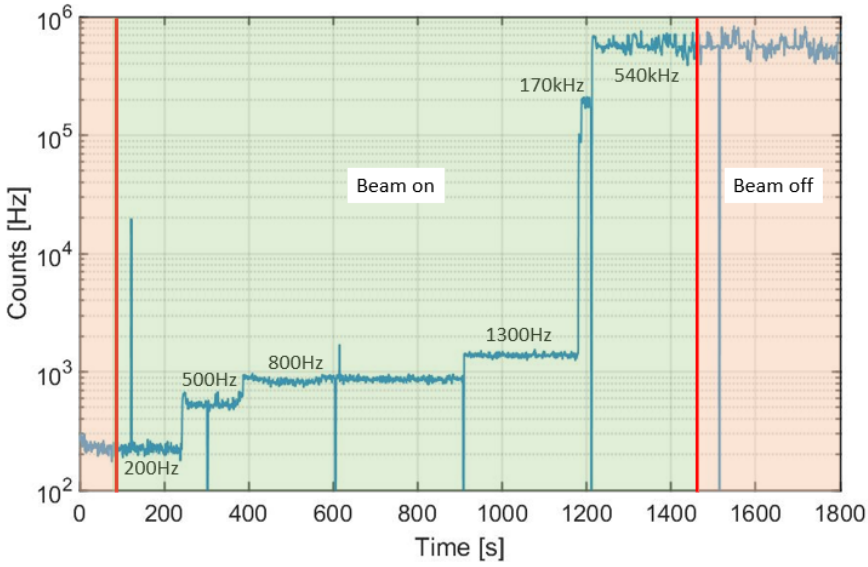

Figure 4.18: *Output signal of a pixel detector under proton irradiation with a* $\sim 1\,\mu\mathrm{m}^2$ *micro-beam raster scanned over the pixel surface. Step shaped DCR increse generated by the proton irradiation.*

4.4 Conclusions

Radiation levels evaluated in the irradiation campaign reported in this chapter are relatively moderate with respect to the harsh environment of future linear colliders[133]. In this moderate environment the devices did not showed an adequate radiation hardness, with a detrimental increase in the DCR. This evaluation provided anyway useful indications for future detectors. The prototype with this configuration could be successfully employed as beta prober for guided microsurgery with beta-tracker [134], while the integration of more than two layers in a multi-stack configuration can further reduce the DCR, extending in this way the ability of the coincidence detectors to operate in higher levels of radiation than the ones evaluated in this dissertation.

CHAPTER 5

SiPM based Time-of-Flight range meter

This chapter reports on the results of an evaluation campaign of measurements of different types of Silicon PhotoMultipliers (SiPMs) designed and fabricated at the Fondazione Bruno Kessler (FBK), used as receiver for a direct Time-of-Flight (ToF) range meter.

SiPMs take advantage of the characteristics of GM-APDs such as high sensitivity, high efficiency and very low time jitter, and overcome the problem related to the dead time connecting several sensitive elements in parallel, making them suitable for the simultaneous detection of more than one photon [5].

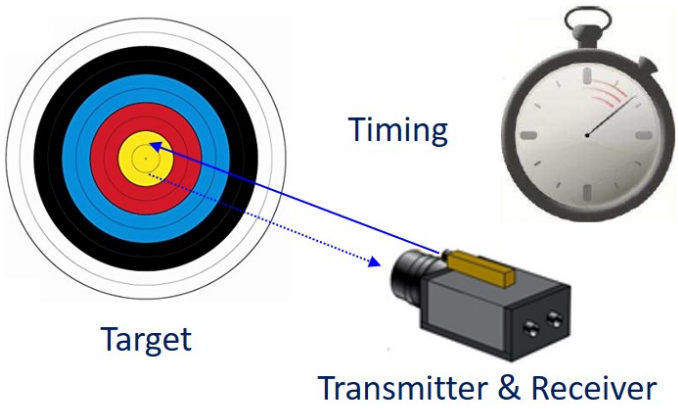

Figure 5.1: *Schematic illustration of the working principle of Time-of-Flight systems.*

5.1 Direct Time-of-Flight(ToF) range meter working principle

In optical Time-of-Flight (ToF) techniques, the distance of a target is measured starting from the propagation time of an optical signal. In an indirect ToF system, the phase shift between a modulated light source, either continuous-wave or a burst of pulses, and the detected signal is acquired, while a direct ToF system measures the time required to an optical pulse to perform a round-trip after being reflected from a target.

Direct ToF range meters are generally composed of a laser emitter, a receiver and a time measuring unit that acquires the time delay between the emission of a laser pulse and the detection of the back reflected light pulse. In direct ToF systems, the distance of a target is calculated from the measured time delay with the following equation:

$$D = \frac{\Delta T \times c}{2} \tag{5.1}$$

where D is the distance of the target, c is the light velocity in the medium and ΔT is the measured delay. In Fig. 5.1, the working principle of a ToF system is shown.

In order to have a good timing resolution and extend the distance

range of measurement, it is desirable to use laser pulses with a small FWHM and a high peak amplitude [135].

If the available acquisition rate is larger than the one required by the application, the single-shot precision can be further improved by filtering, and the measurement error can be reduced to very low levels by calibration. A high acquisition rate is also required to use the range meter for real-time imaging in combination with a scanning mirror [8].

Notwithstanding the extremely high peak power, the very short pulse length and the high pulse repetition rate that can be achieved with lasers operating in Q-switching mode [135], their cost and high power consumption limits the utilization of this class of lasers in most ToF applications. As an alternative to Q-switching lasers, gain-switching emitters can be used as a sub-ns light source in compact ToF systems. Kostamovaara et al. [6] reported a laser ranging operating in enhanced gain-switching mode with a FWHM of $\sim 100\,\mathrm{ps}$ and high-energy.

The receiver unit requires detectors with a good detection efficiency and fast response. Avalanche Photodiodes (APDs) are typically used for this application thanks to their good detection efficiency [135]. Geiger-Mode APDs feature a good detection efficiency as a result of their high gain and excellent timing response. Several works using these detectors in ToF range meters have been reported [136, 6, 137, 138]. SiPMs have also been proposed for ToF systems, and a few articles report a comparison between SiPMs and APDs in Lidar systems [139, 140, 141, 142].

The time measuring unit requires a high resolution in order to time-stamp the fast output signal of the receiver. Its typical configuration includes a comparator and a Time to Digital Converter (TDC). In order to reduce coupling interferences with the receiver, TDC and detectors can be integrated in a single ASIC [143, 144]. Pellegrini et al. [145] reported a first generation of Time-of-Flight system (VL6180) based on the STM SPAD technology, which represent an industrialised integrated device that is capable of range up to $60\,\mathrm{cm}$ in $60\,\mathrm{ms}$. Concerning the realization of a compact ToF system, low-cost FPGA-Based TDCs [146] represent a good alternative to dedicated ASICS in prototyping and low volume applications.

In the research activity reported in this chapter, a first set of measurement was performed by employng three different SiPMs in NUV and NUV-HD technology, designed and fabricated at Fondazione Bruno Kessler, with the same active area but different cell sizes as receiver in a ToF range meter [147, 148]. A $405\,\mathrm{nm}$ laser diode was employed to exploit the higher Photon Detection Efficiency of the receiver at this wavelength. The effect of ambient light was evaluated with a fixed target at $70\,\mathrm{cm}$ and the performance of the system was investigated moving the target from $25\,\mathrm{cm}$ to $215\,\mathrm{cm}$ changing the ambient light illuminance.

In a subsequent set of measurement, the feasibility of a SiPM-based range meter in the NIR spectral region was evaluated by employing a high-energy short-pulse multiple quantum well laser diode with $810\,\mathrm{nm}$ spectral peak, designed at the Circuits and Systems Research Unit of the ITEE Faculty of the University of Oulu, in conjunction with SiPMs with two different cell-size with an enhanced PDE in the NIR region designed and developed at the FBK. The results of this set of measurement are reported and discussed in section 5.4.

5.2 Experimental Setup

In this section an in-depth description of the experimental setup is reported by highlighting the building blocks of a typical ToF range meter.

The experimental setup, consisting of a laser emitter (Transmitter), a SiPM receiver, a moving target, a Time Correlated Single Photon Counter (TCSPC) measurement system and a dual waveform generator is conceptually schematized in the block diagram in Fig. 5.2.

5.2.1 Receiver

The laser pulse back reflected from the target was acquired with a SiPM connected to an amplifier board with a pole-zero compensation stage [149] in order to convert the current output of the SiPM to a sharp voltage pulse. This configuration was found to offer a fast baseline recovery, therefore minimizing the time walk due to uncorrelated cell triggers.

A commercial $405\,\mathrm{nm}$ laser diode was chosen for the transmitter unit since at this wavelength, the PDE of the Near-UV enhanced SiPMs

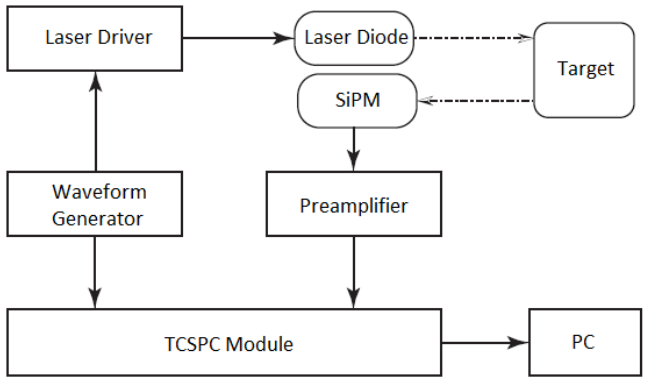

Figure 5.2: *Block-diagram of the experimental setup.*

adopted in this study is maximized. The excess voltage applied to the different SiPMs was defined considering a trade-off between a good Photon Detection Efficiency (PDE) and a low level of correlated noise due to crosstalk and afterpulsing. The excess voltage was set at $4\,\mathrm{V}$ for the $40\,\mu\mathrm{m}$ cell-size device and $8\,\mathrm{V}$ for the $20\,\mu\mathrm{m}$ and the $15\,\mu\mathrm{m}$ cell-size device. In this operating conditions, the single-cell output signal amplitude was respectively $7\,\mathrm{mV}$, $6.5\,\mathrm{mV}$ and $4.1\,\mathrm{mV}$ with a PDE of $37\,\%$, $44\,\%$ and $34\,\%$ [150, 147, 148].

Breakdown voltage extraction

In order to properly provide the desired operating overvoltage to the SiPMs an estimation of their breakdown voltage was performed in a set of preliminary measurements. The SiPMs placed in the dark were biased at different voltages and the single-cell output was acquired. In Fig. 5.3, the single-cell output amplitude as a function of bias voltage is reported. The breakdown voltages were extracted from the intercept of the linear regression of the single-cell output amplitudes with the horizontal axis.

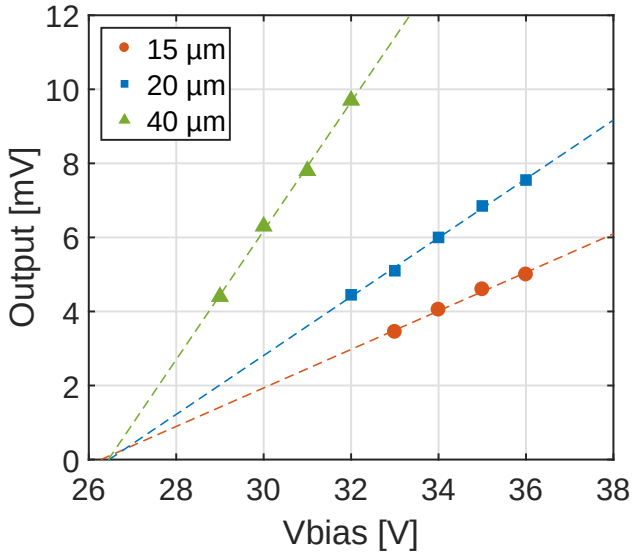

Figure 5.3: *Breakdown voltage extraction from the single-cell output signal amplitude as a function of bias voltage.*

5.2.2 Optics

To focus the light reflected from the target on the SiPM, a lens with NA=0.6 was placed in front of the receiver. The distance from the SiPM and the lens was adjusted to have the SiPM slightly out-of-focus, in order to exploit its whole area for light detection. In this configuration the light is spread on most of the SiPM cells, not just few of them, therefore signal dynamic range is enhanced with respect to a perfectly focused receiver.

In order to analyse the effect of ambient light in the first set of measurements, no filters have been used in the receiver optics. Subsequently, in the activity reported in section 5.3.4 an optical band pass filter centred at $405\,\mathrm{nm}$ was placed in the optics of the receiver to evaluate the improvement in the system performance after ambient light filtering.

5.2.3 Transmitter

The laser diode driver was fabricated with a logic integrated circuit as described in [114]. A dual waveform generator was used to generate the TTL signal, provided to the laser driver module, and a synchronized signal provided to the TCSPC module. The laser module, emitting an average optical power of $140\,\mu W$, was used with a repetition rate of $10\,MHz$. The use of a commercial laser driven by a logic integrated circuit was conceived with the aim to pursue the realization of a compact ToF range meter device.

5.2.4 Acquisition system

The core of the system is the TCSPC module, which includes a Time-to-Digital Converter (TDC) and a memory for TDC data histogram storage [151], used to acquire time-of-arrival histograms of the laser pulse back reflected from the target. This module records the time distribution between two signals entering the two input channels. The first channel was connected to the synchronization output of the dual waveform generator (start event), while the second channel was connected to the SiPM output (stop event). The voltage threshold for the two input channels of the TCSPC module could be set independently for the start and stop signals.

In order to evaluate the system performance at different ambient light intensities, a withe LED was placed close to the target. Tuning the current provided by the LED power supply, it was possible to change the ambient light illuminance on the target from few lux to $1.1\ klux$.

The target was made of a white paper sheet attached to a holder, that was mounted on a metallic rail allowing the distance of the target from the emitter to be easily changed. The range of position covers a distance from $25\,cm$ to $215\,cm$. The closer position was limited by the size of the target holder, while the maximum distance was determined by the size of the rail.

5.3 Preliminary measurements

The results of the preliminary set of measurements are reported in this section. Three different types of analysis have been addressed: an evaluation of the effect of ambient light on the performance of the different types of SiPMs performed on a target placed at a fixed distance, a comparison of their achievable distance ranges and an investigation of the effect of ambient light filtering.

5.3.1 Threshold voltage selection

The threshold voltage for the receiver channel in the TCSPC module was selected by acquiring the count rate induced by ambient light impinging on the fixed target. The threshold was selected to have in the worst case a detection rate of uncorrelated photons lower than $5\,\%$ of the laser repetition rate.

In Fig. 5.4 the count rate induced by ambient light as a function of illuminance is reported. The $40\,\mu\mathrm{m}$ and $20\,\mu\mathrm{m}$ cell-size devices exhibit a similar trend: a first rising edge, a maximum and then a decreasing tail. In the rising part of the curve, as ambient light grows, a higher number of cells fires leading to an increase in the count rate. The decreasing tail after the maximum is a consequence of the finite recharge time of the SiPM cells. As the illuminance increases the average SiPM signal is reduced since the probability that a cell triggers before its recharge is completed is higher.

The $15\,\mu\mathrm{m}$ cell-size device does not reach the maximum of count rate within the illuminance range that can be generated with the available setup, thus the maximum count rate for this device is reached during the rising edge of the curve at $1.1\,\mathrm{klx}$.

As the size of the cell of the SiPMs decreases the illuminance at which the count rate reaches the maximum level increases. This behaviour is a direct consequence of the different number of cells for the three different SiPMs. Since the overall active area is the same, $1\,\mathrm{mm}^2$, the number of cells is higher for small-size devices. The maximum count rate shifts from $30\,\mathrm{lx}$ for the $40\,\mu\mathrm{m}$ cell-size device to $350\,\mathrm{lx}$ for the $20\,\mu\mathrm{m}$ cell-size device.

In order to better understand the effect of ambient light on the receiver output signal an oscilloscope operating in persistence mode was used to acquire the laser triggered output signal of the $15\,\mu\mathrm{m}$ cell-size device at two different illumination condition. As the light level increases, the amplitude of the signal related to the laser peak is reduced as an effect of the lower number of cells available, while the background noise level increases. In Fig. 5.5, the output signal in the dark is compared with the output signal at $10\,\mathrm{lx}$ ambient light intensity

5.3.2 Effect of ambient light on a fixed target

In the first part of our experimental activity, the effect of ambient light was evaluated on a fixed target placed at $70\,\mathrm{cm}$ from the emitter. This set of measurements was acquired keeping a constant amount of reflected laser light.

Detection probability

After the selection of the threshold voltage, the laser pulse detection probability was evaluated as a function of ambient light illuminance. In Fig. 5.6 the results of this analysis are reported. As expected, the device with smaller cell size exhibits the best ambient light rejection. With a higher number of cells, even at high illuminance levels there are still enough available cells to detect the laser pulse. While the largest cell-size device shows a percentage of detected pulses lower than $90\,\%$ at around $300\,\mathrm{lx}$, the smallest cell-size device shows the same drop at around $1.1\,\mathrm{klx}$.

Precision and accuracy of the measurement

Systematic and random errors have been extracted from a gaussian fitting of the time-of-arrival histograms acquired with the TCSPC module. In Fig. 5.7 the single-shot time precision as a function of illuminance is reported. Time precision gets worse as the ambient light increases as a consequence of the lower laser pulse detection probability. While the $40\,\mu\mathrm{m}$ cell-size device exhibits the worst performance, the $20\,\mu\mathrm{m}$ and $15\,\mu\mathrm{m}$ devices show a similar behaviour, with the $15\,\mu\mathrm{m}$ cell-size

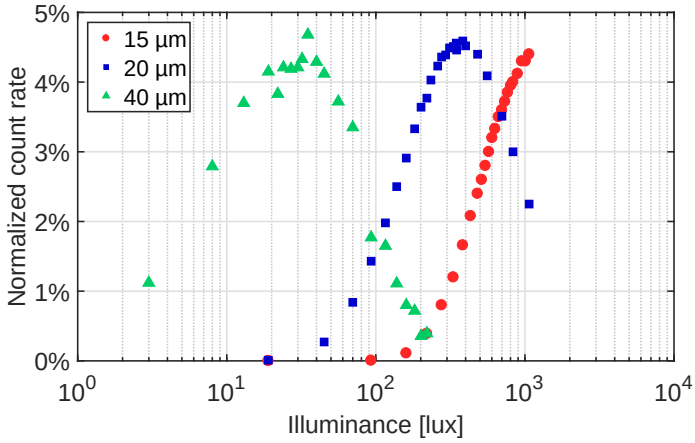

Figure 5.4: *Ambient light count rate as a function of illuminance.*

device having a slightly better time precision at each ambient light levels studied. In the whole range of illuminance the single-shot distance precision remains below $34\,\mathrm{mm}$.

Measurement accuracy is affected by the level of ambient light intensity, leading to an illuminance-dependent time shift, as reported in Fig. 5.8. As the ambient light intensity increases the time shift changes due to the change in threshold crossing time. The $40\,\mu\mathrm{m}$ cell-size device shows a much larger time shift compared to the smaller-size devices. As for the time precision, the SiPM with $15\,\mu\mathrm{m}$ cell-size exhibits the best performance in all the illuminance range.

5.3.3 Distance Measurements

While the measurements reported so far have been acquired with the target placed at a fixed distance, in this section the performance of the range meter is evaluated as a function of target distance. Time-of-arrival histograms were acquired at different positions of the target with a distance step of $10\,\mathrm{cm}$, except for the first measurement from $25\,\mathrm{cm}$ to $30\,\mathrm{cm}$, where the distance step is $5\,\mathrm{cm}$.

A comparison of the probability of laser pulse detection as a function of target distance for the three SiPMs is reported in Fig. 5.9 in the

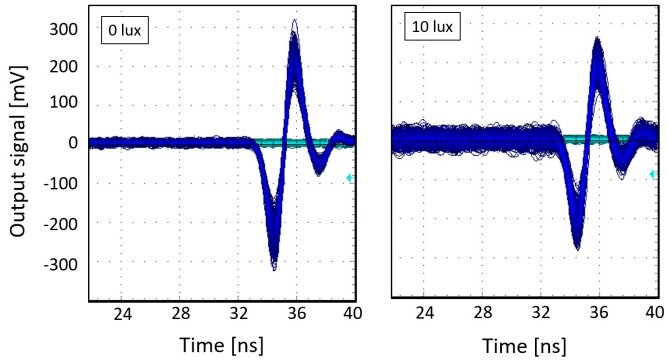

Figure 5.5: *Oscilloscope acquisition in persistence mode of the laser triggered output signal of the* $15\,\mu\mathrm{m}$ *cell-size device at two different ambient light intensities [152].*

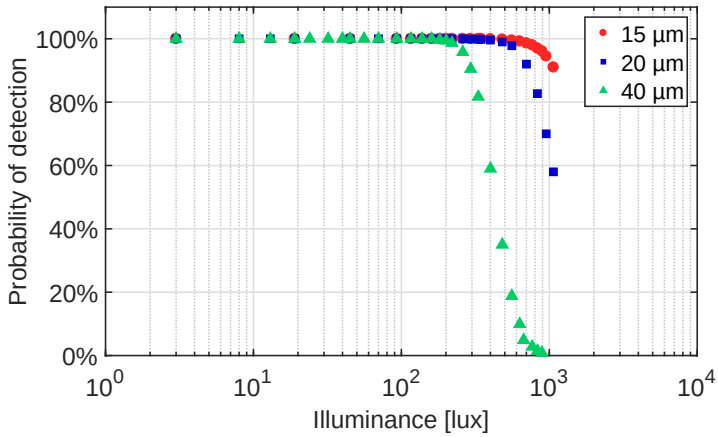

Figure 5.6: *Laser pulse detection probability as a function of ambient light intensity.*

absence of ambient light. The $40\,\mu\mathrm{m}$ cell-size device exhibits the best detection probability on a wider range of distances from $25\,\mathrm{cm}$ up to $120\,\mathrm{cm}$.

The reason of this behaviour can be found in its higher sensitivity compared to the other devices. The maximum range where the detection probability is close to $100\,\%$ for the smaller-sized devices ($20\,\mu\mathrm{m}$

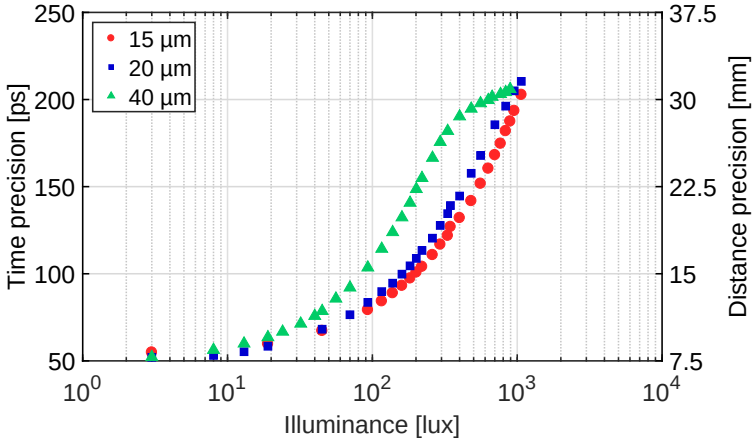

Figure 5.7: *Time precision as a function of ambient light intensity.*

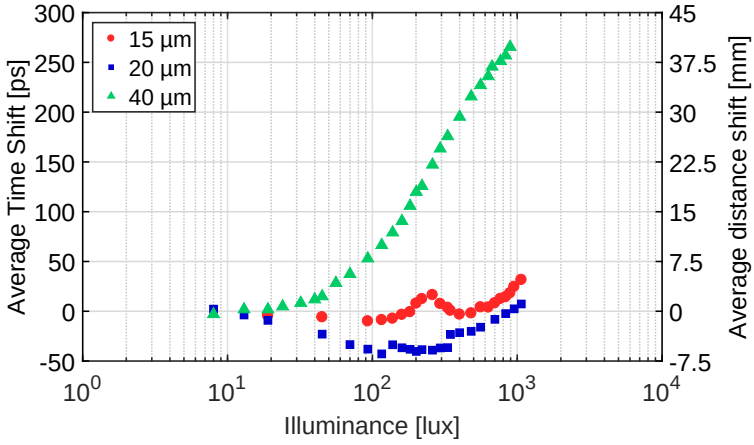

Figure 5.8: *Average time shift as a function of ambient light intensity.*

& 15 µm) is around 100 cm. Their response is very similar at higher distances, while there is a relevant difference at closer distances of the target. At a target distance from 25 cm to 40 cm the probability of detection for the 15 µm cell-size device is much lower than 100 %, while the 20 µm cell-size device displays the maximum probability of detec-

tion. This peculiar behaviour is related to the lower sensitivity of the $15\,\mu\mathrm{m}$ device and to the parallax problem.

The SiPM receiver mounted on its preamplifier board and the laser diode mounted on its holder are physically separated by $6\,\mathrm{cm}$ on a transversal plane. As a consequence of this distance between emitter and detector, the back-reflected light falls on the SiPM in a different position as the target is moved. The system was aligned to have the maximum of the signal when the target is placed at $70\,\mathrm{cm}$ from the emitter. At lower distances the laser hitting the target in a different position leads to a reduction of the SiPM output signal. This reduction is visible only for the smaller cell-size device in the dark dark because of its smaller sensitivity compared to the other devices.

In Fig. 5.10 the same type of measurement is reported with an ambient light illuminance increased to $300\,\mathrm{lx}$. The effect of ambient light on the probability of detection is very strong, especially for the $40\,\mu\mathrm{m}$ cell-size device. The measurement range is strongly reduced and the maximum probability of detection is lower than $90\,\%$. The smaller cell-size devices show a less severe reduction of the detection probability, both having a pulse detection probability larger than $90\,\%$ in the distance range from $50\,\mathrm{cm}$ to $90\,\mathrm{cm}$.

In Fig. 5.11, the probability of detection for the $40\,\mu\mathrm{m}$ cell-size device as a function of the target distance is reported at four different ambient light illuminance levels.

The range of distances where the probability of detection is higher than $80\,\%$, is strongly reduced in the presence of ambient light. In the absence of ambient light, the range of distances extends from $25\,\mathrm{cm}$ to $120\,\mathrm{cm}$, while at $100\,\mathrm{lx}$ of illuminance it is reduced from $50\,\mathrm{cm}$ to $100\,\mathrm{cm}$. At an ambient light level of $300\,\mathrm{lx}$ only a couple of measurement points around $70\,\mathrm{cm}$ exceed $80\,\%$ detection probability, while at $700\,\mathrm{lx}$ the probability is strongly reduced below $5\,\%$.

The time-of-arrival histograms recorded with the TCSPC module were analysed to extract information on random and systematic measurement errors. Results are reported in the absence of ambient light and at $300\,\mathrm{lx}$.

In Fig. 5.12 a) the time and distance precision are reported in the

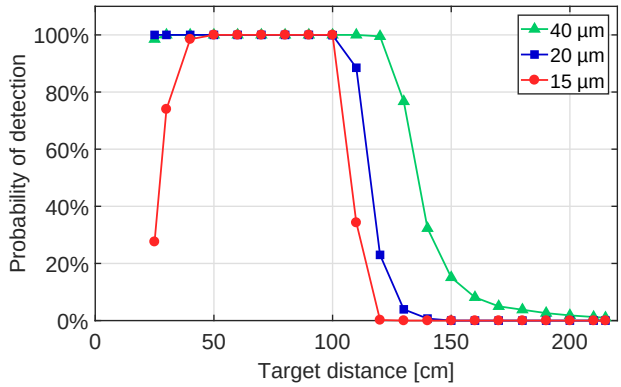

Figure 5.9: *Probability of detection as a function of target distance at* $0\,\mathrm{lx}$.

absence of ambient light. The three different SiPMs exhibit a similar behaviour with the minimum time precision of about $50\,\mathrm{ps}$, that is obtained at a target distance of $70\,\mathrm{cm}$, in agreement with the maximum of the SiPMs output signal at this distance.

As the illuminance is increased to $300\,\mathrm{lx}$, as shown in Fig. 5.12 b), the time precision becomes globally worst with the minimum value slightly above the $100\,\mathrm{ps}$. At this ambient light level, the three different SiPMs behaviours diverge at greater distances, with the $40\,\mu\mathrm{m}$ cell-size device showing the worst time precision while the $15\,\mu\mathrm{m}$ cell-size device displays the best performance.

The mean value of each time distribution was extracted and a linear fitting was performed to evaluate the linearity of distance measurements. The average time shift was determined by subtracting the mean value of each time distribution from the corresponding value in the linear regression of the measured data. In Fig. 5.13 the average time shift is reported as a function of the target distance. The three different SiPMs display a comparable behaviour and the influence of the ambient light is not evident in this case. The smaller cell-size devices exhibit a slightly better performance compared to the $40\,\mu\mathrm{m}$ cell-size device.

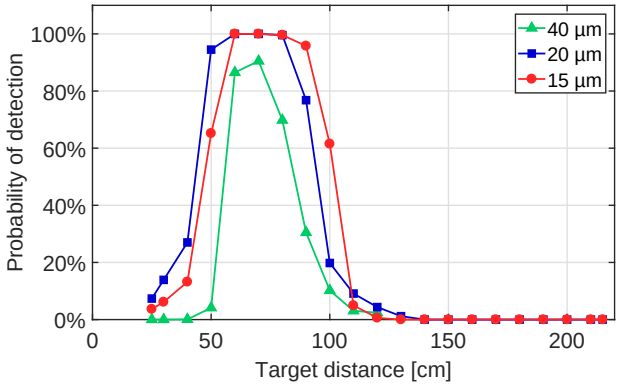

Figure 5.10: *Probability of detection as a function of target distance at* 300 lx.

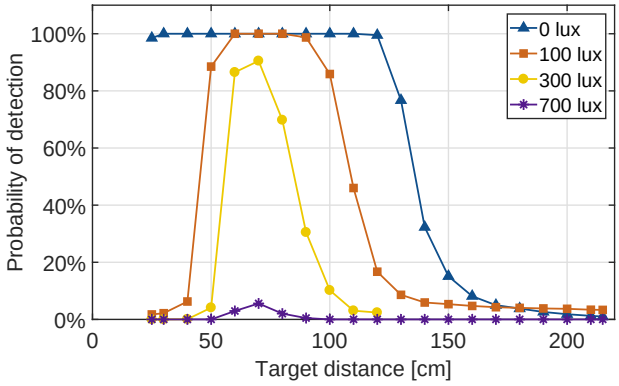

Figure 5.11: *Probability of detection as a function of target distance of the* 40 µm *SiPM at four different ambient light illuminaces.*

5.3.4 Ambient light filtering

The measurements reported so far were acquired without an optical filter in order to verify the performance of the three SiPMs with demanding background light conditions.

Fig. 5.14 shows the optical spectrum of the laser diode together with the spectrum of the white LED, used to mimic the indoor ambient light illuminance. As can be observed, the two spectra do not overlap. Plac-

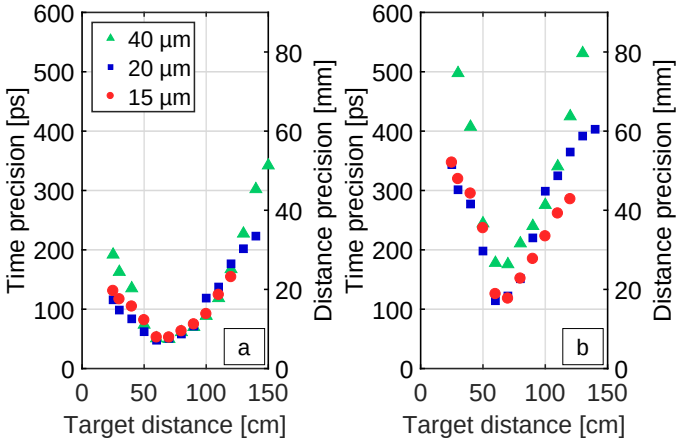

Figure 5.12: *Single-shot time and distance precision as a function of target distance. a)* 0 lx, *b)* 300 lx.

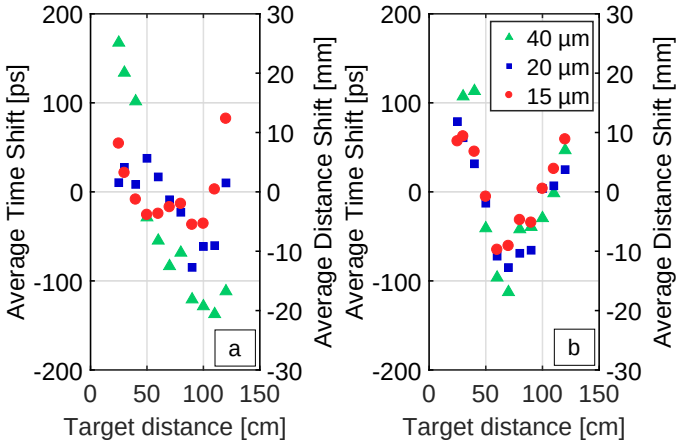

Figure 5.13: *Average time and distance shift as a function of target distance. a)* 0 lx, *b)* 300 lx.

ing an optical band pass filter centred on the wavelength of the laser diode is thus possible to strongly reduce the ambient light intensity with a minimal loss of laser optical power.

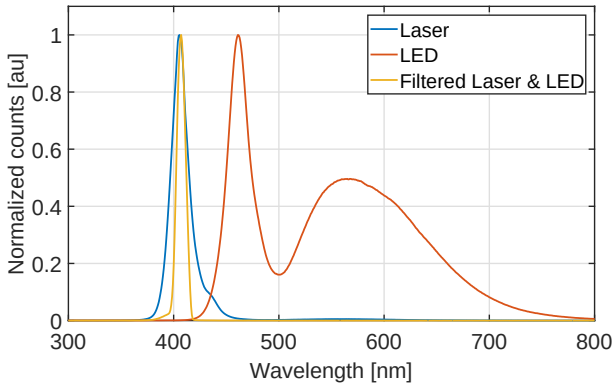

Figure 5.14: *Spectra of Laser and white LED compared to the filtered spectra.*

In Fig. 5.15, the probability of detection for the $40\,\mu\mathrm{m}$ cell-sized SiPM is reported to compare the acquisition with and without the optical band pass filter. Without the filter the effect of ambient light is evident: increasing the illuminance to $300\,\mathrm{lx}$ the probability of detection is severely reduced (cyan triangles) while in the absence of ambient light the range of measured distances extends almost up to $120\,\mathrm{cm}$ with a probability of detection closer to the $100\,\%$ (green triangles).

By placing the optical band pass filter in front of the receiver, the probability of detection is slightly reduced if compared to the acquisition without the filter in the absence of ambient light. This reduction is a consequence of the attenuation of the laser pulse caused by the optical filter ($95\,\%$ of transmission).

With the optical filter mounted, the effect of ambient light is no more evident as can be observed considering the circle data points. Increasing the illuminance up to $1.1\,\mathrm{klx}$ (the maximum level of our setup) there are no evident differences with the measurements performed in the dark. The effect of ambient light is thus effectively suppressed by the optical filter.

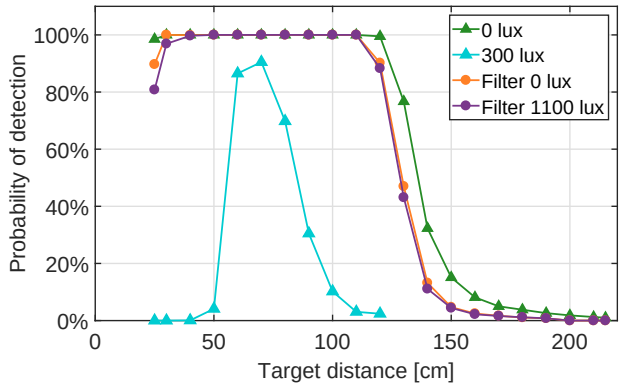

Figure 5.15: *Probability of detection as a function of target distance for the* $40\,\mu\mathrm{m}$ *cell-sized SiPM with and without optical band pass filter.*

5.4 Portable ToF range meter with high-energy short-pulse laser diode

The measurement range obtained in the experimental ToF setup presented in the previous sections, and thus its applicability, is mainly limited by the low power of the emitter used in the investigation. A larger range can be enabled by alternative emitters, such as the one described in [6].

Another factor limiting the applicability of the presented system is the wavelength used, $405\,\mathrm{nm}$, that is not suitable for several applications where people are exposed to the emitted light. For these applications, invisible NIR light is required. The use of IR emitters requires a detector with optimized efficiency in this spectral region, while the NUV-HD SiPMs used in the measurement reported in the previous section exhibit a PDE in the order of $35\,\%$ at $405\,\mathrm{nm}$, with an efficiency at $810\,\mathrm{nm}$ lower than $10\,\%$.

FBK has been recently developing NIR-HD SiPMs with an enhanced PDE in the NIR spectra by implementing several technological and design improvements in order to effectively extend the depth of the collection region of generated carriers up to several microns, thus increasing the PDE of NIR photons [7].

In order to evaluate the feasibility of a SiPM-based range meter in the NIR region, a collaboration with the Circuits and Systems Research Unit of the ITEE Faculty of the University of Oulu was established to operate with a GaAs/AlGaAs multiple quantum well laser diode with with a spectral emission of $\sim 0.808\,\mu\mathrm{m}$ as transmitter and the NIR-HD SiPM designed in FBK as receiver.

The research activity reported in this chapter was carried out from May to July 2018 at the Circuits and Systems Research Unit of the ITEE Faculty of the University of Oulu, Finland, under the supervision of Professor J. Kostamovaara and L. Hallman.

5.4.1 Experimental setup

From a working-principle point of view the experimental setup used for the measurements in the NIR range is based on the same building blocks of the experimental setup used for the preliminary measurements described in 5.2.

The difference with respect to the preliminary measurement setup consists in the replacement of the commercial $405\,\mathrm{nm}$ laser emitter (Transmitter) with a high-energy short-pulse multiple quantum well laser diode emitting at $810\,\mathrm{nm}$, while the Time Correlated Single Photon Counter (TCSPC) measurement system was replaced by an FPGA-based TDC. In order to better match the laser emission with a detector having greater efficiency in the NIR spectral region, newly development FBK NIR-HD SiPMs were employed for the ToF receiver.

Receiver

SiPMs with two different cell-size with a Photon Detection Efficiency enhanced in the NIR region, developed at the FBK, were employed as receivers.

Starting from the RGB-HD technology, the NIR-HD (Near Infra-Red) SiPMs were designed by increasing the thickness of the epitaxial layer till $\sim 8\,\mu\mathrm{m}$ in order to extend the collection depth for NIR photons. This technological improvement is effective to enhance the PDE in the NIR spectrum, although the simultaneous increase of the lateral depletion from the trenches causes a border effect that limits the effective fill

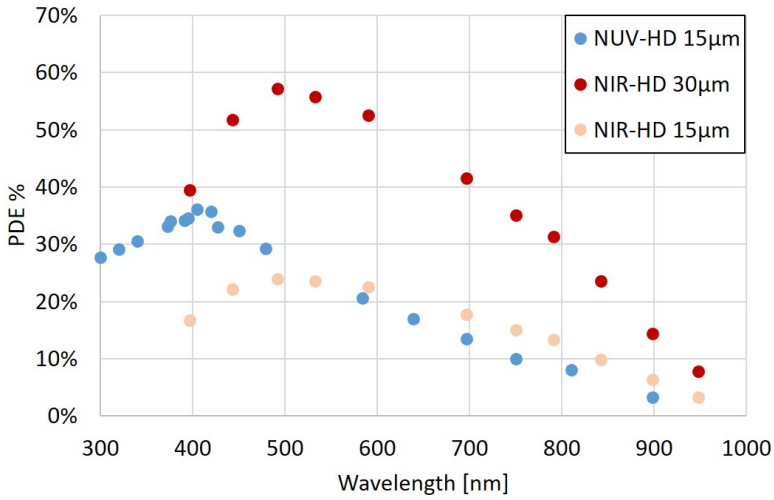

Figure 5.16: *Comparison of the Photon Detection Efficiency of two different NIR-HD and a NUV-HD SiPMs designed and developed at FBK (NUV-HD OV=8V, NIR-HD* $30\,\mu m$ *OV=8V, NIR-HD* $15\,\mu m$ *OV=10V).*

factor [7].

As described in 5.2.1, the SiPMs are connected to an amplifier board with a pole-zero compensation stage [149] in order to convert the current output of the SiPM to a sharp voltage pulse, thus achieving a fast baseline recovery.

In Fig.5.16, the PDE of the two different cell-sized NIR-HD SiPMs is reported at 8V overvoltage together with the PDE of a NUV-HD at the same overvoltage for comparison. In this operation condition the PDE at $810\,nm$ is $25\,\%$ and $12\,\%$ respectively for the $30\,\mu m$ and $15\,\mu m$ cell-sized SiPMs.

Transmitter

The Laser emitter is a GaAs/AlGaAs multiple quantum well laser diode designed and development at the Circuits and Systems Research Unit of the ITEE Faculty of the University of Oulu. This laser diode features an asymmetric waveguide structure composed of a $30\,\mu m$ stripe width and

a $3\,\mathrm{mm}$ cavity length with a spectral emission of $\sim 0.808\,\mu\mathrm{m}$ working in single transversal mode and a large equivalent spot size of $\sim 3\,\mu\mathrm{m}$.

The laser diode is mounted on a ceramic sub-mount that can be connected to the driver board without the need of any heat sink, a feature that perfectly suits the need of integrating the laser driver in a compact system. In Fig. 5.17, the picture of the laser diode on its ceramic sub-mount connected to the laser driver PCB is reported.

When crossed by with current pulses of $\sim 1\,\mathrm{ns}$ with an amplitude lower than $10\,\mathrm{A}$ the laser diode is able to generate short light pulses with a width in the order of $100\,\mathrm{ps}$ (FWHM) and high energy ($\sim 1\,\mathrm{nJ}$) [153].

The core of the driver is a laser switch with 6 channels, that is able to generate fast current pulses when connected to an input pulse signal. Each of the 6 channels connected in parallel can provide up to $1.5\,\mathrm{A}$ current pulses to the laser diode.

At the experimental condition used in the measurement that are reported in this dissertation, the laser driver generated $180\,\mathrm{ps}$ (FWHM) pulses with $1.75\,\mathrm{nJ}$ energy with an input pulse of $600\,\mathrm{mV}$ amplitude and $2\,\mathrm{ns}$ FWHM pulse width. In order to be able to detect the extended distance range as a consequence of the higher energy of the laser with respect to the measurement performed in the previous sections, the repetition rate was set to $1\,\mathrm{MHz}$.

Optics

In Fig.5.18, the experimental setup is reported. Both receiver and laser emitter were mounted on a 3D stage, needed for a fine alignment. In the foreground, the optics block can be seen. The distance measurements were performed on a hallway by measuring a target placed at different distances.

The optics setup block is the same as reported in [6]: it is composed of two lenses of $30\,\mathrm{mm}$ and $20\,\mathrm{mm}$ focal length respectively for the laser emitter and the SiPM receiver. An optical interference filter centred on the laser emission was used to reduce the ambient light detection.

Since the optics was not optimized for the SiPM receiver, the Field

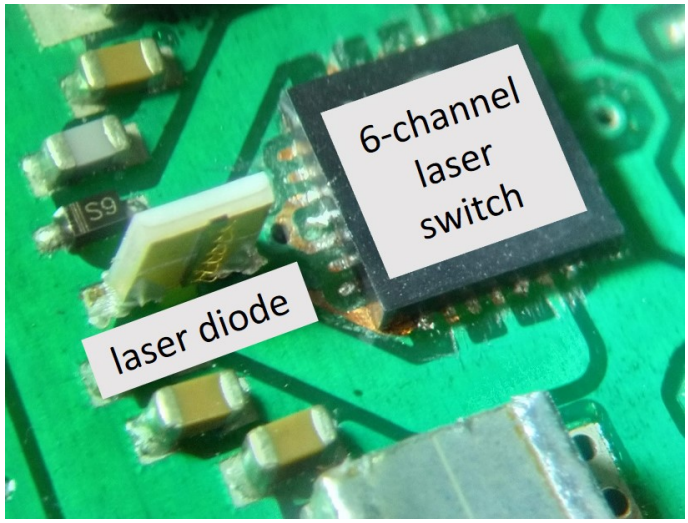

Figure 5.17: *Picture of the laser diode on its ceramic sub-mount connected to the laser driver realized with a 6-channel laser switch.*

Of View (FOV) of the receiver is not correctly matched with the FOV of the laser emitter, meaning that only a portion of the target acquired by the SiPM is covered by the laser spot.

Acquisition system

In order to evaluate the possibility to design a compact ToF range meter and to be able to perform the the ToF measurement with a portable system, a low-cost FPGA-Based TDC as described in [146] was used as acquisition system, replacing the TCSPC module.

The time delay between the start and stop signal can be measured with a simple counter, counting the number of periods of a reference clock between the two signals, but the resolution of this technique is limited by the clock period itself. For low-cost devices the clock period is in the order of few nanoseconds, a resolution that is not acceptable in many ToF systems. To achieve a better resolution a fast tapped delay line can be implemented in the FPGA. The input signal is fed trough the delay line, whose state is latched at the arrival of the stop signal.

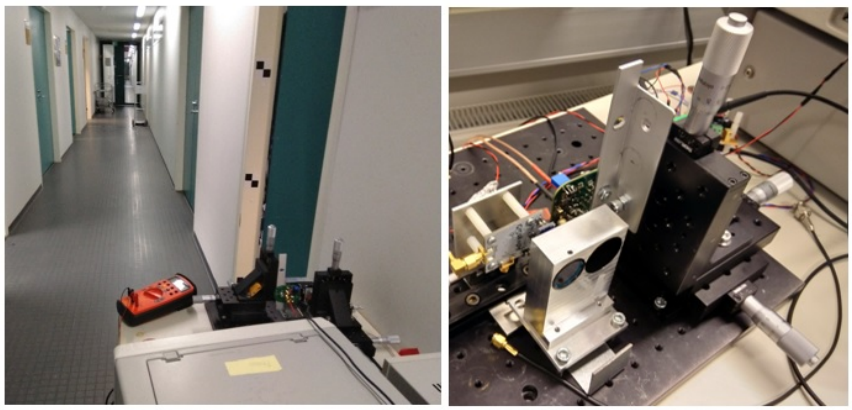

Figure 5.18: *Experimental setup. (Left) Picture of the hallway where the measurements were performed. (Right) In the foreground, optics block composed of two lenses of* $30\,\mathrm{mm}$ *and* $20\,\mathrm{mm}$ *focal length respectively for the laser emitter and the SiPM receiver and an optical interference filter to reduce the ambient light detection. In the background, receiver and laser emitter mounted on 3D stages for a fine alignment.*

The TDC used in this work is based on the Nutt interpolation method that combines the delay lines with a counter to extend the maximum measurable time range.

In Fig. 5.19, a timing diagram of the TDC illustrating its working principle is reported. A clock counter activated by the input signal counts the n clock cycles between the start and stop signal, performing a coarse measurement. The acquisition is then refined by measuring the time stamps of the start and stop signals, sampling the two different delay lines to obtain ΔT_1 and ΔT_2. The overall time interval is thus expressed by the following equation:

$$\Delta T = \Delta T_1 + n \times T_{clk} - \Delta T_2 \tag{5.2}$$

with T_{clk} referring to the clock period of the FPGA.

The TDC, implemented with a low-cost Spartan 6 FPGA, features a resolution (LSB value) of $25.57\,\mathrm{ps}$ and a Single Shot Precision between $0.69 \div 1.46$ LSB. The architecture of the TDC is described in detail in [146].

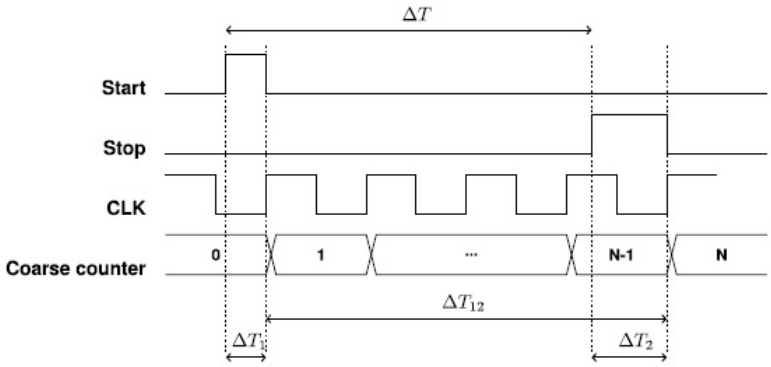

Figure 5.19: *Timing diagram of the TDC, illustrating its working principle [146].*

A user interface was developed in Matlab to set up and control the acquisition. The histogram of the time of arrivals of the detected photons is fitted during the measurement to provide an in-line monitoring of the FWHM.

5.4.2 Preliminary measurement

Before using the NIR SiPMs in the ToF distance measurement setup, the optimal overvoltage was experimentally evaluated.

The threshold voltage for the FPGA-based acquisition system was set at 1.5 SiPM-cell amplitude in all the measurement reported hereafter.

Fig.5.20 shows the probability of detection as a function of distance and overvoltage for the $30\,\mu\mathrm{m}$ cell-size NIR-HD SiPM with a $4\,\%$ reflectivity target at $300\,\mathrm{lx}$ of ambient light.

At low overvoltages ($2\,\mathrm{V}$ and $4\,\mathrm{V}$), the low PDE of the SiPM receiver strongly decreases the probability of detection after few meters. At the highest overvoltage reported in Fig. 5.20, $10\,\mathrm{V}$, the results obtained for distances lower than $6\,\mathrm{m}$ are the same as the ones obtained at $8\,\mathrm{V}$, while at higher distances (from 7 up to 12 meters) the system acquires false detection events due to increased correlated noise. According to the results of these measurement, the characterization campaign reported in this section was performed by applying $8\,\mathrm{V}$ of overvoltage at the $30\,\mu\mathrm{m}$

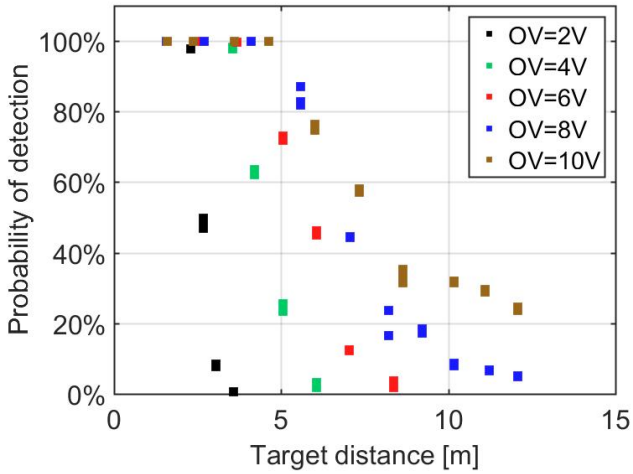

Figure 5.20: *Evaluation of the overvoltage on the probability of detection. Measurement performed at 300 lux of ambient light with a* $4\,\%$ *reflectivity target employing a NIR-HD SiPM with* $30\,\mu\mathrm{m}$ *cell-size.*

cell-size NIR-HD SiPM, while the $15\,\mu\mathrm{m}$ cell-size NIR-HD SiPM was biased at $10\,\mathrm{V}$ of overvoltage thanks to its lower correlated noise.

5.4.3 Target reflectivity

In the previous section, the probability of detection was evaluated using a $4\,\%$ reflectivity target in order to investigate the effect of overvoltage in the probability of detection within a small distance range from 2 to 12 meters.

In this section the effect of the reflectivity of the target on the range detection performance was evaluated using the $30\,\mu\mathrm{m}$ receiver. The measurements were performed in a hallway at indoor light illuminance ($300\,\mathrm{lx}$) by acquiring the laser signal reflected by a moving target with three different reflectivity: $100\,\%$, $10\,\%$ and $4\,\%$.

In Fig. 5.21, the probability of detection is reported as a function of the target distance. The distance range at which the probability of detection is greater than the $90\,\%$ decreases from 40 meters for the $100\,\%$ reflectivity target to 23 meters for the $10\,\%$ target down to 6 meters for

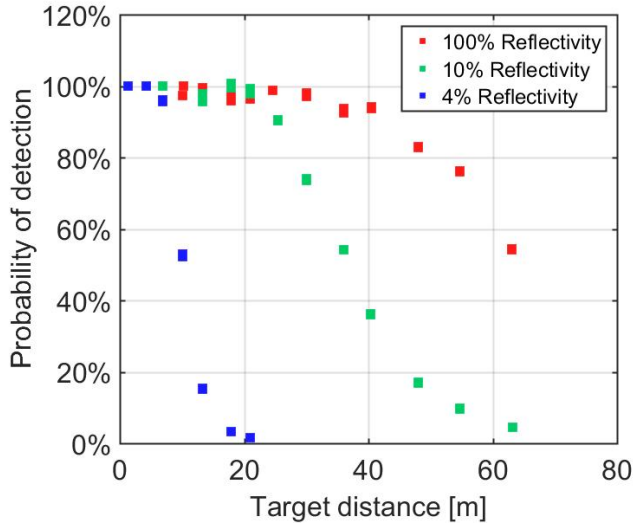

Figure 5.21: *Probability of detection as a function of the target distance for three different targets having* $100\,\%$*,* $10\,\%$ *and* $4\,\%$ *reflectivity at* $300\,\mathrm{lx}$*. The maximum target distance range was limited by the length of the hallway where the measurement were performed.*

the target with $4\,\%$ of reflectivity.

The precision and accuracy of this measurement were evaluated from the Gaussian fit of the time delay histograms. The results of this analysis are reported in Fig. 5.22.

The timing precision at very short distance is almost the same for the three targets, while at large distance a higher target reflectivity obviously leads to a better precision. If restricted to the region where the detection probability is larger than $90\,\%$, for each target both precision and average time shift are in the same range. For the $100\,\%$ reflectivity target placed at 64 meters from the receiver a precision of $240\,\mathrm{ps}$ was measured, corresponding to a distance precision of $36\,\mathrm{mm}$.

5.4.4 SiPM comparison

The $10\,\%$ reflectivity target was used to compare the performance of NIR-SiPMs with different cell size.

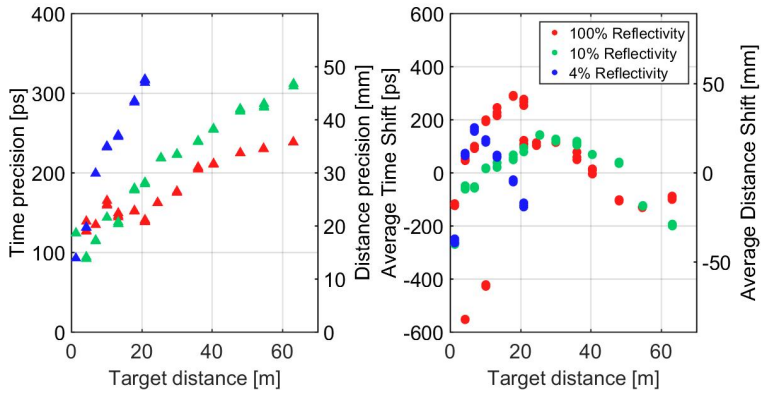

Figure 5.22: *Time precision (left) and average time shift (right) as a function of the target distance for three different target respectively with* $100\,\%$*,* $10\,\%$ *and* $4\,\%$ *reflectivity at* $300\,\mathrm{lx}$*.*

The $10\,\%$ reflectivity target was chosen to make the comparison in an intermediate operating environment, since the $4\,\%$ and $100\,\%$ reflectivity targets feature both extreme conditions of detection.

The $30\,\mu\mathrm{m}$ cell-size SiPM was biased at $8\,\mathrm{V}$ of overvoltage while the $15\,\mu\mathrm{m}$ cell-size SiPM was biased at $10\,\mathrm{V}$. The $15\,\mu\mathrm{m}$ cell-size SiPM was biased at higher overvoltage since its lower gain causes lower correlated noise. The measurement was taken in a hallway with $300\,\mathrm{lx}$ of illuminance.

In Fig. 5.23, the probability of detection is reported for both SiPMs. The range of distances at which the probability of detection is higher than $90\,\%$ extends until 20 meters and 16 meters respectively for the $30\,\mu\mathrm{m}$ and $15\,\mu\mathrm{m}$ cell-size SiPMs. These results can be explained with the different PDE of the two SiPMs.

As shown in Fig 5.24, within the respective measurement ranges, timing precision and worst-case time shift have similar values for both detectors.

For the $30\,\mu\mathrm{m}$ cell-size SiPM the maximum distance of 64 meter was acquired with a time precision lower than $300\,\mathrm{ps}$ corresponding to a distance precision below $45\,\mathrm{mm}$. The accuracy of detection settles in the range of $200\,\mathrm{ps}$ corresponding to a distance precision lower than

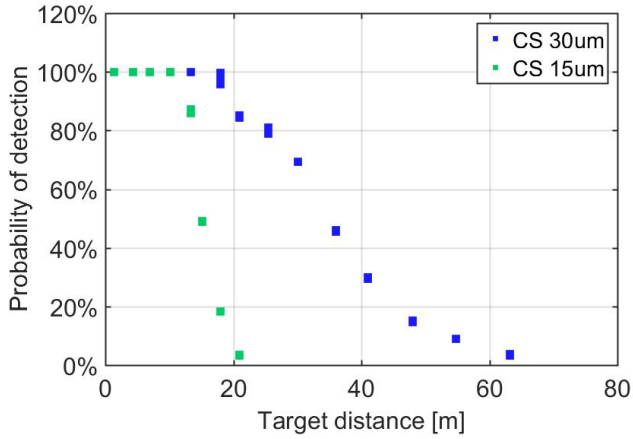

Figure 5.23: *Probability of detection as a function of the target distance for the two different cell-sized NIR-HD SiPMs (*30 *and* 15 µm*) performed on a* 10 % *reflectivity target with* 300 lx *ambient light illuminance.*

25 mm.

Differently from the preliminary measurement reported in section 5.3, in the absence of a controlled source of ambient light, it was not possible to compare the two NIR SiPMs at different values of environmental illuminance.

5.5 Conclusions

The results presented in this chapter are mainly intended to provide some guidelines for optimizing the operating conditions of a SiPM in a Time-of-Flight system.

In section 5.3, a comparison between three different NUV-HD SiPMs used as detectors in a Time-of-Flight system is reported in terms of ambient light rejection and distance range measurement performance. The different types of SiPM analysed in section 5.3 have the same active area but differ in the cell size.

A first set of measurement were performed on a fixed target maintaining a constant amount of reflected laser light while changing the ambient light illuminance. The larger cell-size device exhibits the worst

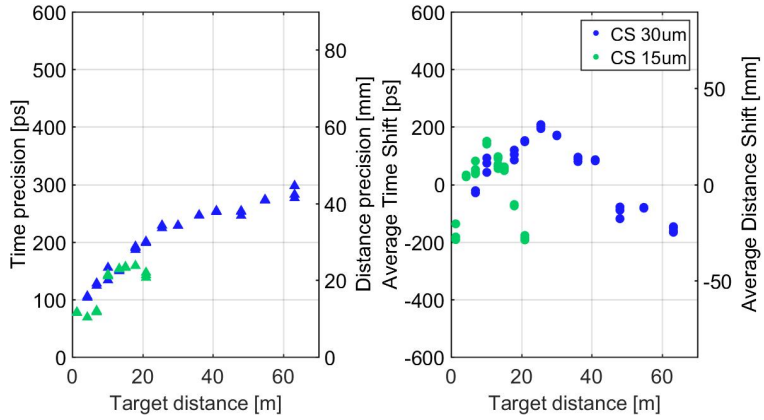

Figure 5.24: *Comparison of the time precision (left) and average time shift (right) as a function of the target distance for the two different cell-sized NIR-HD SiPMs (*30 *and* $15\,\mu\mathrm{m}$*) measured with a* $10\,\%$ *reflectivity target at* $300\,\mathrm{lx}$.

laser pulse detection probability, the worst time precision and higher average time shift. The $15\,\mu\mathrm{m}$ cell-size device presents the best performance in all the considered range of ambient light illuminance, with a single-shot time precision better than $34\,\mathrm{mm}$ at $1.1\,\mathrm{klx}$ at $10\,\mathrm{MHz}$ repetition rate.

The evaluation of the acquisition performance as a function of target distance showed that the better sensitivity of the $40\,\mu\mathrm{m}$ cell-size device leads to a larger measurement range at $0\,\mathrm{lx}$ if compared to smaller cell-size devices. However, the ranging performance is reduced as the ambient light illuminance increases due to the lower ambient light rejection of the larger cell-size devices. The smaller cell-size SiPM has superior performance both with respect to random and to systematic distance measurement errors in the all range of illuminances that can be obtained with the current system.

To evaluate the feasibility of a SiPM-based range meter in the NIR region, the measured distance range of the SiPM-based ToF system was extended up to a few tens of meter by using a short-pulse ($180\,\mathrm{ps}$ FWHM) high-energy ($1.75\,\mathrm{nJ}$) GaAs/AlGaAs multiple quantum well laser diode with a spectral emission of $\sim 0.808\,\mu\mathrm{m}$ [6], combined with

NIR-HD SiPMs with an enhanced efficiency for NIR photons recently developed at FBK [7].

A measurement campaign was performed on targets with different reflectivity in order to investigate the ability of the detection system to operate in a realistic scenario with different target characteristics. Targets with good reflectivity can be detected up to 64 meters with a detection probability of $54\,\%$, a precision of $240\,\mathrm{ps}$ and an accuracy of $100\,\mathrm{ps}$ corresponding respectively to a distance precision of $36\,\mathrm{mm}$ and an average distance shift of $15\,\mathrm{mm}$, while in the worst case scenario measurement performed with a $4\,\%$ reflectivity target its distance was detected up to 10 meters with a detection probability of $53\,\%$, an accuracy of $250\,\mathrm{ps}$ and a precision of $230\,\mathrm{ps}$.

With proper ambient light noise filtering, achieved by placing an optical interference filter centred on the laser emission, and considering a low ambient light illuminance of $300\,\mathrm{lx}$, the $30\,\mu\mathrm{m}$ cell-size NIR-HD SiPM features a larger distance range of detection compared to the $15\,\mu\mathrm{m}$ NIR-HD cell-size SiPM due to its higher PDE.

The replacement of the TCSPC module with an FPGA-based TDC represents a good opportunity to integrate the system in a low-cost prototype. In perspective, a portable prototype can be obtained thanks to the low power consumption of the device: $33\,\mathrm{mA}$ at $12\,\mathrm{V}$ for the transmitter driver, $80\,\mathrm{mA}$ at $5\,\mathrm{V}$ for the SiPM-based receiver and $75\,\mathrm{mA}$ at $3.3\,\mathrm{V}$ for the acquisition system.

The high repetition rate (MHz range) was successfully managed by both laser driver and acquisition system: the proposed system could thus be upgraded by including a 2-axis scanning mirror to perform real-time imaging [8].

CHAPTER 6

Conclusions and Future Perspectives

In this dissertation two different applications of Geiger-Mode Avalanche Photo Diode arrays have been reported: a two-tier GM-APD array with in-pixel coincidence for particle tracking and a direct Time-of-Flight range meter with a SiPM-based receiver.

The two-tier particle detector, which was developed in the framework of ApiX2 and ASAP projects funded by Istituto Nazionale di Fisica Nucleare (INFN), has been characterized both from the electrical and from the functional points of view.

The use of GM-APDs in coincidence has already been proposed to discriminate a particle tracking event from a dark event in order to overcome the DCR issue of GM-APDs that has prevented their use as particle tracking detectors. In the ApiX prototype, fabricated in a standard $150\,\mathrm{nm}$ CMOS process, the detection in coincidence is performed at the pixel level by implementing a dedicated in-pixel electronics ensuring a

strong DCR reduction with respect to each single layer. Thanks to this feature, if a time resolution of $0.75\,\mathrm{ns}$ is selected, the mean dark count rate can be reduced to $93\,\mathrm{mHz}$ per pixel, that is five order of magnitude lower than the mean DCR of each layer (few kHz).

A dedicated experimental setup composed of an interface board and a microcontroller was made to evaluate the functionality of the device. A complete characterization campaign was performed and results in terms of breakdown voltage uniformity, DCR distribution and optical crosstalk were reported.

The intra-array breakdown voltage variability is lower with respect to the variation between different dies. The uniformity among detectors of the same type is very good, with a standard deviation lower than $20\,\mathrm{mV}$ and a peak-to-peak variation in the order of $100\,\mathrm{mV}$. The variation of the breakdown voltage between the same detectors on different dies is larger: Type 1 devices exhibit a maximum spread of about $1\,\mathrm{V}$, while in Type 2 devices the variation is lower, about $350\,\mathrm{mV}$. The DCR of devices of the same type spans several orders of magnitude, a typical behaviour that has been observed in different processes. The DCR distribution between different dies has a good uniformity. The median DCR is in the order of $3\,\mathrm{kHz}$ for both device types at $3.3\,\mathrm{V}$ excess bias, while the best detectors in the distribution exhibit a DCR in the order of $300\,\mathrm{Hz}$. The best DCR corresponds to $0.15\,\mathrm{Hz}\,\mu\mathrm{m}^{-2}$ that is a rate comparable with commercial SiPM cells of the same size, while the median DCR is an order of magnitude larger than typical SiPMs ($1.5\,\mathrm{Hz}\,\mu\mathrm{m}^{-2}$). This higher DCR is a consequence of the standard CMOS process adopted for the fabrication of the devices that has no dedicated processing gettering steps.

While optical crosstalk in GM-APD arrays have often been performed through pseudo-crosstalk measurements, the coincidence detection electronics included in the APiX prototype represented a good opportunity to perform direct measurement of intra-tier crosstalk in single-layer devices and inter-layer crosstalk in vertically-integrated devices. Differences in the structures between the two types of detectors lead to different values of crosstalk coefficient. Type 2 devices exhibit higher value of crosstalk coefficient compared to Type 1 detector. This higher

value is a consequence of the higher active volume and higher junction depth of Type 2 detectors. In order to test the possibility of obtaining a low material budget, as required in modern colliders, the original $280\,\mu\mathrm{m}$ substrate thickness of the dies was reduced to $50\,\mu\mathrm{m}$ and $25\,\mu\mathrm{m}$. This substrate reduction, successfully performed without compromising the detectors functionality, allowed the evaluation of the role of substrate thickness on the optical crosstalk. In thicker devices the crosstalk dependence on detector distance shows a secondary peak due to the onset of total internal reflection at the bottom surface of the device, while in thinner samples the substrate acts like a 2D wave guide. Considering the global effect of crosstalk when all the pixels in the array are enabled, a severe increase of the DCR distribution was shown, an increase that is more pronounced with a lower substrate thickness. Optical crosstalk measurements on vertically-aligned unshielded pixels reported a different coefficient between Type 1 and Type 2 devices. The higher crosstalk coefficient for Type 2 detectors can be explained considering their higher photon detection efficiency at the spectral wavelengths of secondary photons and the avalanche triggering probability that increases more sharply with excess bias. The results of the optical crosstalk characterization confirmed the importance to implement proper strategies to limit its effect, especially in the design of efficient high-density SPAD arrays if the backside needs to be thinned. Deep trenches should be implemented to reduce the direct optical crosstalk, while the implementation of a heavily doped layer or the texturing of the chip backside should be considered to avoid waveguide propagation.

The functional characterization of the APiX prototype with a β-source was reported and an evaluation of the radiation hardness of the devices was discussed.

A set of measurement with a ^{90}Sr β source was performed to demonstrate the particle detection ability of the APiX prototype. The experimentally measured count rate of $33\,\mathrm{mHz}$ per pixel, corresponding to $8.8\,\mathrm{Hz}\,\mu\mathrm{m}^{-2}$, is in good agreement with the expected particle-induced count rate predicted by Monte Carlo simulations. Small difference between the measured rate and the predicted rate can be attributed to uncertainties within the MC simulation. In particular, the geometrical fill

factor for charged particles could be higher with respect to the optically measured one; an experimentally confirmation of this hypothesis should be performed on the APiX prototype with a nearly orthogonal incidence particle beam.

An irradiation campaign with neutrons was performed at the INFN Laboratori Nazionali di Legnaro (LNL) in order to evaluate the radiation tolerance of the detectors. Five devices were irradiated with different fluences from a minimum of $10^9 n\ cm^{-2}$ up to a maximum fluence of $3 \times 10^{11} n\ cm^{-2}$. The mean DCR as a function of the neutron fluence exhibits a linear dependence with the fluence up to $10^{11} n\ cm^{-2}$, as expected for neutron radiation, while a loss of linearity was observed at the highest fluence as a consequence of the DCR saturation due to the detector dead-time. Radiation levels evaluated in this irradiation campaign are relatively moderate with respect to the harsh environment of future linear colliders[133]. Even in the presence of a moderate fluence, the devices did not showed an adequate radiation hardness, with a detrimental increase in the DCR. This characterization provided anyway useful indications for possible applications of this detector concept. This configuration could be successfully employed as beta prober for guided microsurgery with beta-trackers, while the integration of more than two layers in a multi-stack configuration can further reduce the DCR, extending in this way the ability of the coincidence detectors to operate in higher levels of radiation than the ones evaluated in this dissertation.

While the irradiation of samples with neutrons was performed without biasing the detectors during the irradiation and performing the functional characterization off-line shortly after the irradiation, an on-line measurement of a proton micro-beam was also carried out on single layer devices. As the micro-beam was switched on, an increase of the count rate comparable with the expected proton rate was successfully detected. As the dose increased with the beam on, the DCR increased in steps due to creation of defects in the active region. A similar step-shaped increase of DCR with the radiation dose in silicon GM-APDs detectors, due to the generation of clusters of defects, was already reported in literature[132].

The electrical and functional characterization of APiX prototype provided useful guidelines for the optimization of a novel prototype designed within the ASAP project, by implementing technological improvements to increase system performance in terms of efficiency and dark count reduction. Only Type 1 detectors were integrated in the new prototype since they exhibited a lower crosstalk coefficient, while the other characteristics were similar to Type 2 detectors. In the new prototype, the pixel pitch was increased to achieve a better Fill Factor and the array dimensions were extended to $3.6 \times 3.6\,\mathrm{mm}^2$ in order to perform beam measurements with better statistics[111].

SiPMs take advantage of the characteristics of GM-APDs such as high sensitivity, high efficiency and very low time jitter, and allow the simultaneous detection of multiple photons thanks to the connection of several sensitive elements in parallel [5]. These features make SiPMs ideal detectors for direct Time-of-Flight range meters.

The results of an evaluation campaign of measurements using different types of Silicon PhotoMultipliers (SiPMs) designed and fabricated at the Fondazione Bruno Kessler (FBK) used as receiver for a direct Time-of-Flight (ToF) range meter was reported.

A first set of measurement with NUV-HD SiPMs were performed on a fixed target maintaining a constant amount of reflected laser light while changing the ambient light illuminance. The larger cell-size device exhibits the worst laser pulse detection probability, the worst time precision and the highest average time shift. The $15\,\mu\mathrm{m}$ cell-size device presents the best performance in all the considered range of ambient light illuminance, with a single-shot time precision better than $34\,\mathrm{mm}$ at $1.1\,\mathrm{klx}$ at $10\,\mathrm{MHz}$ repetition rate.

The characterization of the SiPMs in a range-meter setup showed that, thanks to its higher PDE, the $40\,\mu\mathrm{m}$ cell-size device offers a larger measurement range at $0\,\mathrm{lx}$ ambient light if compared to smaller cell-size devices. However, its ranging performance is reduced as the ambient light illuminance increases due to the lower ambient light rejection of the larger cell-size devices. The smaller cell-size SiPM has superior performance both with respect to random and to systematic distance measurement errors in the all range of illuminances that could be ob-

tained with the current system.

In order to evaluate the feasibility of a SiPM-based range meter in the NIR region, a collaboration with the Circuits and Systems Research Unit of the ITEE Faculty of the University of Oulu was established. A measurement setup was realized using a GaAs/AlGaAs multiple quantum well laser diode with with a spectral emission of $\sim 0.808\,\mu\mathrm{m}$ as transmitter and FBK recently developed NIR-HD SiPMs, with an enhanced PDE in the NIR spectra, as receivers.

A measurement campaign was performed on targets with different reflectivity in order to investigate the ability of the detection system to operate in a realistic scenario with different target characteristics. Targets with good reflectivity can be detected up to $64\,\mathrm{m}$ with a detection probability of $54\,\%$, a precision of $240\,\mathrm{ps}$ and an accuracy of $100\,\mathrm{ps}$ corresponding respectively to a distance precision of $36\,\mathrm{mm}$ and an average distance shift of $15\,\mathrm{mm}$, while in the worst case scenario, obtained using a $4\,\%$ reflectivity target, the detection probability was $53\,\%$ at $10\,\mathrm{m}$, with an accuracy of $250\,\mathrm{ps}$ and a precision of $230\,\mathrm{ps}$.

While the preliminary measurements with NUV-HD SiPM receiver were performed with a Time Correlated Single Photon Counting module, the NIR measurement were successfully acquired using an FPGA module. By replacing the TCSPC module with an FPGA-based TDC it was possible to integrate a compact low-cost prototype. In perspective, a portable prototype can be obtained thanks to the low power consumption of the device: $33\,\mathrm{mA}$ at $12\,\mathrm{V}$ for the transmitter driver, $80\,\mathrm{mA}$ at $5\,\mathrm{V}$ for the SiPM-based receiver and $75\,\mathrm{mA}$ at $3.3\,\mathrm{V}$ for the acquisition system.

In addition, the high repetition rate (MHz range) successfully managed by both laser driver and acquisition system, makes the proposed system suitable to be upgraded by including a 2-axis scanning mirror to perform real-time imaging [8].

List of Figures

1.1 IV curve of a diode. 2
1.2 Representation of the five constitutive phases of the avalanche process. 4
1.3 Semplified model of the SPAD. 5
1.4 GM-APD pixel with generic CMOS front-end electronic. 6
1.5 Cross-sections of a cell of a p-on-n SiPM (left) and a cell of a n-on-p SiPM (right). 8
1.6 SiPM output acquired with an oscilloscope in persistance mode. 8
1.7 Temperature dependence of dark currents for the different generation mechanisms. 11
1.8 (a) Schematic representation of DCR dependence on temperature. (b) Example of DCR measurement as a function of temperature. 13
1.9 Effect of the three factor composing the PDE. 16
1.10 Photo renspose of a CMOS SPAD array for 3D imaging. 18
1.11 Excess bias dependence of SPTR of a $1\times1\,\mathrm{mm}^2$ SiPM at $\lambda = 425\,\mathrm{nm}$ and $\lambda = 850\,\mathrm{nm}$. 20

1.12 Block diagram of the 512-channel per-pixel Time-to-Digital Converter implemented in a 4×128 SPAD array. 23
1.13 Schematic representation of the time-resolved spectroscopy. 23
1.14 Micrograph of the SPAD linear array for the Raman spectroscopy. 24
1.15 3D representation of the time resolved measurement. . . 25
1.16 Block diagram of the line sensor with the integrated electronics. 26
1.17 Pixel building block with the simplified DAMAC. 27
1.18 3D imager receiver chip based on a 9×9 SPAD array. . . 28
1.19 3D Time-of-Flight image acquired with 30k points. . . . 29

2.1 Absorption depth in silicon with respect to photon wavelength. 34
2.2 Photon absorption probability for $300\,\mu\mathrm{m}$ silicon as a function of the photon energy. 35
2.3 Depletion voltage and absolute effective doping variations with respect to the normalized fluence. 37
2.4 Detection of short-lived particle decay track acquired by three double-sided microstrip detectors. 38
2.5 First experimental setup of coincidence detection with SiPMs 40
2.6 Basic working principle of the coincidence detection of the APiX prototype pixel. 41
2.7 Cross section of the two different types of detector integrated in the APiX prototype. 42
2.8 Micrograph of the bottom chip. 44
2.9 Block diagram of in-pixel electronics. 45
2.10 Simplified timing diagram showing the effect of monostable pulse width on fake coincidence events. 46
2.11 Schematic representation of the vertically-integrated particle detector prototype. 48

3.1 Block diagram of the experimental setup. 50
3.2 (Left) PGA100 package for bottom chips and vertically-integrated devices. (Right) JLCC44 package for top chips. 51

3.3 Timing diagram of the enable register loading. 54
3.4 Enable configuration patterns that can be selected. 55
3.5 Timing diagram of the data readout signals. 56
3.6 Example of DCR vs. bias voltage curve. 57
3.7 Uniformity of the breakdown voltage measured on 5 dies. 58
3.8 2D map of the dark counts for Type 1 detectors at an excess voltage of 1V at 20°C. 59
3.9 DCR cumulative distributions. 60
3.10 DCR distributions for Type 1 detectors at an excess voltage of $1\,\mathrm{V}$ from $-30\,^{\circ}\mathrm{C}$ to $50\,^{\circ}\mathrm{C}$. 61
3.11 Temperature dependence of dark count rate for three nominally equal detectors. 62
3.12 Crosstalk coefficient as a function of the overvoltage. . . 65
3.13 Crosstalk coefficient 2D map measured on a die with $25\,\mu\mathrm{m}$ tickness at Vex = $3\,\mathrm{V}$. 66
3.14 Crosstalk coefficient as a function of detector distance for a die with $280\,\mu\mathrm{m}$ substrate thickness. 67
3.15 Crosstalk coefficient as a function of detector distance for a die with $50\,\mu\mathrm{m}$ substrate thickness. 67
3.16 Crosstalk coefficient as a function of detector distance for a die with $25\,\mu\mathrm{m}$ substrate thickness. 68
3.17 DCR distributions acquired at 3V (Type 1 devices). . . . 71
3.18 DCR distributions acquired at 3V (Type 2 devices). . . . 72
3.19 DCR distributions of Type 2 devices with $50\,\mu\mathrm{m}$ thickness biased at three different excess voltages. 74
3.20 Crosstalk coefficient as a function of the excess voltage measured on the vertically integrated prototype. 75

4.1 Distribution of the Dark Count Rate in coincidence . . . 79
4.2 Energy distributions of the simulated β particles 81
4.3 Distribution of DCR in coincidence at different excess voltages. 82
4.4 Distribution of DCR in coincidence at three different environmental temperature 83

4.5 Map of the differences pixel-by-pixel between the acquisition in the presence and in the absence of the radioactive source 84
4.6 Coincidence rate distribution in the presence and in the absence of the radioactive source 84
4.7 Histogram of the differences pixel-by-pixel between the acquisition in the presence and in the absence of the radioactive source 85
4.8 Sketch of the irradiation setup 87
4.9 DCR distributions for the Type 1 detectors irradiated at different neutron fluences 88
4.10 DCR distributions for the Type 2 detectors irradiated at different neutron fluences 89
4.11 DCR distributions before and after the annealing procedure 90
4.12 Histograms of the breakdown voltage before and after the irradiation 91
4.13 Mean DCR as a function of the neutron fluence 93
4.14 Experimental setup at the LNL micro-beam 94
4.15 Evaluation of the proton count rate with the SiPM covered with a scintillator layer 95
4.16 Secondary X-ray image of the alignment marker compared with a micrograph of the same area 96
4.17 Output signal of a pixel detector under proton irradiation 97
4.18 Output signal of a pixel detector under proton irradiation 98

5.1 Schematic illustration of the working principle of Time-of-Flight systems. 100
5.2 Block-diagram of the experimental setup. 103
5.3 Breakdown voltage extraction from the single-cell output signal amplitude as a function of bias voltage. 104
5.4 Ambient light count rate as a function of illuminance. . . 108
5.5 Oscilloscope acquisition in persistence mode of the laser triggered output signal of the $15\,\mu\mathrm{m}$ cell-size device . . . 109
5.6 Laser pulse detection probability as a function of ambient light intensity. 109
5.7 Time precision as a function of ambient light intensity. . 110

5.8 Average time shift as a function of ambient light intensity. 110
5.9 Probability of detection as a function of target distance at 0 lx. 112
5.10 Probability of detection as a function of target distance at 300 lx. 113
5.11 Probability of detection as a function of target distance of the 40 µm SiPM at four different ambient light illuminaces. 113
5.12 Single-shot time and distance precision as a function of target distance. a) 0 lx, b) 300 lx. 114
5.13 Average time and distance shift as a function of target distance. a) 0 lx, b) 300 lx. 114
5.14 Spectra of Laser and white LED compared to the filtered spectra. 115
5.15 Probability of detection as a function of target distance for the 40 µm cell-sized SiPM with and without optical band pass filter. 116
5.16 Comparison of the Photon Detection Efficiency of two different NIR-HD and a NUV-HD SiPMs designed and developed at FBK 118
5.17 Picture of the laser diode on its ceramic sub-mount connected to the laser driver realized with a 6-channel laser switch. 120
5.18 Experimental setup. 121
5.19 Timing diagram of the TDC, illustrating its working principl 122
5.20 Evaluation of the overvoltage on the probability of detection 123
5.21 Probability of detection as a function of the target distance for three different targets having 100 %, 10 % and 4 % reflectivity at 300 lx. 124
5.22 Time precision (left) and average time shift (right) as a function of the target distance for three different target respectively with 100 %, 10 % and 4 % reflectivity at 300 lx. 125

5.23 Probability of detection as a function of the target distance for the two different cell-sized NIR-HD SiPMs (30 and 15 µm) performed on a 10 % reflectivity target with 300 lx ambient light illuminance. 126
5.24 Comparison of the time precision (left) and average time shift (right) as a function of the target distance for the two different cell-sized NIR-HD SiPMs (30 and 15 µm) measured with a 10 % reflectivity target at 300 lx. 127

List of Tables

1.1 Minimum detectable signal of different type of photodiodes. 19

2.1 Classification of neutron according to the energy 36

3.1 Coincidence time setting 52
3.2 List of digital input signals. B refers to Bottom chip while T refers to Top chip. 53

4.1 Mean ad median DCR at different values of time resolution 80
4.2 List of the irradiation runs reporting the exposure time, the proton current and neutron fluence. 87

[1] G Casse. Recent developments on silicon detectors. *Nuclear Instruments and Methods in Physics Research Section A: Accelerators, Spectrometers, Detectors and Associated Equipment*, 732:16–20, 2013.

[2] N Savic, L Bergbreiter, J Breuer, A La Rosa, A Macchiolo, R Nisius, and S Terzo. Thin n-in-p planar pixel modules for the atlas upgrade at hl-lhc. *Nuclear Instruments and Methods in Physics Research Section A: Accelerators, Spectrometers, Detectors and Associated Equipment*, 845:154–158, 2017.

[3] M Meschini, GF Dalla Betta, M Boscardin, G Calderini, G Darbo, G Giacomini, ALBERTO Messineo, and S Ronchin. The infn-fbk pixel r&d program for hl-lhc. *Nuclear Instruments and Methods in Physics Research Section A: Accelerators, Spectrometers, Detectors and Associated Equipment*, 831:116–121, 2016.

[4] C Riegel, M Backhaus, JW Van Hoorne, Thanushan Kugathasan, Luciano Musa, Heinz Pernegger, Petra Riedler, D Schaefer, W Snoeys, and W Wagner. Radiation hardness and timing studies of a monolithic towerjazz pixel design for the new atlas inner tracker. *Journal of Instrumentation*, 12(01):C01015, 2017.

[5] P Buzhan, B Dolgoshein, L Filatov, A Ilyin, V Kantzerov, V Kaplin, A Karakash, F Kayumov, S Klemin, E Popova, et al. Silicon Photomultiplier and its possible applications. *Nuclear Instruments and Methods in Physics Research Section A: Accelerators, Spectrometers, Detectors and Associated Equipment*, 504(1-3):48–52, 2003.

[6] Juha Kostamovaara, Jaakko Huikari, Lauri Hallman, Ilkka Nissinen, Jan Nissinen, Harri Rapakko, Eugene Avrutin, and Boris Ryvkin. On Laser Ranging Based on High-Speed/Energy Laser Diode Pulses and Single-Photon Detection Techniques. *IEEE Photonics Journal*, 7(2):1–15, 2015.

[7] Fabio Acerbi, Giovanni Paternoster, Alberto Gola, Nicola Zorzi, and Claudio Piemonte. Silicon photomultipliers and single-photon avalanche diodes with enhanced nir detection efficiency at fbk. *Nuclear Instruments and Methods in Physics Research Section A: Accelerators, Spectrometers, Detectors and Associated Equipment*, 912:309–314, 2018.

[8] François Blais. Review of 20 years of range sensor development. *Journal of electronic imaging*, 13(1):231–244, 2004.

[9] E Charbon. Single-photon imaging in complementary metal oxide semiconductor processes. *Philosophical Transactions of the Royal Society of London A: Mathematical, Physical and Engineering Sciences*, 372(2012):20130100, 2014.

[10] Simon M Sze and Kwok K Ng. *Physics of semiconductor devices*. John wiley & sons, 2006.

[11] Matthew W Fishburn. *Fundamentals of CMOS single-photon avalanche diodes*. fishburn, 2012.

[12] Sergio Cova, M Ghioni, A Lacaita, Carlo Samori, and Franco Zappa. Avalanche photodiodes and quenching circuits for single-photon detection. *Applied optics*, 35(12):1956–1976, 1996.

[13] Alexis Rochas, Alexandre R Pauchard, P-A Besse, Dragan Pantic, Zoran Prijic, and Rade S Popovic. Low-noise silicon avalanche photodiodes fabricated in conventional cmos technologies. *IEEE Transactions on Electron Devices*, 49(3):387–394, 2002.

[14] A Lacaita, M Ghioni, and Sergio Cova. Double epitaxy improves single-photon avalanche diode performance. *Electronics letters*, 25(13):841–843, 1989.

[15] Mohammad Azim Karami, Hyung-June Yoon, and Edoardo Charbon. Single-photon avalanche diodes in sub-100nm standard cmos technologies. In *Proc. Intl. Image Sensor Workshop (IISW)*, number EPFL-CONF-178147, 2011.

[16] Cristiano Niclass, Marek Gersbach, Robert Henderson, Lindsay Grant, and Edoardo Charbon. A single photon avalanche diode implemented in 130-nm cmos technology. *IEEE Journal of selected topics in quantum electronics*, 13(4):863–869, 2007.

[17] Marek Gersbach, Justin Richardson, Eric Mazaleyrat, Stephane Hardillier, Cristiano Niclass, Robert Henderson, Lindsay Grant, and Edoardo Charbon. A low-noise single-photon detector implemented in a 130 nm cmos imaging process. *Solid-State Electronics*, 53(7):803–808, 2009.

[18] Lucio Pancheri and David Stoppa. Low-noise cmos single-photon avalanche diodes with 32 ns dead time. In *Solid State Device Research Conference, 2007. ESSDERC 2007. 37th European*, pages 362–365. IEEE, 2007.

[19] Justin A Richardson, Eric AG Webster, Lindsay A Grant, and Robert K Henderson. Scaleable single-photon avalanche diode structures in nanometer cmos technology. *IEEE Transactions on Electron Devices*, 58(7):2028–2035, 2011.

[20] Eric AG Webster, Justin A Richardson, Lindsay A Grant, David Renshaw, and Robert K Henderson. A single-photon avalanche diode in 90-nm cmos imaging technology with 44% photon detection efficiency at 690 nm. *IEEE Electron Device Lett*, 33(5):694–696, 2012.

[21] Eric AG Webster, Lindsay A Grant, and Robert K Henderson. A high-performance single-photon avalanche diode in 130-nm cmos imaging technology. *IEEE Electron Device Letters*, 33(11):1589–1591, 2012.

[22] Dieter Renker. Geiger-mode avalanche photodiodes, history, properties and problems. *Nuclear Instruments and Methods in Physics Research Section A: Accelerators, Spectrometers, Detectors and Associated Equipment*, 567(1):48–56, 2006.

[23] V. golovin, "patent no. ru 2142175", 1998.

[24] Z. sadygov, "patent no. ru 2102820", 1998.

[25] Gaetano Zappala. *Characterisation of Silicon Photomultipliers for the detection of Near Ultraviolet and Visible light*. PhD thesis, University of Trento, 2017.

[26] Veronica Regazzoni. *Development of a Gamma-Ray Detector based on Silicon Photomultipliers for Prompt Gamma Imaging and High-Energy Spectroscopy*. PhD thesis, University of Trento, 2017.

[27] WTRW Shockley and WT Read Jr. Statistics of the recombinations of holes and electrons. *Physical review*, 87(5):835, 1952.

[28] Re N Hall. Electron-hole recombination in germanium. *Physical review*, 87(2):387, 1952.

[29] Willem Johannes Kindt. Geiger mode avalanche photodiode arrays: For spatially resolved single photon counting. 1999.

[30] Clarence Zener. A theory of the electrical breakdown of solid dielectrics. *Proceedings of the Royal Society of London. Series A, Containing Papers of a Mathematical and Physical Character*, 145(855):523–529, 1934.

[31] Alberto Gola, Fabio Acerbi, Massimo Capasso, Marco Marcante, Alberto Mazzi, Giovanni Paternoster, Claudio Piemonte, Veronica Regazzoni, and Nicola Zorzi. Nuv-sensitive silicon photomultiplier technologies developed at fondazione bruno kessler. *Sensors*, 19(2):308, 2019.

[32] Claudio Piemonte and Alberto Gola. Overview on the main parameters and technology of modern silicon photomultipliers. *Nuclear Instruments and Methods in Physics Research Section A: Accelerators, Spectrometers, Detectors and Associated Equipment*, 2018.

[33] B Dolgoshein, V Balagura, P Buzhan, M Danilov, L Filatov, E Garutti, M Groll, A Ilyin, V Kantserov, V Kaplin, et al. Status report on silicon photomultiplier development and its applications. *Nuclear Instruments and Methods in Physics Research Section A: Accelerators, Spectrometers, Detectors and Associated Equipment*, 563(2):368–376, 2006.

[34] Brian F Aull, Daniel R Schuette, Douglas J Young, David M Craig, Bradley J Felton, and Keith Warner. A study of crosstalk in a 256×256 photon counting imager based on silicon geiger-mode avalanche photodiodes. *IEEE Sensors Journal*, 15(4):2123–2132, 2015.

[35] Andrea L Lacaita, Franco Zappa, Stefano Bigliardi, and Manfredo Manfredi. On the bremsstrahlung origin of hot-carrier-induced photons in silicon devices. *IEEE Transactions on electron devices*, 40(3):577–582, 1993.

[36] WJ Kindt, HW Van Zeijl, and S Middelhoek. Optical cross talk in geiger mode avalanche photodiode arrays: modeling, prevention and measurement. In *Solid-State Device Research Conference, 1998. Proceeding of the 28th European*, pages 192–195. IEEE, 1998.

[37] Sergio Cova, Massimo Ghioni, Franco Zappa, Ivan Rech, and Angelo Gulinatti. A view on progress of silicon single-photon avalanche diodes and quenching circuits. In *Advanced Photon Counting Techniques*, volume 6372, page 63720I. International Society for Optics and Photonics, 2006.

[38] Arthur George Milnes. Deep impurities in semiconductors. 1973.

[39] Sergio Cova, A Lacaita, and Giancarlo Ripamonti. Trapping phenomena in avalanche photodiodes on nanosecond scale. *IEEE Electron device letters*, 12(12):685–687, 1991.

[40] Massimo Ghioni, Angelo Gulinatti, Ivan Rech, Franco Zappa, and Sergio Cova. Progress in silicon single-photon avalanche diodes. *IEEE Journal of selected topics in quantum electronics*, 13(4):852–862, 2007.

[41] Gaetano Zappalà, Fabio Acerbi, Alessandro Ferri, A Gola, Giovanni Paternoster, Nicola Zorzi, and Claudio Piemonte. Set-up and methods for sipm photo-detection efficiency measurements. *Journal of Instrumentation*, 11(08):P08014, 2016.

[42] William G Oldham, Reid R Samuelson, and Paolo Antognetti. Triggering phenomena in avalanche diodes. *IEEE Transactions on electron devices*, 19(9):1056–1060, 1972.

[43] Fabio Acerbi and Stefan Gundacker. Understanding and simulating sipms. *Nuclear Instruments and Methods in Physics Research Section A: Accelerators, Spectrometers, Detectors and Associated Equipment*, 2018.

[44] G Intermite, RE Warburton, A McCarthy, X Ren, F Villa, AJ Waddie, MR Taghizadeh, Y Zou, Franco Zappa, Alberto Tosi, et al. Enhancing the fill-factor of cmos spad arrays using microlens integration. In *Photon Counting Applications 2015*, volume 9504, page 95040J. International Society for Optics and Photonics, 2015.

[45] Danilo Bronzi, F Villa, Simone Bellisai, Simone Tisa, Giancarlo Ripamonti, and Alberto Tosi. Figures of merit for cmos spads and arrays. In *Photon Counting Applications IV; and Quantum Optics and Quantum Information Transfer and Processing*, volume 8773, page 877304. International Society for Optics and Photonics, 2013.

[46] Cristiano L Niclass, Alexis Rochas, Pierre-André Besse, and Edoardo Charbon. A cmos single photon avalanche diode array for 3d imaging. In *2004 IEEE International Solid-State Circuits Conference (IEEE Cat. No. 04CH37519)*, pages 120–517. IEEE, 2004.

[47] Sergio Cova, A Lacaita, M Ghioni, Giancarlo Ripamonti, and TA Louis. 20-ps timing resolution with single-photon avalanche diodes. *Review of scientific instruments*, 60(6):1104–1110, 1989.

[48] Wolfgang Becker. *Advanced time-correlated single photon counting applications*, volume 111. Springer, 2015.

[49] Angelo Gulinatti, P Maccagnani, Ivan Rech, M Ghioni, and Sergio Cova. 35 ps time resolution at room temperature with large area single photon avalanche diodes. *Electronics Letters*, 41(5):272–274, 2005.

[50] A Lacaita, Sergio Cova, A Spinelli, and Franco Zappa. Photon-assisted avalanche spreading in reach-through photodiodes. *Applied physics letters*, 62(6):606–608, 1993.

[51] Fabio Acerbi, Alessandro Ferri, Alberto Gola, Massimo Cazzanelli, Lorenzo Pavesi, Nicola Zorzi, and Claudio Piemonte. Characterization of single-photon time resolution: from single spad to silicon photomultiplier. *IEEE Transactions on Nuclear Science*, 61(5):2678–2686, 2014.

[52] Helmuth Spieler. Fast timing methods for semiconductor detectors. *IEEE Transactions on Nuclear Science*, 29(3):1142–1158, 1982.

[53] D Renker and E Lorenz. Advances in solid state photon detectors. *Journal of Instrumentation*, 4(04):P04004, 2009.

[54] Matthew D Eisaman, Jingyun Fan, Alan Migdall, and Sergey V Polyakov. Invited review article: Single-photon sources and detectors. *Review of scientific instruments*, 82(7):071101, 2011.

[55] VK Zworykin, GA Morton, and L Malter. The secondary emission multiplier-a new electronic device. *Proceedings of the Institute of Radio Engineers*, 24(3):351–375, 1936.

[56] Joseph Ladislas Wiza et al. Microchannel plate detectors. *Nucl. Instrum. Methods*, 162(1-3):587–601, 1979.

[57] EJ Gansen, Mary A Rowe, MB Greene, Danna Rosenberg, Todd E Harvey, MY Su, RH Hadfield, Sae Woo Nam, and Richard P Mirin. Photon-number-discriminating detection using a quantum-dot, optically gated, field-effect transistor. *Nature Photonics*, 1(10):585, 2007.

[58] Kristine M Rosfjord, Joel KW Yang, Eric A Dauler, Andrew J Kerman, Vikas Anant, Boris M Voronov, Gregory N Gol'Tsman, and Karl K Berggren. Nanowire single-photon detector with an integrated optical cavity and anti-reflection coating. *Optics express*, 14(2):527–534, 2006.

[59] Darek P Palubiak and M Jamal Deen. Cmos spads: Design issues and research challenges for detectors, circuits, and arrays. *IEEE Journal of Selected Topics in Quantum Electronics*, 20(6):409–426, 2014.

[60] M Caccia, L Nardo, R Santoro, and D Schaffhauser. Silicon photomultipliers and spad imagers in biophotonics: Advances and perspectives. *Nuclear Instruments and Methods in Physics Research Section A: Accelerators, Spectrometers, Detectors and Associated Equipment*, 2018.

[61] Lucio Pancheri and David Stoppa. A spad-based pixel linear array for high-speed time-gated fluorescence lifetime imaging. In *2009 Proceedings of ESSCIRC*, pages 428–431. IEEE, 2009.

[62] Yuki Maruyama, Jordana Blacksberg, and Edoardo Charbon. A 1024×8, 700-ps time-gated spad line sensor for planetary surface exploration with laser raman spectroscopy and libs. *IEEE Journal of Solid-State Circuits*, 49(1):179–189, 2014.

[63] A Kufcsák, A Erdogan, R Walker, K Ehrlich, M Tanner, A Megia-Fernandez, E Scholefield, P Emanuel, K Dhaliwal, M Bradley, et al. Time-resolved spectroscopy at 19,000 lines per second using a cmos spad line array enables advanced biophotonics applications. *Optics express*, 25(10):11103–11123, 2017.

[64] Samuel Burri, Harald Homulle, Claudio Bruschini, and Edoardo Charbon. Linospad: a time-resolved 256× 1 cmos spad line sensor system featuring 64 fpga-based tdc channels running at up to 8.5 giga-events per second. In *Optical Sensing and Detection IV*, volume 9899, page 98990D. International Society for Optics and Photonics, 2016.

[65] J. M. Pavia, M. Scandini, S. Lindner, M. Wolf, and E. Charbon. A 1 x 400 backside-illuminated SPAD sensor with 49.7 ps resolution, 30 pj/sample TDCs fabricated in 3D CMOS technology for near-infrared optical tomography. *IEEE Journal of Solid-State Circuits*, 50(10):2406–2418, Oct 2015.

[66] Ilkka Nissinen, Jan Nissinen, Pekka Keränen, David Stoppa, and Juha Kostamovaara. A 16×256 spad line detector with a 50-ps, 3-bit, 256-channel time-to-digital converter for raman spectroscopy. *IEEE Sensors Journal*, 18(9):3789–3798, 2018.

[67] Tarek Al Abbas, Neale AW Dutton, Oscar Almer, Neil Finlayson, Francescopaolo Mattioli Della Rocca, and Robert Henderson. A cmos spad sensor with a multi-event folded flash time-to-digital converter for ultra-fast optical transient capture. *IEEE Sensors Journal*, 18(8):3163–3173, 2018.

[68] Luca Parmesan, NA Dutton, Neil J Calder, Nikola Krstajic, Andrew J Holmes, Lindsay A Grant, and Robert K Henderson. A 256× 256 spad array with in-pixel time to amplitude conversion for fluorescence lifetime imaging microscopy. In *International Image Sensor Workshop, Vaals, Netherlands, Memory*, volume 900, page M5, 2015.

[69] Sahba Jahromi, Jussi-Pekka Jansson, and Juha Kostamovaara. Solid-state 3d imaging using a 1nj/100ps laser diode transmitter and a single photon receiver matrix. *Optics express*, 24(19):21619–21632, 2016.

[70] Matteo Perenzoni, Lucio Pancheri, and David Stoppa. Compact spad-based pixel architectures for time-resolved image sensors. *Sensors*, 16(5):745, 2016.

[71] Ilkka Nissinen, Jan Nissinen, Jouni Holma, and Juha Kostamovaara. A 4× 128 spad array with a 78-ps 512-channel tdc for time-gated pulsed raman spectroscopy. *Analog Integrated Circuits and Signal Processing*, 84(3):353–362, 2015.

[72] Nikola Krstajić, James Levitt, Simon Poland, Simon Ameer-Beg, and Robert Henderson. 256× 2 spad line sensor for time resolved fluorescence spectroscopy. *Optics express*, 23(5):5653–5669, 2015.

[73] Paul L Stiles, Jon A Dieringer, Nilam C Shah, and Richard P Van Duyne. Surface-enhanced raman spectroscopy. *Annu. Rev. Anal. Chem.*, 1:601–626, 2008.

[74] https://proteus.ac.uk/.

[75] K Ehrlich, A Kufcsák, N Krstajić, RK Henderson, RR Thomson, and MG Tanner. Fibre optic time-resolved spectroscopy using cmos-spad arrays. In *Optical Fibers and Sensors for Medical Diagnostics and Treatment Applications XVII*, volume 10058, page 100580H. International Society for Optics and Photonics, 2017.

[76] K Ehrlich, A Kufcsák, S McAughtrie, H Fleming, N Krstajic, CJ Campbell, RK Henderson, K Dhaliwal, RR Thomson, and MG Tanner. ph sensing through a single optical fibre using sers and cmos spad line arrays. *Optics express*, 25(25):30976–30986, 2017.

[77] Erik B van Munster and Theodorus WJ Gadella. Fluorescence lifetime imaging microscopy (flim). In *Microscopy techniques*, pages 143–175. Springer, 2005.

[78] Jan Willem Borst and Antonie JWG Visser. Fluorescence lifetime imaging microscopy in life sciences. *Measurement Science and Technology*, 21(10):102002, 2010.

[79] Ahmet T Erdogan, Richard Walker, Neil Finlayson, Nikola Krstajić, Gareth OS Williams, John M Girkin, and Robert K Henderson. A cmos spad line sensor with per-pixel histogramming tdc for time-resolved multispectral imaging. *IEEE Journal of Solid-State Circuits*, 2019.

[80] Leo Huf Campos Braga, Leonardo Gasparini, L Grant, RK Henderson, Nicola Massari, Matteo Perenzoni, David Stoppa, and R Walker. A fully digital $8\times$ 16 sipm array for pet applications with per-pixel tdcs and real-time energy output. 2014.

[81] Alessandro Ferri, Alberto Gola, Nicola Serra, Alessandro Tarolli, Nicola Zorzi, and Claudio Piemonte. Performance of fbk high-density sipm technology coupled to ce: Lyso and ce: Gagg for tof-pet. *Physics in Medicine & Biology*, 59(4):869, 2014.

[82] DW Townsend. Multimodality imaging of structure and function. *Physics in Medicine & Biology*, 53(4):R1, 2008.

[83] Suleman Surti, Austin Kuhn, Matthew E Werner, Amy E Perkins, Jeffrey Kolthammer, and Joel S Karp. Performance of philips gemini tf pet/ct scanner with special consideration for its time-of-flight imaging capabilities. *Journal of Nuclear Medicine*, 48(3):471–480, 2007.

[84] Miles N Wernick and John N Aarsvold. *Emission tomography: the fundamentals of PET and SPECT*. Elsevier, 2004.

[85] William W Moses. Recent advances and future advances in time-of-flight pet. In *AIP Conference Proceedings*, volume 1204, pages 119–125. AIP, 2010.

[86] Leonardo Gasparini, Bänz Bessire, Manuel Unternährer, André Stefanov, Dmitri Boiko, Matteo Perenzoni, and David Stoppa. Supertwin: towards 100kpixel cmos quantum image sensors for quantum optics applications. In *Quantum Sensing and Nano Electronics and Photonics XIV*, volume 10111, page 101112L. International Society for Optics and Photonics, 2017.

[87] Samuel Burri, D Stucky, Yuki Maruyama, Claudio Bruschini, Edoardo Charbon, and Francesco Regazzoni. Jailbreak imagers: transforming a single-photon image sensor into a true random number generator. Technical report, 2013.

[88] Nicola Massari, Leonardo Gasparini, Alessandro Tomasi, Alessio Meneghetti, Hesong Xu, Daniele Perenzoni, Guglielmo Morgari, and David Stoppa. 16.3 a 16× 16 pixels spad-based 128-mb/s quantum random number generator with- 74db light rejection ratio and- 6.7 ppm/Â° c bias sensitivity on temperature. In *2016 IEEE International Solid-State Circuits Conference (ISSCC)*, pages 292–293. IEEE, 2016.

[89] T. A. Abbas, N. A. W. Dutton, O. Almer, S. Pellegrini, Y. Henrion, and R. K. Henderson. Backside illuminated SPAD image sensor with 7.83 um pitch in 3D-stacked CMOS technology. In *2016 IEEE International Electron Devices Meeting (IEDM)*, pages 8.1.1–8.1.4, Dec 2016.

[90] Helmuth Spieler. *Semiconductor detector systems*, volume 12. Oxford university press, 2005.

[91] Glenn F Knoll. *Radiation detection and measurement*. John Wiley & Sons, 2010.

[92] Lev Davidovich Landau. On the energy loss of fast particles by ionization. *J. Phys.*, 8:201–205, 1944.

[93] Frank Hartmann. Silicon tracking detectors in high-energy physics. *Nuclear Instruments and Methods in Physics Research Section A: Accelerators, Spectrometers, Detectors and Associated Equipment*, 666:25–46, 2012.

[94] Martin A Green and Mark J Keevers. Optical properties of intrinsic silicon at 300 k. *Progress in Photovoltaics: Research and Applications*, 3(3):189–192, 1995.

[95] Leonardo Rossi, Peter Fischer, Tilman Rohe, and Norbert Wermes. *Pixel detectors: From fundamentals to applications*. Springer Science & Business Media, 2006.

[96] David Price and Kurt Skold. *Neutron scattering*. Academic Press, 1987.

[97] Michael Moll. Displacement damage in silicon detectors for high energy physics. *IEEE Transactions on Nuclear Science*, 65(8):1561–1582, 2018.

[98] https://rd50.web.cern.ch/rd50/.

[99] Gerhard Lutz et al. *Semiconductor radiation detectors*, volume 40. Springer, 1999.

[100] R Wunstorf. *Systematic Investigation of the Radiation Hardness of Silicon Detectors for Application in High Energy Physics Experiments*. PhD thesis, PhD thesis, Hamburg University, 1992.

[101] Gijs Dingemans and WMM Kessels. Status and prospects of al2o3-based surface passivation schemes for silicon solar cells. *Journal of Vacuum Science & Technology A: Vacuum, Surfaces, and Films*, 30(4):040802, 2012.

[102] B Mikulec, M Campbell, G Dipasquale, Ch Schwarz, and J Watt. Characterisation of a single photon counting pixel system for imaging of low-contrast objects. *Nuclear Instruments and Methods in Physics Research Section A: Accelerators, Spectrometers, Detectors and Associated Equipment*, 458(1-2):352–359, 2001.

[103] SV Tipnis, VV Nagarkar, I Shestakova, V Gaysinskiy, G Entine, MP Tornai, and BC Stack. Feasibility of a beta-gamma digital imaging probe for radioguided surgery. *IEEE Transactions on Nuclear Science*, 51(1):110–116, 2004.

[104] Josef Kemmer. Fabrication of low noise silicon radiation detectors by the planar process. *Nuclear Instruments and Methods*, 169(3):499–502, 1980.

[105] Gianluca Rizzo, C Avanzini, Giovanni Batignani, Stefano Bettarini, F Bosi, Giovanni Calderini, M Ceccanti, R Cenci, A Cervelli, F Crescioli, et al. Development of deep n-well maps in a 130 nm cmos technology and beam test results on a 4k-pixel matrix with digital sparsified readout. In *2008 IEEE Nuclear Science Symposium Conference Record*, pages 3242–3247. IEEE, 2008.

[106] A Gabrielli, SLIM5 Collaboration, et al. Development of a triple well cmos maps device with in-pixel signal processing and sparsified readout capabilities. *Nuclear Instruments and Methods in Physics Research Section A: Accelerators, Spectrometers, Detectors and Associated Equipment*, 581(1-2):303–305, 2007.

[107] N D'Ascenzo, PS Marrocchesi, CS Moon, F Morsani, L Ratti, V Saveliev, A Savoy Navarro, and Q Xie. Silicon avalanche pixel sensor for high precision tracking. *Journal of Instrumentation*, 9(03):C03027, 2014.

[108] Valeri Saveliev. Avalanche pixel sensors and related methods, September 18 2012. US Patent 8,269,181.

[109] MM Vignetti, F Calmon, P Pittet, G Pares, R Cellier, L Quiquerez, T Chaves de Albuquerque, E Bechetoille, E Testa, J-P Lopez, et al. 3d silicon coincidence avalanche detector (3d-sicad) for charged particle detection. *Nuclear Instruments and Methods in Physics Research Section A: Accelerators, Spectrometers, Detectors and Associated Equipment*, 881:53–59, 2018.

[110] http://www.tifpa.infn.it/projects/apix2/.

[111] https://indico.cern.ch/event/716539/contributions/3246038/.

[112] Marco Musacci. *Design and characterization of CMOS SPADs for charged particle detectors*. PhD thesis, University of Pavia, 2018.

[113] Andrea Ficorella, Lucio Pancheri, Paolo Brogi, Gianmaria Collazuol, Gian-Franco Dalla Betta, Pier Simone Marrocchesi, Fabio Morsani, Lodovico Ratti, and Aurore Savoy-Navarro. Crosstalk characterization of a two-tier pixelated avalanche sensor for charged particle detection. *IEEE Journal of Selected Topics in Quantum Electronics*, 24(2):1–8, 2018.

[114] Lucio Pancheri and David Stoppa. Low-noise single photon avalanche diodes in 0.15 μm CMOS technology. In *Solid-State Device Research Conference (ESSDERC), 2011 Proceedings of the European*, pages 179–182. IEEE, 2011.

[115] Lucio Pancheri, Andrea Ficorella, Paolo Brogi, G Collazuol, Gian-Franco Dalla Betta, PS Marrocchesi, Fabio Morsani, Lodovico Ratti, Aurore Savoy-Navarro, and Arta Sulaj. First demonstration of a two-tier pixelated avalanche sensor for charged particle detection. *IEEE Journal of the Electron Devices Society*, 5(5):404–410, 2017.

[116] Gian-Franco Dalla Betta, Lucio Pancheri, David Stoppa, Robert Henderson, and Justin Richardson. Avalanche photodiodes in submicron cmos technologies for high-sensitivity imaging. In *Advances in photodiodes*. InTech, 2011.

[117] Hesong Xu, Lucio Pancheri, Leo HC Braga, Gian-Franco Dalla Betta, and David Stoppa. Crosstalk characterization of single-photon avalanche diode (SPAD) arrays in CMOS 150nm technology. *Procedia Engineering*, 87:1270–1273, 2014.

[118] Ivan Rech, Antonino Ingargiola, Roberto Spinelli, Ivan Labanca, Stefano Marangoni, Massimo Ghioni, and Sergio Cova. Optical crosstalk in single photon avalanche diode arrays: a new complete model. *Optics express*, 16(12):8381–8394, 2008.

[119] A Ficorella, L Pancheri, G-F Dalla Betta, P Brogi, G Collazuol, PS Marrocchesi, F Morsani, L Ratti, and A Savoy-Navarro. Crosstalk mapping in CMOS SPAD arrays. In *Solid-State Device Research Conference (ESSDERC), 2016 46th European*, pages 101–104. IEEE, 2016.

[120] Calvin Chao, Chin-Hao Chang, Manoj Mhala, Po-Sheng Chou, Hon-Yih Tu, Shang-Fu Yeh, Kuo-Yu Chou, Charles Liu, and Fu-Lung Hsueh. Detection and shielding of photon emission in stacked CIS. In *2015 International Image Sensor Workshop (IISW 2015)*, pages 51–54, June 2015.

[121] Lucio Pancheri, David Stoppa, and Gian-Franco Dalla Betta. Characterization and modeling of breakdown probability in sub-micrometer CMOS SPADs. *IEEE Journal of Selected Topics in Quantum Electronics*, 20(6):328–335, 2014.

[122] Marek Gersbach, Cristiano Niclass, Lucio Carrara, Maximilian Sergio, Noémy Scheidegger, Herbert Shea, Edoardo Charbon, and Silicon Biosystems. A study of the effects of gamma radiation on cmos single-photon avalanche diodes. In *Proc. 7th IEEE Conf. Sensors*, pages 919–922, 2008.

[123] Lucio Carrara, Cristiano Niclass, Noémy Scheidegger, Herbert Shea, and Edoardo Charbon. A gamma, x-ray and high energy proton radiation-tolerant cis for space applications. In *2009 IEEE International Solid-State Circuits Conference-Digest of Technical Papers*, pages 40–41. IEEE, 2009.

[124] Matteo Perenzoni, Daniele Perenzoni, David Stoppa, Alexandre Pollini, Jacques Haesler, and Christophe Pache. 3d imaging with cmos single-photon detector arrays for space applications: Ground-based measurements and irradiation tests. In *Proc. Int. Image Sensor Workshop*, pages 262–265, 2017.

[125] F Di Capua, M Campajola, L Campajola, C Nappi, E Sarnelli, L Gasparini, and H Xu. Random telegraph signal in proton irradiated single-photon avalanche diodes. *IEEE Transactions on Nuclear Science*, 65(8):1654–1660, 2018.

[126] Lodovico Ratti, P Brogi, G Collazuol, G-F Dalla Betta, A Ficorella, L Lodola, PS Marrocchesi, S Mattiazzo, F Morsani, M Musacci, et al. Dark count rate degradation in cmos spads exposed to x-rays and neutrons. *IEEE Transactions on Nuclear Science*, 66(2):567–574, 2019.

[127] Pier Simone Marrocchesi, Maria Grazia Bagliesi, Simone Bonechi, Gabriele Bigongiari, Paolo Brogi, Gianmaria Collazuol, Alessandro Ferri, Paolo Maestro, Claudio Piemonte, Arta Sulaj, et al. Charged particle detection with nuv-sensitive sipm in a beam of relativistic ions. *IEEE Transactions on Nuclear Science*, 61(5):2786–2793, 2014.

[128] S Agosteo, P Colautti, J Esposito, A Fazzi, MV Introini, and A Pola. Characterization of the energy distribution of neutrons generated by 5 mev protons on a thick beryllium target at different emission angles. *Applied Radiation and Isotopes*, 69(12):1664–1667, 2011.

[129] JR Srour, Z Shanfield, RA Hartmann, S Othmer, and DM Newberry. Permanent damage introduced by single particles incident on silicon devices. *IEEE Transactions on Nuclear Science*, 30(6):4526–4532, 1983.

[130] George C Messenger. A summary review of displacement damage from high energy radiation in silicon semiconductors and semiconductor devices. *IEEE Transactions on nuclear Science*, 39(3):468–473, 1992.

[131] Massimo Manghisoni, Lodovico Ratti, Valerio Re, and Valeria Speziali. Radiation hardness perspectives for the design of analog detector readout circuits in the 0.18-$/mum$ cmos generation. *IEEE Transactions on Nuclear Science*, 49(6):2902–2909, 2002.

[132] Kimberly E Kolb, Donald F Figer, Joong Y Lee, and Brandon J Hanold. Radiation tolerance of a geiger-mode avalanche photodiode imaging array. *Journal of Astronomical Telescopes, Instruments, and Systems*, 2(3):036001, 2016.

[133] O Alonso, R Casanova, A Dieguez, J Dingfelder, T Hemperek, T Kishishita, T Kleinohl, M Koch, H Krüger, M Lemarenko, et al. Depfet active pixel detectors for a future linear e^+e^- collider. *IEEE Transactions on Nuclear Science*, 60(2):1457–1465, 2013.

[134] Ennio Bertolucci, M Maiorino, G Mettivier, MC Montesi, and P Russo. Preliminary test of an imaging probe for nuclear medicine using hybrid pixel detectors. *Nuclear Instruments and Methods in Physics Research Section A: Accelerators, Spectrometers, Detectors and Associated Equipment*, 487(1-2):193–201, 2002.

[135] Ari Kilpelä, Riku Pennala, and Juha Kostamovaara. Precise pulsed Time-of-Flight laser range finder for industrial distance measurements. *Review of Scientific Instruments*, 72(4):2197–2202, 2001.

[136] Cristiano Niclass, Mineki Soga, Hiroyuki Matsubara, Satoru Kato, and Manabu Kagami. A 100m-Range 10-Frame/s 340×96-Pixel Time-of-Flight Depth Sensor in 0.18μm CMOS. *IEEE Journal of Solid-State Circuits*, 48:559–572, 02 2013.

[137] A Ullrich and M Pfennigbauer. Linear LIDAR versus Geiger-mode LIDAR: impact on data properties and data quality. In *Laser Radar Technology and Applications XXI*, volume 9832, page 983204. International Society for Optics and Photonics, 2016.

[138] JJ Eckl and KU Schreiber. High accurate range finding with SPADs at 1064nm. In *Photon Counting Applications IV; and Quantum Optics and Quantum Information Transfer and Processing*, volume 8773, page 87730A. International Society for Optics and Photonics, 2013.

[139] Ravil Agishev, Adolfo Comerón, Jordi Bach, Alejandro Rodriguez, Michaël Sicard, Jordi Riu, and Santiago Royo. Lidar with SiPM: Some capabilities and limitations in real environment. *Optics & Laser Technology*, 49:86–90, 2013.

[140] Sergey L Vinogradov. Evaluation of performance of silicon photomultipliers in lidar applications. In *Photon Counting Applications 2017*, volume 10229, page 102290L. International Society for Optics and Photonics, 2017.

[141] Gabriele Adamo and Alessandro Busacca. Time Of Flight measurements via two LiDAR systems with SiPM and APD. In *AEIT International Annual Conference (AEIT), 2016*, pages 1–5. IEEE, 2016.

[142] Salvatore Gnecchi and Carl Jackson. A 1×16 SiPM Array for Automotive 3D Imaging LiDAR Systems. *International Image Sensor Workshop (IISW), 2017*, 2017.

[143] Matteo Perenzoni, Daniele Perenzoni, and David Stoppa. A 64×64-Pixels Digital Silicon Photomultiplier Direct ToF Sensor with 100-MPhotons/s/pixel Background Rejection and Imaging/Altimeter Mode with 0.14% Precision up to 6 km for Spacecraft Navigation and Landing. *IEEE Journal of Solid-State Circuits*, 52(1):151–160, 2017.

[144] Cristiano Niclass, Kota Ito, Mineki Soga, Hiroyuki Matsubara, Isao Aoyagi, Satoru Kato, and Manabu Kagami. Design and characterization of a 256×64-pixel single-photon imager in CMOS for a MEMS-based laser scanning time-of-flight sensor. *Optics Express*, 20(11):11863–11881, 2012.

[145] S Pellegrini and B Rae. Fully industrialised single photon avalanche diodes. In *Advanced Photon Counting Techniques XI*, volume 10212, page 102120D. International Society for Optics and Photonics, 2017.

[146] Alessandro Tontini, Leonardo Gasparini, Lucio Pancheri, and Roberto Passerone. Design and Characterization of a Low-Cost FPGA-Based TDC. *IEEE Transactions on Nuclear Science*, 65(2):680–690, 2018.

[147] F Acerbi, A Ferri, G Zappala, G Paternoster, A Gola, N Zorzi, and C Piemonte. Technological and Design Improvements of FBK NUV Silicon-Photomultipliers. *Fotonica AEIT Italian Conference on Photonics Technologies, 2015*, 2015.

[148] Claudio Piemonte, Fabio Acerbi, Alessandro Ferri, Alberto Gola, Giovanni Paternoster, Veronica Regazzoni, Gaetano Zappala, and Nicola Zorzi. Performance of NUV-HD Silicon Photomultiplier Technology. *IEEE Transactions on Electron Devices*, 63(3):1111–1116, 2016.

[149] Alberto Gola, Alessandro Tarolli, and Claudio Piemonte. SiPM Cross-talk Amplification due to Scintillator Crystal: Effects on Timing Performance. In *Nuclear Science Symposium and Medical Imaging Conference (NSS/MIC), 2012 IEEE*, pages 421–423. IEEE, 2012.

[150] Fabio Acerbi, Alessandro Ferri, Gaetano Zappala, Giovanni Paternoster, Antonino Picciotto, Alberto Gola, Nicola Zorzi, and Claudio Piemonte. NUV Silicon Photomultipliers with High Detection Efficiency and Reduced Delayed Correlated-Noise. *IEEE transactions on Nuclear Science*, 62(3):1318–1325, 2015.

[151] Wolfgang Becker. *The bh TCSPC handbook*. Becker & Hickl, 2014.

[152] A Ficorella, L Pancheri, F Acerbi, and C Piemonte. Effect of cell size on ambient light rejection in SiPM-based Time-of-Flight range sensors. In *SENSORS, 2017 IEEE*, pages 1–3. IEEE, 2017.

[153] Jaakko MT Huikari, Eugene A Avrutin, Boris S Ryvkin, Jan J Nissinen, and Juha Tapio Kostamovaara. High-energy picosecond pulse generation by gain switching in asymmetric waveguide structure multiple quantum well lasers. *IEEE journal of Selected Topics in Quantum Electronics*, 21(6):189–194, 2015.